EVALUATION OF THE WRF & WRF-HYDRO MODELING SYSTEM TO BETTER UNDERSTAND THE HYDROMETEOROLOGICAL INTERACTIONS OVER HUMID AND SEMI-ARID CLIMATE CONDITIONS

A THESIS SUBMITTED TO
THE GRADUATE SCHOOL OF NATURAL AND APPLIED SCIENCES
OF
MIDDLE EAST TECHNICAL UNIVERSITY

BY

EREN DÜZENLİ

IN PARTIAL FULFILLMENT OF THE REQUIREMENTS
FOR
THE DEGREE OF DOCTOR OF PHILOSOPHY
IN
CIVIL ENGINEERING

OCTOBER 2022

Approval of the thesis:

EVALUATION OF THE WRF & WRF-HYDRO MODELING SYSTEM TO BETTER UNDERSTAND THE HYDROMETEOROLOGICAL INTERACTIONS OVER HUMID AND SEMI-ARID CLIMATE CONDITIONS

submitted by **EREN DÜZENLİ** in partial fulfillment of the requirements for the degree of **Doctor of Philosophy** i**n Civil Engineering, Middle East Technical University** by,

Prof. Dr. Halil Kalıpçılar
Dean, Graduate School of **Natural and Applied Sciences** _____

Prof. Dr. Erdem Canbay
Head of the Department, **Civil Engineering** _____

Assoc. Prof. Dr. Mustafa Tuğrul Yılmaz
Supervisor, **Civil Engineering** _____

Prof. Dr. İsmail Yücel
Co-Supervisor, **Civil Engineering** _____

Examining Committee Members:

Prof. Dr. Melih Yanmaz
Civil Engineering, METU _____

Assoc. Prof. Dr. Mustafa Tuğrul Yılmaz
Civil Engineering, METU _____

Prof. Dr. Elçin Kentel
Civil Engineering, METU _____

Prof. Dr. Ömer Lütfi Şen
Climate and Marine Sciences, Istanbul Technical University _____

Assoc. Prof. Dr. Abdulla Sakallı
Industrial Engineering, Iskenderun Technical University _____

Date: 07.10.2022

I hereby declare that all information in this document has been obtained and presented in accordance with academic rules and ethical conduct. I also declare that, as required by these rules and conduct, I have fully cited and referenced all material and results that are not original to this work.

Name Last name : Eren Düzenli

Signature :

ABSTRACT

EVALUATION OF THE WRF & WRF-HYDRO MODELING SYSTEM TO BETTER UNDERSTAND THE HYDROMETEOROLOGICAL INTERACTIONS OVER HUMID AND SEMI-ARID CLIMATE CONDITIONS

Düzenli, Eren
Doctor of Philosophy, Civil Engineering
Supervisor : Assoc. Prof. Dr. Mustafa Tuğrul Yılmaz
Co-Supervisor: Prof. Dr. İsmail Yücel

October 2022, 112 pages

Changing climate causes extreme weather events, such as heavy precipitation and flash floods, to occur more destructive and frequently. Thus, it is worthwhile to perform a reliable prediction of hydrometeorological circumstances reasonably before extreme events occur. Similarly, robust estimation of future weather conditions would contribute significantly to long-term water management issues, one of the most crucial problems of our time. Accordingly, this study evaluates the skill of (un)coupled WRF/WRF-Hydro system to estimate hydrometeorological variables for both short-term and long-term periods under humid and semi-arid climate conditions. Firstly, a sensitivity analysis of the model physics and initial and lateral boundary data source on the precipitation outputs of the standalone WRF model is conducted for some short-term extreme precipitation events over the Eastern Black Sea (EBS; a humid region) and Mediterranean (MED; a semi-arid region) regions. The sensitivity analysis is repeated for different seasons (i.e., autumn and summer) and spatial resolutions of the model domains (i.e., 9 km and 3 km). The aim here is to construct a reliable early warning system for two flood-prone

regions of Turkey. Secondly, the WRF model is coupled with a hydrologic model, WRF-Hydro. The coupled model is initiated with Soil Moisture Active Passive level 4 (SMAP) data. These analyses aim to improve the simulation of the energy fluxes between the land and the atmosphere. According to the results of the first part, the model physics are generally more influential than the initial and lateral boundary data source on extreme precipitation variability. For the second part, the fully coupled models correct the location and magnitude of the occurrence of hourly extreme precipitation. Changing the initial soil moisture data source affects the terrestrial water cycle elements in the semi-arid region more than in the humid area, especially in spring and summer, which are drier periods.

Keywords: WRF & WRF-Hydro Coupling, Extreme Event Simulation, Terrestrial Water Cycle, Land Surface Energy Fluxes, Sensitivity Analysis

ÖZ

HİDROMETEOROLOJİK ETKİLEŞİMLERİN DAHA İYİ ANLAŞILABİLMESİ AMACIYLA WRF & WRF-HYDRO MODELLEME SİSTEMİNİN NEMLİ VE YARI KURAK İKLİM KOŞULLARINDA DEĞERLENDİRİLMESİ

Düzenli, Eren
Doktora, İnşaat Mühendisliği
Tez Yöneticisi: Doç. Dr. Mustafa Tuğrul Yılmaz
Ortak Tez Yöneticisi: Prof. Dr. İsmail Yücel

Ekim 2022, 112 sayfa

Değişen iklim, yoğun yağış ve ani sel gibi aşırı hava olaylarının daha yıkıcı ve daha sık yaşanmasına sebep olmaktadır. Bu nedenle, hidrometeorolojik değişkenlerin güvenilir tahminlerini aşırı durumlar meydana gelmeden makul bir süre önce gerçekleştirmek ve geliştirmek çok önemlidir. Benzer şekilde, gelecekteki hava koşullarının sağlam bir şekilde tahmin edilmesi, zamanımızın en önemli sorunlarından biri olan uzun vadeli su yönetimi meselesine önemli ölçüde katkıda bulunacaktır. Alakalı olarak, bu çalışma bağımsız ve bütünleşik olarak çalıştırılan WRF/WRF-Hydro sisteminin nemli ve yarı kurak iklim koşullarında hem uzun hem de kısa dönemler için hidrometeorolojik değişkenleri tahmin edebilme beceresini değerlendirmektedir. İlk olarak, bağımsız WRF modelinin yağış çıktılarının, Doğu Karadeniz (EBS; nemli bölge) ve Akdeniz (MED; yarı kurak bölge) bölgeleri üzerinde, bazı kısa vadeli aşırı yağış olayları aracılığıyla model fiziği ve başlangıç veri kaynağına olan duyarlılığı test edilmiştir. Duyarlılık analizi, farklı mevsimler (yani; sonbahar ve yaz) ve farklı mekânsal çözünürlük değerleri (yani; 9 km ve 3 km) için tekrarlanmıştır. Buradaki temel amaç, Türkiye'nin sele yatkın iki bölgesi

üzerinde güvenilir bir erken uyarı sistemi kurmaktır. İkinci olarak, WRF modeli hidrolojik bir model olan WRF-Hydro ile bütünleşik şekilde çalıştırılmıştır. Bütünleşik model ayrıca SMAP verileriyle de başlatılmıştır. Bu analizler, kara ve atmosfer arasındaki enerji akış simülasyonlarını iyileştirmeyi hedeflemektedir. İlk kısmın sonuçlarına göre, model fiziği aşırı yağış değişkenliği üzerinde başlangıç veri kaynağından genellikle daha etkilidir. İkinci kısma gelinirse, bütünleşik model kullanımı saatlik aşırı yağış oluşumunun konum ve büyüklük tahminini iyileştirmeye yardımcı olmuştur. Başlangıç toprak nemi veri kaynağının değiştirilmesi karasal su döngüsü çıktılarını yarı kurak bölgede özellikle kurak dönemler olan ilkbahar ve yaz aylarında nemli bölgeye nazaran daha fazla etkilemiştir.

Anahtar Kelimeler: Bütünleşik WRF & WRF-Hydro Modeli, Aşırı olay simülasyonu, Karasal Su Döngüsü, Kara Yüzey Enerji Akıları, Duyarlılık Analizi

To the grain of sand in the sky

ACKNOWLEDGMENTS

This thesis is a product of a collaborative work supported by many people in their own ways. First of all, I would like to thank my supervisor Assoc. Prof. Dr. Mustafa Tuğrul Yılmaz and co-supervisor Prof. Dr. İsmail Yücel, who never gave up on me and answered all my questions with patience. I am deeply grateful for their generous support.

The committee members: Prof. Dr. Melih Yanmaz, Prof. Dr. Elçin Kentel, Prof. Dr. Ömer Lütfi Şen, Assoc. Prof. Dr. Abdulla Sakallı greatly assisted me through their insightful comments in shaping the final draft of this study. I am very thankful to them for spending their time and efforts.

I have greatly benefited from the feedbacks and comments of my thesis monitoring committee, Prof. Dr. Elçin Kentel, and Assoc. Prof. Dr. Abdulla Sakallı, during my PhD research. I would like to express my gratitude for sharing their knowledge and their constructive comments and suggestions on my study.

I would also like to pay my deepest gratitude to Prof. Dr. İsmail Yücel and Prof. Dr. Melih Yanmaz, who helped me all along my PhD study. I will be appreciating this in my whole life and I will always remember them with love and respect.

I would like to thank the Scientific and Technological Research Council of Turkey for supporting this thesis under the project number TUBITAK 116Y193.

I would like to thank my colleagues: Beril Aydın, Berina Mina Kılıçarslan, Burak Bulut, Eray Ercan, Heves Pilatin, Ömer Burak Akgün, Mehdi Hesami Afshar, Murat Yeğin and Serkan Bayar for all their help and support.

Not only my friends from the academic circle but also my friends with whom I share the burden of our lives were always with me through their endless love, joy and support. For this, I would like to thank: Bulut Başkan, Ecem Seçkin Gökyer, Emre Gökyer, Gamze Karaca, Hüseyin Kağan İmamoğlu, Mert Alperten, Özgür Balkılıç,

Ruken Dilara Zaf, Selçuk Güler, Yunus Arif Kesmez and Zeynep Tufan. I seek to understand, learn, smile, push the limits, take risks, improve, change, remember, forget and restart with them.

I would like to thank my sister Deniz Düzenli for her unique energy and my brother Rıza Can Öztürk for his love and beautiful smile, which he always shares with me. Their presences are precious to me.

I would like to express my deepest gratitude to my lovely mothers Asya Düzenli, Hatice Öztürk and Yıldız Nakkaş for their unconditional and endless love.

In every decision I make, my brothers Alper Nakkaş, Emre Düzenli and Serdar Nakkaş, and my father Fatih Öztürk have always been backing me. I would like to thank them sincerely. I know I will always become stronger when I have them beside me.

Perihan Öztürk Düzenli has always inspired my desire to understand the essence of the universe. She always makes me appreciate how life is short, precious, and worth living. I would like to thank her for choosing to be my companion in a tiny spot in the vastness of time and the infinity of the universe.

I would like to thank the loving memory of Ahmet Nakkaş. I still remember and appreciate the priceless times we spent together.

I would like to thank my father Ali Düzenli with all my respect and longing. I will exceed the speed of light to see you again from millions of light years away.

TABLE OF CONTENTS

LIST OF TABLES

TABLES

LIST OF FIGURES

FIGURES

LIST OF ABBREVIATIONS

ABBREVIATIONS	
AATS	Aerosol–aware Thompson Scheme
AWOS	Automated weather observation systems
BMJ	Betts–Miller–Janjic Scheme
CSI	Critical Success Index
CU	Cumulus
DEM	Digital elevation model
DSI	General Directorate of State Hydraulic Works
EBS	Eastern Black Sea
ECMWF	European Centre for Medium-Range Weather Forecasts
ES	Eta (Ferrier) Scheme
ET	Evapotranspiration
FAR	False alarm ratio
FBI	Frequency bias index
FNL	Final analysis
GFES	Grell–Freitas Ensemble Scheme
GFS	Global Forecast System
HydroSHEDS	Hydrological data and maps based on Shuttle Elevation Derivatives at multiple Scales
IDW	Inverse Distance Weighting
KF	Kain–Fritsch Scheme
KGE	Kling-Gupta efficiency
KS	Kessler Scheme
LCC	Lambert conformal conic
LKSATFAC	Lateral saturated hydraulic conductivity scaling factor
LSM	Land surface model
MAE	Mean absolute error
MARS	Multivariate adaptive regression splines

MBE	Mean bias error
MED	Mediterranean
MGM	General Directorate of Meteorology
MP	Microphysics
MYJ	Mellor–Yamada–Janjic Scheme
NASA	National Aeronautics and Space Administration
NCAR	National Center of Atmospheric Research
NCEP	National Centers for Environmental Prediction
NOAA	National Oceanic and Atmospheric Administration
NSE	Nash-Sutcliffe efficiency
NWP	Numerical weather prediction
OVROUGHRTFAC	Overland roughness scaling factor
PBL	Planetary boundary layer
PC	Percent correct
POD	Probability of detection
REFDK	the reference (silty clay loam) saturated hydraulic conductivity
REFKDT	Infiltration depth
REG	Linear regression
RETDEPRTFAC	Retention depth scaling factor
RMSE	Root means square error
SLOPE	Free drainage coefficient
SMAP	Soil Moisture Active Passive level 4
SST	Sea surface temperature
TOPSIS	The Technique for Order of Preference by Similarity to Ideal Solution
VAR	Variance matching
WPS	WRF preprocessing system
WRF	Weather Research and Forecasting
WRF-Coup	Coupled WRF & WRF-Hydro modeling system

WRF-Hydro	(Weather Research and Forecasting)-Hydro
WRF-Hydro-SA	Standalone WRF-Hydro model
WRF-SA	Standalone WRF model
WRF-SM-Coup	Coupled WRF & WRF-Hydro modeling system initiated with SMAP data
WSM6	WRF Single–moment 6–class Scheme
YSU	Yonsei University Scheme

CHAPTER 1

INTRODUCTION

1.1 Sensitivity of the extreme precipitation simulation capability of the WRF model against model physics and initial and lateral boundary data source

Spatiotemporal variability of precipitation characteristics (e.g., intensity and duration) are significantly influenced by global warming. The expected changes in hydrometeorological variables such as high temperatures, high evapotranspiration rates, and desiccating winds will not only cause drought with higher severity and longer duration but also increase the water vapor holding capacity of the air (Trenberth, 2011; Spinoni et al., 2020; Afshar et al., 2020) hence the increased likelihood of extreme precipitation events (e.g., rainstorms). In other words, the abrupt condensation of excessive water vapor enhances the probability of encountering more intense rain showers, which often triggers flash floods. To properly manage these extreme events, it is crucial to develop early warning systems (i.e., operational modeling systems that are capable of predicting extreme precipitation events a couple of days before it happens) utilizing the state-of-the-art weather prediction and hydrological models, which are capable of estimating the events with high accuracy and longer lead time.

Sub-daily precipitation extremes are more prone to be exacerbated by global warming than daily or longer-term extremes (Ali and Mishra, 2018). Clausius–Clapeyron equation proves that the water vapor holding capacity of the air, the origin of the sub-daily extreme precipitation, increases with 7% per kelvin for the average mid-latitude conditions (Berg et al., 2018), and the intensities of the sub-daily extremes are anticipated to increase more than 7% per degree warming for the regions in mid-latitude (Prein et al., 2017). Further, short term prediction or long-

term projection of the variations in the sub-daily extremes are substantial for the estimation of the resulting flash or fluvial floods. Therefore, the competence to predict extreme precipitation in sub-daily temporal resolution is one of the greatest assets of an early warning system.

Complex topography, land-use heterogeneity, and close proximity to the sea are some of the important geophysical features that control the synoptic-scale and local weather conditions (Pielke et al., 2006; Yucel et al., 2015; Bulut et al., 2019; Amjad et al., 2020). These features highly exist in Turkey, and they also provide significant control over land-sea-atmosphere interactions. Moreover, forecasting spatial and temporal variations of extreme precipitation is a challenging issue, especially for the regions with a complex topography (Yucel and Onen, 2014; Amjad et al., 2020). The Mediterranean (MED) and Black Sea regions show serious weather hazards that resulted from heavy precipitation events. Besides, extreme precipitation behaviors of these regions differ for dry and wet seasons (Duzenli et al., 2018). Thus, the evaluation of model predictability over these regions is essential. By constructing spatiotemporally sensitive simulations through the numerical weather prediction (NWP) models, the possible catastrophic consequences of probable disasters can be prevented.

Even though there are global NWP models producing precipitation data, the spatial and temporal resolution of the data is generally low to study local extreme events because of the computational limitations (Sikder and Hossain, 2016) and the inadequacy in resolving the initial and lateral boundary conditions and the localized atmospheric dynamics in organized convective systems (Weisman et al., 1997, Done et al., 2004; Li et al., 2012; Gustafson Jr. et al., 2014; Li et al., 2019). According to Prein et al. (2015), with appropriate initial and lateral boundary conditions and model physics configurations, convection-permitting simulations (i.e., finer than 4 km) via NWP models offer great potential for the improved precipitation forecast. The added values of these kind of simulations to the global NWP models are widely accepted, especially in the regions with a strong heterogeneous underlying boundary (Fosser et al., 2015; Cassola et al., 2015; Zittis et al., 2017; Van de Walle et al., 2020). The

Weather Research and Forecasting (WRF; Skamarock et al., 2019) model is one of the most advanced convection-permitting (i.e., spatial resolution < 4km) NWP models to predict the alterations in the meteorological events through downscaling of the large scale models' data (Zhou and Mu, 2018).

However, the success of WRF predictability directly depends on selecting the appropriate model physical parameterization, the accurate initial and lateral boundary conditions, and the representative spatial resolution (García-Díez et al., 2013; Di et al., 2015; Dyer et al., 2016; Mylonas et al., 2019). There are a large number of options for each physics of the WRF model, enabling users to enhance the model for specific geographies (Evans et al., 2012). As the number of parameterization schemes increases, it becomes more difficult to determine the best combination of physical parameterization schemes. Therefore, model sensitivity study to determine the best WRF configuration and its testing through independent storm events and specified geographical regions are imperative prior to its operational use. Many other studies (Rao et al., 2007; Liu et al., 2012; Evans et al., 2012; Efstathiou et al., 2013; Mannan et al., 2013; Yucel and Onen, 2014; Pennelly et al., 2014) evaluated the sensitivity of these features.

Overall, NWP accuracy is primarily controlled by the choices of model physics, initial and lateral boundary condition dataset, and horizontal grid spacing (i.e., spatial resolution). Among five model physics of the WRF model, microphysics (MP), cumulus (CU), and planetary boundary layer (PBL) scheme selection received the highest attention in the literature in sensitivity studies. According to Kan et al. (2015), although the MP scheme is the most determinant among them, MP, CU, and PBL schemes are the main factors of precipitation estimation in WRF. Argüeso et al. (2011) have tested eight different scenarios to check the sensitivity of the precipitation and temperature outputs against MP, CU, and PBL schemes in a region with a complex topography and Mediterranean climate. They have found that, unlike Kan et al. (2015), the precipitation estimates are substantially driven by CU and PBL schemes in Andalusia, while MP scheme selection does not have a significant impact on the results. Similarly, Yucel and Onen (2014) also stated the higher sensitivity

from the choice of convective treatment (i.e., CU) rather than the MP scheme in simulating extreme summer precipitation in the Western Black Sea region of Turkey. Accuracy of the datasets used as initial and lateral boundary conditions are also studied to minimize the errors in the WRF predictability. To address this issue, Zhou and Mu (2018) have compared Global Forecast System (GFS) and Final Analysis (FNL) reanalysis data produced by National Centers for Environmental Prediction (NCEP) throughout Ili region located in China. The outcomes showed that both datasets could catch the temporal movement of precipitation for the selected event, and there is no significant difference in using any of the two datasets as boundary conditions. Dyer et al. (2016) have examined the changes in the statistical dispersion of WRF ensembles in response to horizontal grid spacing values. Results of four different ensembles, which have 9 km, 15 km, 25 km, and 35 km horizontal grid spacing, are comparatively discussed. In brief, an inverse proportion has been detected between uncertainty and spatial resolution.

Each of above studies investigates the sensitivity of their WRF model configuration. However, until now, there is an apparent absence of a study encompassing a large ensemble that includes information about the impacts of physical parameterization, initial and lateral boundary data source, and spatial resolution on the extreme precipitation forecasts, and comprehensively interpreting the results through the ensemble mean approach for the events occurred in different climatic regions. Above studies so far either investigated the sensitivity of WRF-derived precipitation accuracy to model physics or initial and lateral boundary data source selection, but no study so far has investigated the sensitivity of the results to both factors comparatively. Furthermore, comparison of the abilities of modeling systems driven by reanalysis or forecast dataset is crucial for an early warning system since the reanalysis datasets have much longer latency and are not immediately available for operational use. However, no study so far comparatively evaluated the performances of WRF model driven by initial and lateral boundary conditions obtained from forecast and reanalysis datasets. It is also essential to understand the utility of the locally run WRF model with its optimum parameterization (the optimum refers to

the model parameterization that provides the best precipitation outputs) over the precipitation outputs compared against the initial and lateral boundary datasets.

1.2 Contribution of the WRF & WRF-Hydro coupling and satellite soil moisture initialization to the accuracy of hydrometeorological forecasts

A comprehensive understanding of the terrestrial water cycle, which is highly interconnected to the land surface interactions, becomes more of an issue with the changing climate (Yucel and Onen, 2014; Arnault et al., 2016; Rummler et al., 2022). One-dimensional (1D) Noah land surface model (LSM; Chen and Dudhia, 2001) is one of the most preferred LSM schemes in the WRF modeling studies (Hong et al., 2009; Efstathiou et al., 2013; Pennelly et al., 2014; Ekström and Gilleland, 2017; Arnault et al., 2019; Gao et al., 2022). Even though the 1D Noah LSM in the WRF handles the surface-atmosphere interaction described by diffusive exchange and radiative processes, it lacks hydrologically enhanced processes such as surface and sub-surface routing. Therefore, this may result in a poorer surface feedback system, particularly in complex terrain areas and high-resolution studies.

Moreover, a better representation of the LSM model not only provides a better contribution to the atmospheric model but also increases the quality of the LSM outcomes of the next time step due to the concurrent and interactive operation of the models. Therefore, the two-way coupling of the NWP models with a land surface model having an enhanced hydrologic model package is expected to improve both atmospheric and hydrologic outputs by investigating the feedback between the land and overlying planetary boundary layer, which results in a better presentation of the terrestrial water cycle (Ning et al., 2019). The WRF-Hydro (Gochis et al., 2018) is a 2-D hydrologic model aiming to enhance terrestrial water cycle simulation by focusing on surface overland flow, saturated subsurface flow, channel flow, and baseflow processes. The WRF-Hydro model can be run in uncoupled mode or two-way coupled (i.e., the feedback mechanism between the models is activated) to the WRF model.

The added value of coupling WRF with the WRF-Hydro hydrologic model on precipitation output is limited according to some studies (Senatore et al., 2015; Givati et al., 2016; Kerandi et al., 2018; Arnault et al., 2018; Rummler et al., 2019; Fersch et al., 2020; Zhang et al., 2021a). Senatore et al. (2015) claimed that the coupling effect on precipitation simulated over a MED coast is low because the primary precipitation moisture source comes from the MED sea not from the local soil moisture. Kerandi et al. (2018) and Arnault et al. (2018) stated that the coupled model did not improve the precipitation outcomes because the precipitation regime of their study area is mostly driven by the large-scale circulations, not by the local water cycle. Fersch et al. (2020) associated the slight improvement with selecting the innermost WRF domain too small, preventing reliable internal moisture recycling. Still, Givati et al. (2016), Naabil et al. (2017), and Wehbe et al. (2019) detected better simulation of summer extremes by the coupled model. This progress is because the WRF-Hydro model enhances the soil moisture outputs and thus the convective precipitation controlled by local latent heat fluxes. Moreover, a considerable number of the study showed that the amount of the soil moisture output increases with the WRF-Hydro coupling since the lateral distribution of the infiltrated water prevents the soils at higher elevations from being saturated, which also ends up with a decrease in the surface runoff amount (Senatore et al., 2015; Arnault et al., 2016; Fersch et al., 2020). In some cases, the increase in the soil moisture amount brings about overestimated intense precipitation with increased convectively available potential energy (cape) owing to the unstable convective environment originating from the strengthening of the latent heat flux (Lahmers et al., 2020; Wang et al., 2020; Zhang et al., 2021a; Zhang et al., 2021b).

The energy and water fluxes connecting the surface and the overlying atmosphere depend on the topsoil layer's moisture amount and distribution. For instance, soil moisture amount is critical in the allocation of total transferable energy between latent and sensible heat fluxes. With this aspect, it is one of the main moisture sources, especially for the convective summer extreme precipitation events over (semi)arid regions (Kerandi et al., 2018; Wang et al., 2018). In WRF-Hydro, soil

moisture at each level is used by the subsurface routing module and thus directly contributes to horizontal flows and river flows. In addition, as a result of irrigation works in agricultural areas of the basins, topsoil layer moisture amount unnaturally changes, and the model systems do not perceive these unexpected variations (Afshar et al., 2022). Therefore, forcing the coupled WRF/WRF-Hydro modeling system with a satellite-based topsoil layer moisture data and discussing the contribution of the updated soil moisture distribution to the (sub)surface flow outputs or the feedback to the overlying atmosphere and heavy precipitation formations is a subject that is open to exploration and is of great importance.

The effect of the initial state of soil moisture data on the WRF-derived latent and sensible heat flux, accordingly evapotranspiration, precipitation, and temperature, is tested considering dry & wet soil initial conditions (Vivoni et al., 2009; Zeng et al., 2014; Zhan et al., 2016; Xiang et al., 2018; Zhang et al., 2020a) or different models' soil moisture products (Hong et al., 2009; Dillon et al., 2016). Lin and Pu (2019) assimilated a remotely sensed product, Soil Moisture Active Passive level 4 (SMAP), into the standalone WRF with Noah LSM, which improved the hydrometeorological variables like humidity, surface soil moisture, and temperature. The impact of the same remote sensing data on the hydrologic outputs (i.e., surface soil moisture, streamflow) of the WRF-Hydro model is examined by Abbaszadeh et al. (2020). Among these studies mentioned above, only Xiang et al. (2018) conducted their study through the fully coupled WRF/WRF-Hydro model. Also, most of them checked the sensitivity of the WRF modeling system against soil moisture forcing data for the short-term events during the dry period and over arid/semi-arid regions, as well as neither of them focused on the initiation of the WRF/WRF-Hydro fully coupled system with a satellite soil moisture data.

1.3 The motivations of the study

Based on the information and the gaps defined in the above parts, this study basically consists of two different parts:

1-) To address the issues in Section 1.1, this study conducts a sensitivity analysis of physical parameterization, initial and lateral boundary condition dataset, and spatial resolution to construct a set of WRF models that are capable of simulating selected extreme precipitation events. WRF model with two nested domains (9 km and 3 km) configured by four MP, three CU, two PBL schemes, and two initial and lateral boundary forcings from ERA5 and GFS is integrated to simulate the two summer (dry) and two autumn (wet) events from two different climate and flood-prone regions of Turkey, namely; Eastern Black Sea (EBS) and MED. In addition to the discussion by means of the ensemble mean approach, the ranking of the success of each simulation member is provided. The influences of the model physics and initial and lateral boundary data sources on the WRF outputs are comparatively examined. The most successful model configurations are chosen from the ensemble to form a new smaller ensemble for each event, and the small ensembles are tested in the independent events that have the same spatiotemporal circumstances to validate the selections. The performances of these ensembles at the independent events are also compared with the ERA5-derived precipitation data to show the added value of WRF forecasts. With the intent of discussing the success of the convection-permitting simulations (i.e., the combinations with 3 km horizontal grid spacing), the results of 9 km and 3 km simulations are separately presented.

2-) In the second part, the effect of the feedback mechanism provided by hydrologically enhanced LSM with and without an initial soil moisture update is evaluated not only for precipitation formation but also for runoff, soil moisture, near-surface specific humidity, and temperature. The main motivation is to explore the relationship between the components of the terrestrial water cycle utilizing different model simulation cases. The analyses are repeated over a semi-arid (i.e., MED) and a humid (i.e., EBS) regions of Turkey and assessed for both short-term extremes and longer terms (i.e., monthly and yearly) to consider different climate and terrain conditions when evaluating the coupling and soil moisture update effects. Moreover, the standalone WRF-Hydro model is calibrated separately for hourly and daily streamflow data over EBS. In this way, it is shown whether the model calibration

performed using daily streamflow data is adequate in capturing hourly flow hydrographs of steeply-sloping and small watersheds of the EBS region. The calibration over MED is achieved based on Kling-Gupta efficiency (KGE; Gupta et al., 2009) and Nash-Sutcliffe efficiency (NSE; Nash and Sutcliffe, 1970) coefficients to see the decision coefficient influence on the selected parameter values of the hydrologic model. Then, calibrated standalone hydrologic models are forced by four different precipitation products (i.e., in-situ measurement, uncorrected radar, corrected radar, and WRF) and are validated under different spatiotemporal circumstances. In other words, another motivation of this study is to focus on the sensitivity of the WRF-Hydro parameters against the time scale of the observed streamflow data and the decision functions, as well as the sensitivity of the WRF-Hydro outputs to the precipitation forcing data products.

CHAPTER 2

MATERIALS AND METHODS

Sections 2.1 and 2.2 introduce the study areas and the atmospheric & hydrologic models used in that study. As explained before, the first part of the study conducts a sensitivity analysis of the WRF-derived precipitation to define the best model physics and initial and lateral boundary data source combinations capable of successfully simulating extreme events. The details of the first part are mentioned in Section 2.3. The second part discusses the contribution of the WRF-Hydro coupling to the hydrometeorological outputs of the WRF modeling system. Besides, the performance of the coupled model is tested when the system is initiated with the satellite soil moisture data. Section 2.4 clarifies the steps of the second part.

2.1 Study area

This study focuses on Turkey's MED and EBS regions, which have different climate types. For example, the EBS region prevails humid climate and receives rainfall throughout the year. However, MED is a typical representative of the Mediterranean climate (semi-arid, semi-humid) in which summers are hot and dry, and winters are cool and rainy (Türkeş, 1996). The EBS area is impacted by polar air masses with the continental origin of cold Siberian High, and maritime origin of Iceland Low in the winter and by subtropical air-masses (Azores High and part of Pakistan Low) in the summer (Duzenli et al., 2018). When the Siberian High crosses the Black Sea and approaches the northern coasts of Turkey, cold and dry air turn into a maritime continental air mass due to the acquired moisture content. MED is under the influence of mid-latitude depression (Icelandic and Mediterranean based low pressure) that produces cool and rainy weather in winter (Türkeş, 1996). Both maritime tropical air mass (Azores High) and continental tropical air masses are also

responsible for precipitation events. Both regions show a strong dependency on orographic lifting because of the existence of mountains parallel to the sea. Frequent moisture fluxes from sea to windward direction of the mountain throughout the year, particularly for the EBS region, favor the heavy precipitation events. Surface heating of complex topography in spring, summer, and fall seasons also triggers precipitation events through convection. The schematic demonstration and further information about the local and synoptic scale drivers of the climate over the regions are provided by Saris et al. (2010).

2.2 The modeling systems

2.2.1 WRF

NWP models are precious tools to monitor the interactions between the components of the hydrometeorological cycle, such as precipitation, temperature, (sub)surface runoff, soil moisture/temperature, and specific humidity. WRF model is an example of the new generation NWP models appropriate for long-term atmospheric research or short-term extreme weather event studies. It can be used for multiple purposes, including hindcasting, real-time numerical weather prediction, and regional climate modeling. The modeling system consists of two parts: WRF preprocessing system (WPS) and WRF (Figure 2.1). The former part, WPS, comprises three programs:

i) Geogrid: This program specifies the model domain and interpolates the input geographical data to this domain. Also, map projection of the study area is specified by using this program (Lambert conformal conic projection (LCC) is chosen for this study since LCC is the recommended projection type for the mid-latitudes). The geogrid program allows the users to form nested model domains, making simulations with high spatial resolution possible for the specific areas in a shorter run time.

ii) Ungrib: Input meteorological data for the WRF model are generally in GRIB data format (i.e., a file format to store the meteorological data). The ungrib program

extracts the GRIB-formatted meteorological data to the simple data format used by the WRF model called as intermediate data format. This process makes the meteorological data useable for the metgrid program.

iii) Metgrid: The meteorological input data extracted by the ungrib program are horizontally interpolated to the model domains determined by the geogrid program.

After the preprocessing is completed, the second component of the modeling system, WRF, can be initiated. The WRF component composes of two parts:

i) Real: The real program reads the input data prepared by the WPS and forms the initial and lateral boundary condition files to force the WRF model. In addition to the horizontal interpolation in the WPS part, input data are also interpolated in the vertical direction (i.e., along the vertical column of the domain grids).

ii) WRF: This is the main program where; dynamical downscaling occurs using the initial and lateral boundary condition data. The non-hydrostatic WRF modeling system sequentially solves the atmosphere using dynamics and physics consisting of CU, MP, PBL, radiation, and surface physics that are interactive through model integration. It is worthwhile to state that surface physics is divided into an atmospheric surface layer and an LSM. Direct interactions between the model physics can be followed in Figure 2.2.

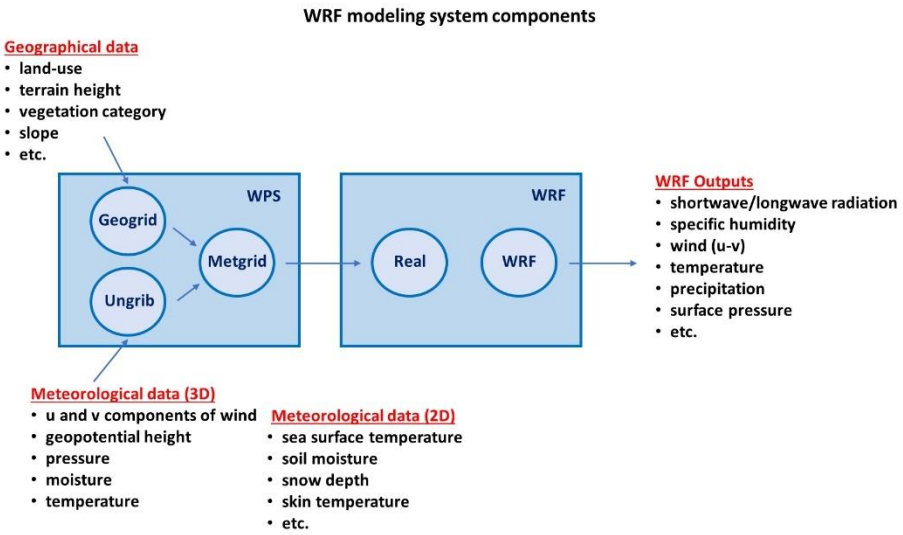

Figure 2.1. Workflow and components of the WRF modeling system

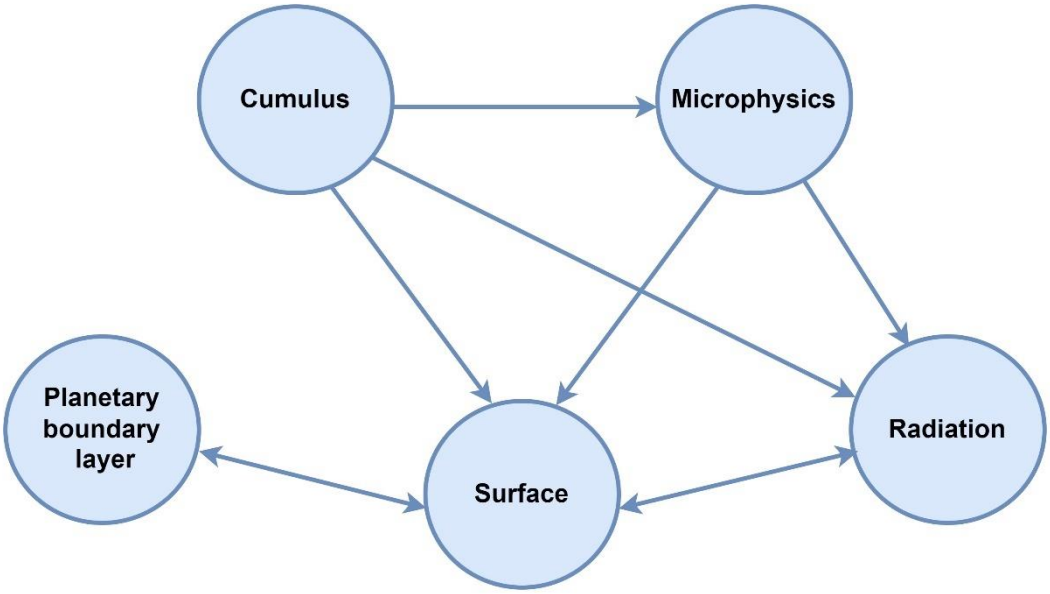

Figure 2.2. Direct interactions between the model physics. The arrows show the direction of the impact. The figure is formed based on the information by Dudhia (2014).

2.2.2 WRF-Hydro

The WRF-Hydro hydrologic model is an extended version of the traditional 1D Noah LSM and developed to simulate the corresponding water cycle more robustly. It can be run in standalone mode or fully coupled with the WRF atmospheric model. In 1D Noah LSM, the infiltration excess in a vertical grid column is directly assigned as the surface runoff. This excess water is considered the sink term, which does not affect the calculations of the next time step. However, the WRF-Hydro model can laterally redistribute the (sub)surface water based on high-resolution topographical data via its (sub)surface routing options. Also, the surface runoff in WRF-Hydro is a state variable (contrary to the sink term, state variables affect the system's future behavior) instead of just being a sink term. The subsurface routing is performed first to allow for possible exfiltration during the routing processes. Through the disaggregation algorithm developed by Gochis and Chen (2003), the soil moisture and surface head variables are routed at higher resolutions than the Noah LSM horizontal grid spacing. The streamflow is fed by the surface runoff, subsurface runoff from the soil layers, and underground runoff from the buckets (if activated). Lateral distribution of the (sub)surface water at higher resolutions is prospective to cause a better partitioning of the terrestrial water budget as the model can illustrate more detailed mesoscale orography and land surface heterogeneities (Givati et al., 2016; Cerbelaud et al., 2022). The schematic representation of the processes in WRF-Hydro is demonstrated in Figure 2.3.

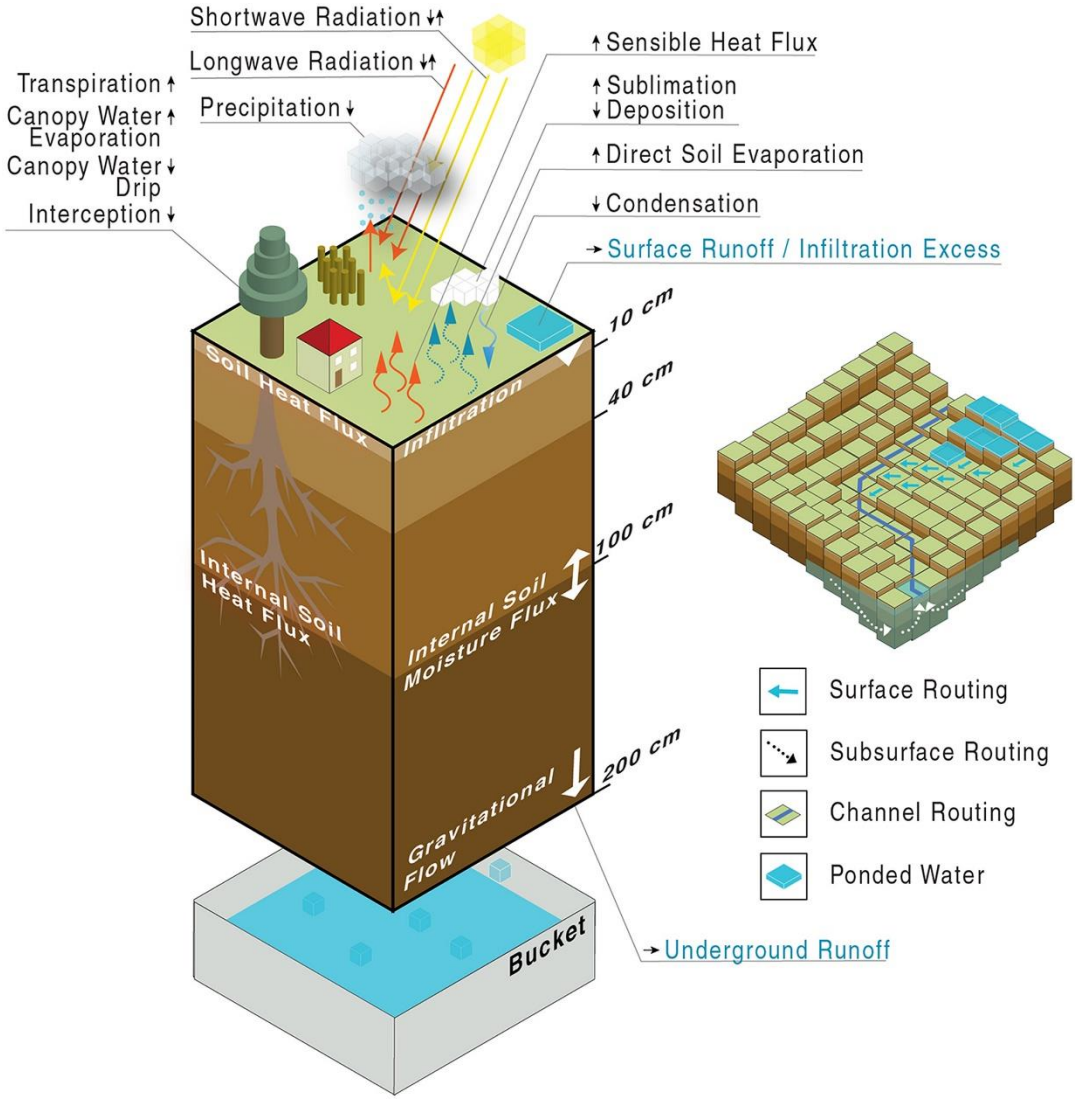

Figure 2.3. Demonstration of the processes in a single soil column in WRF-Hydro. The figure is retrieved from Rummler et al. (2019)

2.3 Sensitivity of the extreme precipitation simulation capability of the WRF model against model physics and initial and lateral boundary data source

This section focuses on the data, methods, and model configurations used for the sensitivity analysis. Even though the details about the steps of the study can be found

in the subsections of Section 2.3, a summary of the work is also provided in Figure 2.4.

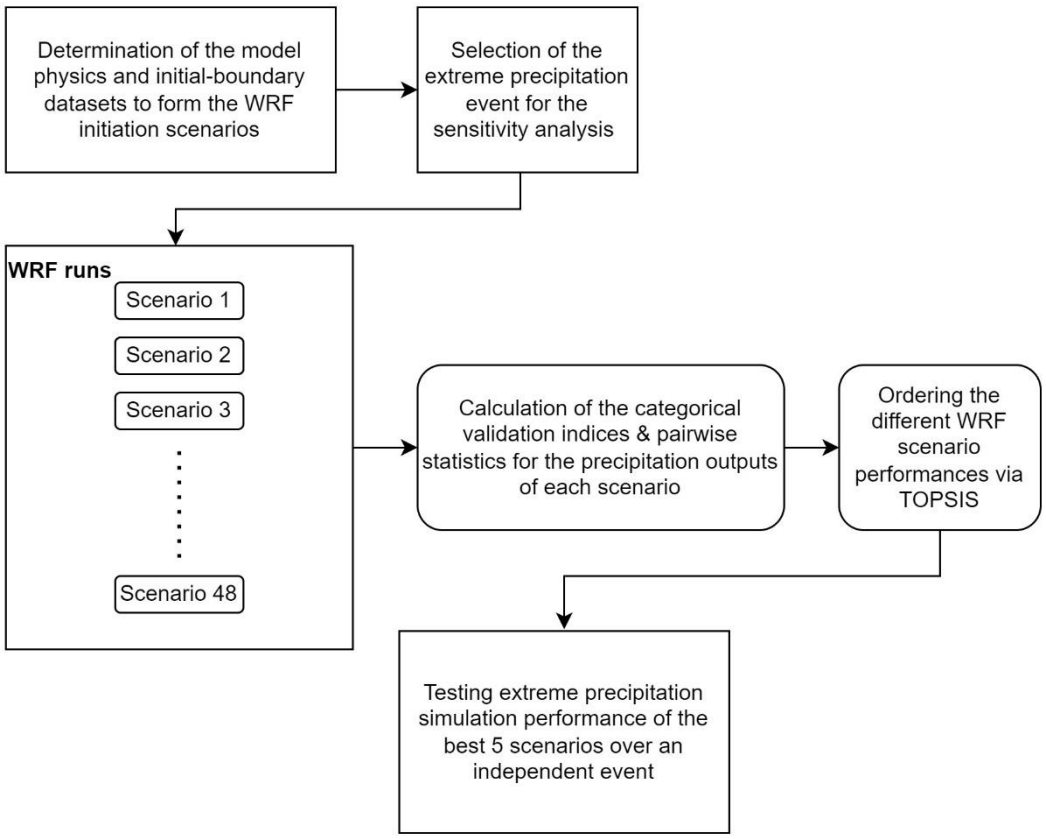

Figure 2.4. Summary of the sensitivity analysis. This process is repeated for each spatial resolution used as well as each extreme precipitation event selected for the corresponding season and region.

2.3.1 Observational data

There are above 2000 automated weather observation systems (AWOS) stations over the country maintained by the General Directorate of Meteorology (MGM) in Turkey. For this study, MGM provided hourly precipitation and temperature records of 159 AWOS stations for the period of 01/01/2008 - 31/12/2017 (109 of them is in EBS and 50 of them is in MED). Two basic problems are foreseen related to the data quality of these gauges. First, some of the stations are eliminated since all data of

them were recorded as zero. After this process, 46 and 99 stations are operational for MED and EBS, respectively (Figure 2.5-B, blue points). Second, some stations are omitted from the analyses as their not available (NA) data amount is too high to conduct the analyses. However, the NA amount is not checked for the 10-year data. The reason is that the study focuses on short term extreme events. The availability of the data for the simulation period is sufficient. Hence, instead of entire datasets, NA amount criteria are verified for each of the events separately. The stations, at which the NA ratio exceeds 5% of whole data of the simulation period, are not included among the stations used for the performance measure study of the corresponding event.

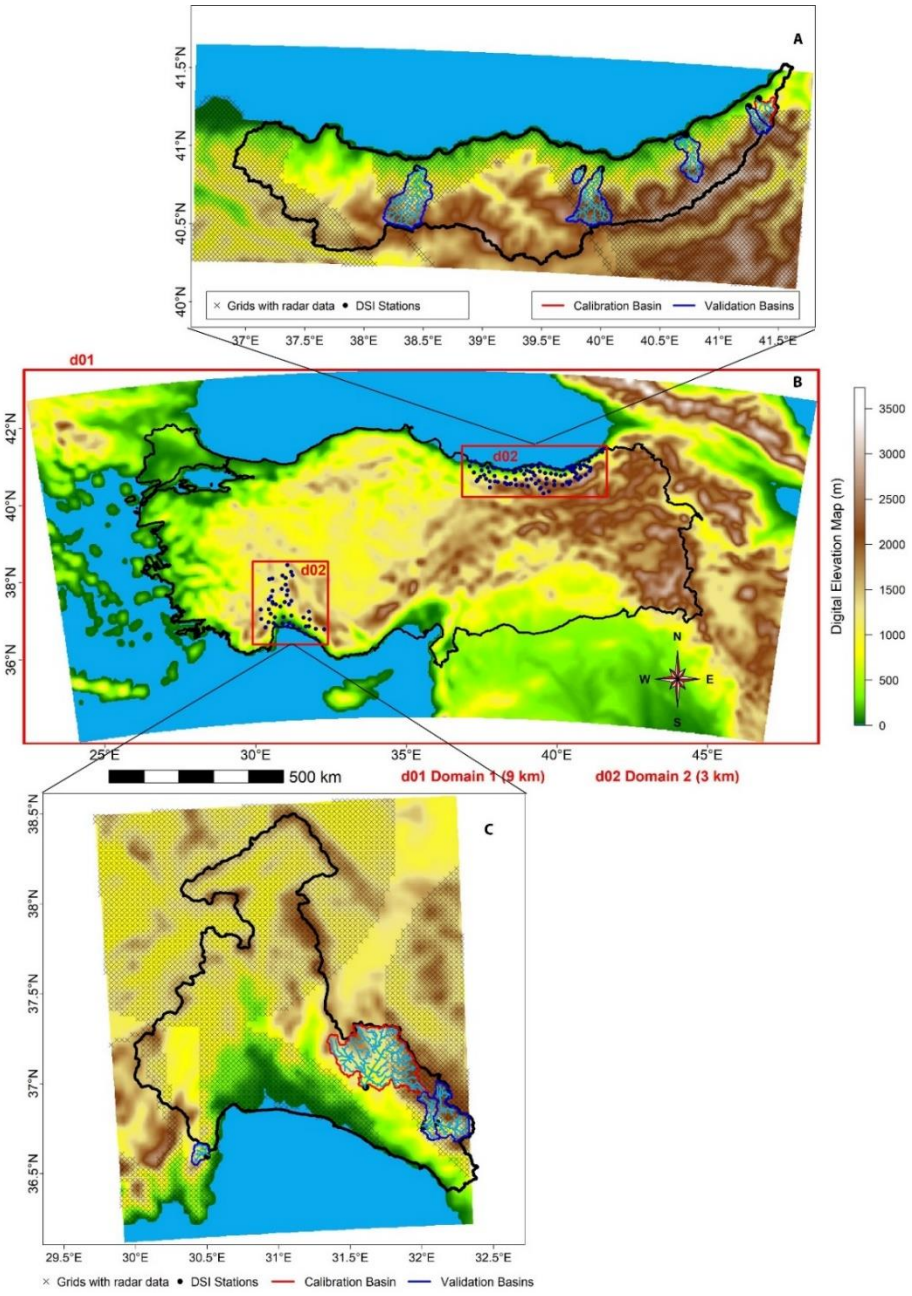

Figure 2.5. Panel B shows the WRF domains for both regions; d01: the parent domain, d02: the child domains. The WRF-Hydro model with 250 m horizontal grid spacing is operated over child domains. Panel A and Panel C provides detailed information over the (sub)basins defined for EBS and MED regions, respectively. Background of the maps: digital elevation model (DEM) provided by MODIS. Dashed areas in panels A and C show coverage of radar echos. The figure is obtained using R-programming language (R Core Team, 2020).

2.3.2 Selection of the events

MGM also records the extraordinary meteorological events that occur throughout Turkey each year based on the observations acquired over AWOS stations. As the main criteria, MGM considers the magnitude of the damage due to these events when selecting and recording. A total of 62 and 100 extreme events are acquired from MGM for MED and EBS regions between 01/01/2008 and 31/12/2017 (Table 2.1) where these acquired records are tagged as heavy rain and/or flood. During this period, the highest number of events for MED and EBS regions are observed in autumn (23) and summer & autumn (45 and 38), respectively. Even though the number of summer events is approximately the same as the winter and spring events for the MED region, the summer events in this area are relatively complex to solve due to their convection-dominant nature. Accordingly, two events per region, one from summer and one from autumn, are chosen, and the sensitivity analyses are performed for each case to show the temporal variability aside from spatial variation. Among the total 162 events (Table 2.1), 8 events are used in this study: 4 of them are from summer and 4 are from autumn, 4 of them are for EBS and 4 of them are for MED, 4 are selected for calibration and 4 are for independent validation (details about these 8 events are given below in Table 2.2). Here, the calibration indicates the events used for the sensitivity analyses to specify the best model physics and initial and lateral boundary data source combinations for simulating extreme precipitation.

Table 2.1 Number of the extreme precipitation/flooding events with respect to the years and the seasons. Spring: From 21 March to 20 June. Summer: From 21 June to 22 September. Autumn: From 23 September to 20 December. Winter: From 21 December to 20 March

	MED Region				EBS Region			
	Spring	**Summer**	**Autumn**	**Winter**	**Spring**	**Summer**	**Autumn**	**Winter**
2008	0	1	0	0	1	6	0	0
2009	0	1	5	3	2	13	7	1
2010	0	0	4	4	2	4	2	1
2011	3	0	1	0	0	3	4	0
2012	2	0	1	3	0	4	6	0
2013	0	1	1	1	2	3	1	1
2014	1	1	5	1	0	3	4	0
2015	1	2	2	1	4	4	6	0
2016	0	1	0	0	0	4	3	0
2017	7	5	4	0	2	1	5	1
Total	**14**	**12**	**23**	**13**	**13**	**45**	**38**	**4**
General Total	**62**				**100**			

Considering the precipitation regimes of the regions, spatially smaller scale short-term extreme cases reflect the typical features of the summer events, while the spatially larger scale and long-term extreme events exemplify the autumn events. The events selected for the calibration are used for the sensitivity analysis of the WRF model. Table 2.2 gives some characteristics of the selected events: date of the event, maximum hourly rainfall amount in the event center, cumulative rainfall amount of the event center for the simulation period, the hour at which maximum hourly precipitation occurred (i.e., peak hour), number of the stations passed the event-based quality control (stations, at which the not available (NA) data length exceeds 5% of the whole simulation period, are omitted for the corresponding event) and percent of the rainy data (the records higher than 0.3 mm is assumed as rainy). It is noted that the percent of the rainy data parameter (%) shows how many of the records are rainy. For instance, 75 stations pass the quality control procedure for the

event dated 21.09.2016. So, a total of 5475 (i.e., 75 stations * 73 h = 5475 h) hours of data are recorded for the incident. Table 2.2 indicates that the records at 23% of 5475 hours are higher than 0.3 mm.

Additionally, calibration and validation events (Table 2.2) are selected to have similar spatial and temporal characteristics, so that the adaptability of the results of the sensitivity analysis is tested in the independent events. For the validation events of the EBS-summer and MED-autumn, the simulations continue six days because of the several successive precipitation events that follow each other.

Table 2.2 The characteristics of the selected events used in model calibration and validation

	Starting date of the run	Run Time	Region	Center station	Lat (°)	Long (°)	Max hourly precip (mm)	Cum precip (mm)	Peak hour	Number of stations	%
Calibration Events	20.09.2016	3 days	EBS	18231	41.0328	39.2144	81.1	299.7	34	75	23
	13.11.2016	3 days	EBS	19059	40.9758	41.1125	40.1	398	31	87	27
	29.08.2017	3 days	MED	18844	37.5242	31.1881	59.2	66.2	38	34	4
	26.11.2017	3 days	MED	17954	36.7895	31.441	29.6	163.2	68	43	28
Validation Events	21.08.2015	6 days	EBS	18554	41.3166	41.2928	36.9	315.3	26	77	12
	13.10.2015	3 days	EBS	17800	40.9898	40.6083	39.8	169.8	37	24	37
	30.07.2015	3 days	MED	17927	37.0968	31.5952	22.6	34.2	44	34	3
	20.10.2015	6 days	MED	17954	36.7895	31.441	78.2	268.4	71	35	21

Figure 2.6 depicts the accumulated precipitation and the temperature variations from AWOS stations during the 73-hour simulation period for the calibration events. The steep increase of the cumulative precipitation line and the instantaneous drop of temperature just before the peak hour reveal the convection-dominant nature of the summer events. Especially for MED, percent of rainy data is very low, and 59.2 mm of a total 66.2 mm rainfall at the central station (station # 18844) occurs just in 1 hour (Figure 2.6). These also support the inference that the convective factors trigger

the event. For autumn, the milder slope of the cumulative precipitation lines proves the longevity of the events in comparison to summer.

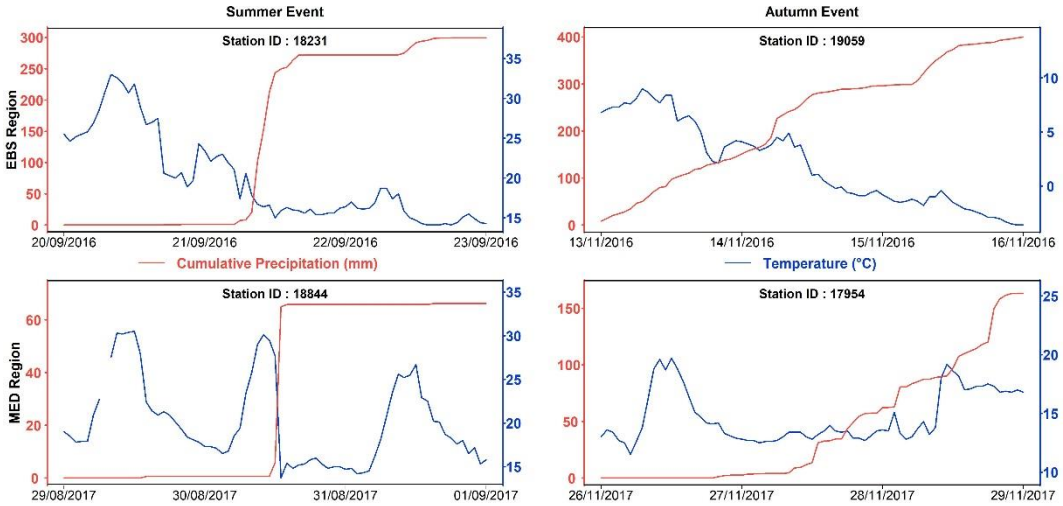

Figure 2.6. The time-series of the observed precipitation and temperature for the central stations of the calibration events for the simulation period

2.3.3 Model configuration

The physics-based ensemble simulations are generated using the WRF system with Advanced Research WRF version 4.0 developed at the National Center of Atmospheric Research (NCAR; Skamarock et al., 2019) The MP, CU, and PBL schemes are alternated in the ensemble and described in Section 2.3.3.1 while all experiments use the unified Noah land surface model, Dudhia short- and RRTM long-wave radiation schemes, and Eta & MM5 similarity surface layer schemes. Herein, it is substantial to note that the usage of the surface layer scheme depends on the used PBL scheme. In this study, the sensitivity of two different PBL schemes, Yonsei University Scheme (YSU) and Mellor–Yamada–Janjic Scheme (MYJ), are tested. According to the WRF working algorithm, when the PBL scheme is selected as MYJ, the surface layer option has to be selected as the Eta similarity scheme. However, the YSU option is not compatible with this surface layer option.

Each simulation is a nested run (two-way nesting) with the spectral nudging of the parent domain (d01). The spatial resolutions of the outer and inner domains are 9 km and 3 km, respectively. The areas covered by the domains (d01 & d02) together with elevation distribution are shown in Figure 2.5-B. The outer domain is situated between the coordinates of 23.5°E-47.5°E and 34.5°N- 43.5°N with 232 x 111 grid points. It extends further from the national border of Turkey to account for weather systems under the influence of synoptic-scale circulations that originate overseas (Türkeş and Erlat, 2003; Givati and Rosenfeld, 2013). Two inner domains shown with red frames (d02) in Figure 2.5-B have 73 x 88 grid points and 136 x 52 grid points for the MED and EBS regions, respectively. As stated in the literature, the input variables are expected to have a remarkable impact on WRF outputs. Accordingly, the products of the National Oceanic and Atmospheric Administration (NOAA) and European Centre for Medium-Range Weather Forecasts (ECMWF) are employed as initial and lateral boundary conditions and the sensitivity of the model against data sources are deliberated for different spatiotemporal conditions. NCEP GFS Global Forecast Grids (NOAA, 2015) contains the forecasts for the upcoming 16 days with a 0.25° horizontal grid spacing. The temporal resolution is 3 hours for the first ten days and 12 hours for the last six days. Alternatively, ERA5 data, the successor to ERA-Interim, originated by ECMWF atmospheric reanalysis, provides hourly reanalysis data from 1979 to present with 0.25° spatial resolution. Data are available at 137 model levels in the vertical direction. The vertical resolution of the WRF models in this study is 40 atmospheric levels spaced closer together in the PBL. Each WRF simulation starts from a day before the event day to get rid of spin-up time error, and lasts until a day after, including the midnights.

2.3.3.1 Physics ensemble design

Multiple options for most physics parameterizations that are actual model representations of sub-grid scale processes are available in the WRF system. The implementation of various physics schemes, as well as their interactions, causes a

considerable variation in the forecast output (Zhang et al., 2006). The key parameterization of CU convection, MP, and boundary layer are examined to return the best configuration that would produce reliable precipitation simulation for selected rainfall events. Here we investigate the performance of different options in three physics schemes to simulate two storms occurring over MED and two storms occurring over EBS regions in Turkey. The physics schemes tested are the MP scheme, the CU scheme, and the PBL scheme.

The MP scheme is mainly responsible for the cloud formation and water particle action, as well as specifies the interactions between the atmosphere and the surface (ElTahan and Magooda, 2017). The scheme plays a vital role in the estimation of non-convective large-scale precipitation. Four different MP schemes are selected to be tested in this study. These are Kessler Scheme (KS), Eta (Ferrier) Scheme (ES), WRF Single–moment 6–class Scheme (WSM6), and Aerosol–aware Thompson Scheme (AATS). KS is the oldest MP scheme of WRF, which considers the air circulations in two-dimension (Mielikainen et al., 2013). It calculates the values of water vapor, cloud water, and rainfall in response to microphysical processes (Kessler, 1995). ES assesses two more condensed matters: small ice crystals, and precipitation ice like snow, graupel, or sleet (Ferrier et al., 2002). WSM6 explores the processes of water vapor, cloud water, cloud ice, snow, rain, and graupel (Hong and Lim, 2006). AATS algorithm utilizes the same water particles with WSM6. Additionally, this algorithm takes the aerosols (their size and spread in the air) into account while generating cloud and precipitation (Thompson and Eidhammer, 2014).

The CU scheme determines the convective fluxes and resulting phase modulation of water (e.g., from gas to liquid or vice versa) on individual columns where the scheme is triggered. In general, the estimation of convective rainfall is directed by the choice of CU scheme. This study involves Kain–Fritsch Scheme (KF), Betts–Miller–Janjic Scheme (BMJ), and Grell–Freitas Ensemble Scheme (GFES). KF searches for the instabilities, which may cause the forming of a CU cloud by concentrating on mass fluxes (Kain, 2004). On the other hand, BMJ is not a mass flux scheme; it deduces the convective processes from the reference temperature and moisture profiles

(Janjić, 1994). These profiles are constituted in the wake of a vast number of observations (Vaidya and Singh, 2000). A procedure (Grell and Dévényi, 2002), including an ensemble probability density function and a data assimilation technique, underlies the working mechanism of the GFES scheme (Grell and Freitas, 2013). All of the selected CU parametrization schemes can simulate both deep and shallow convection phenomena.

The PBL tied to the surface layer determines the vertical sub-grid fluxes due to eddy transports in the atmospheric column. Along with the cloud formation and chemistry, a thorough understanding of the interaction between the atmosphere and the Earth surface is a vital issue to consider in order to increase the performance of NWP models. From this point of view, PBL schemes trace the turbulent vertical mixing of thermodynamic and kinematic profiles such as heat, momentum, or the atmospheric constituents like moisture (Hu et al., 2010). The influences of the YSU and MYJ on WRF-derived precipitation are measured in this study.

In total, 24 ensemble members (i.e., scenarios) based on physics are generated for each case study region. However, since each of these 24 members is performed using two datasets for initial and lateral boundary conditions (GFS and ERA5), 48 scenarios are formed for the sensitivity analysis (Table 2.3). It is worthy to remark that no CU option is used for 3 km domain runs since the MP scheme is sufficiently capable of solving convective processes at a finer resolution (Hsiao et al., 2013; Pennelly et al., 2014). Finally, for the validation events, the five best scenarios for the 3 km and 9 km analyses (i.e., a total of 10 scenarios) are selected from the ensembles of the sensitivity analysis for each calibration event.

Table 2.3 MP, CU, PBL, and initial and lateral boundary datasets selections for the scenarios used in the sensitivity analysis.

Scenario Number	MP	CU	PBL	Initial
1	KS (1)	KF (1)	YSU (1)	GFS
2	ES (5)	KF (1)	YSU (1)	GFS
3	WSM6 (6)	KF (1)	YSU (1)	GFS
4	AATS (28)	KF (1)	YSU (1)	GFS
5	KS (1)	BMJ (2)	YSU (1)	GFS
6	ES (5)	BMJ (2)	YSU (1)	GFS
7	WSM6 (6)	BMJ (2)	YSU (1)	GFS
8	AATS (28)	BMJ (2)	YSU (1)	GFS
9	KS (1)	GFES (3)	YSU (1)	GFS
10	ES (5)	GFES (3)	YSU (1)	GFS
11	WSM6 (6)	GFES (3)	YSU (1)	GFS
12	AATS (28)	GFES (3)	YSU (1)	GFS
13	KS (1)	KF (1)	MYJ (2)	GFS
14	ES (5)	KF (1)	MYJ (2)	GFS
15	WSM6 (6)	KF (1)	MYJ (2)	GFS
16	AATS (28)	KF (1)	MYJ (2)	GFS
17	KS (1)	BMJ (2)	MYJ (2)	GFS
18	ES (5)	BMJ (2)	MYJ (2)	GFS
19	WSM6 (6)	BMJ (2)	MYJ (2)	GFS
20	AATS (28)	BMJ (2)	MYJ (2)	GFS
21	KS (1)	GFES (3)	MYJ (2)	GFS
22	ES (5)	GFES (3)	MYJ (2)	GFS
23	WSM6 (6)	GFES (3)	MYJ (2)	GFS
24	AATS (28)	GFES (3)	MYJ (2)	GFS
25	KS (1)	KF (1)	YSU (1)	ERA5
26	ES (5)	KF (1)	YSU (1)	ERA5
27	WSM6 (6)	KF (1)	YSU (1)	ERA5
28	AATS (28)	KF (1)	YSU (1)	ERA5
29	KS (1)	BMJ (2)	YSU (1)	ERA5
30	ES (5)	BMJ (2)	YSU (1)	ERA5
31	WSM6 (6)	BMJ (2)	YSU (1)	ERA5
32	AATS (28)	BMJ (2)	YSU (1)	ERA5
33	KS (1)	GFES (3)	YSU (1)	ERA5
34	ES (5)	GFES (3)	YSU (1)	ERA5
35	WSM6 (6)	GFES (3)	YSU (1)	ERA5
36	AATS (28)	GFES (3)	YSU (1)	ERA5
37	KS (1)	KF (1)	MYJ (2)	ERA5
38	ES (5)	KF (1)	MYJ (2)	ERA5
39	WSM6 (6)	KF (1)	MYJ (2)	ERA5
40	AATS (28)	KF (1)	MYJ (2)	ERA5
41	KS (1)	BMJ (2)	MYJ (2)	ERA5
42	ES (5)	BMJ (2)	MYJ (2)	ERA5
43	WSM6 (6)	BMJ (2)	MYJ (2)	ERA5
44	AATS (28)	BMJ (2)	MYJ (2)	ERA5
45	KS (1)	GFES (3)	MYJ (2)	ERA5
46	ES (5)	GFES (3)	MYJ (2)	ERA5
47	WSM6 (6)	GFES (3)	MYJ (2)	ERA5
48	AATS (28)	GFES (3)	MYJ (2)	ERA5

2.3.3.2 Performance statistics

In total nine accuracy statistics (Probability of Detection, POD; False Alarm Ratio, FAR; Critical Success Index, CSI; Percent Correct, PC; Frequency Bias Index, FBI; Root Mean Square Error, RMSE; Mean Bias Error, MBE; Standard Deviation Ratio, SD; Pearson Correlation Coefficient) from two different metric groups (categorical metrics and pairwise statistics) are utilized to specify the hierarchy between the scenarios (Table 2.4). Categorical metrics inform about the precipitation detection capacity of the model, while pairwise statistics measure the goodness of the model in forecasting the total amount and trend (Toté et al., 2015). The values of the metrics are calculated between each station and the closest WRF grid to that station. For instance, for a scenario of an event having 75 available stations with sufficient quality, a total of 75 values are calculated for each metric. Determination of the best scenarios for the entire region is based on the average of these 75 values since the stations are almost uniformly distributed over the regions. In other words, scenarios are rated regarding the nine distinct metrics mean values calculated for each scenario. Nevertheless, ordering the combinations on the basis of these nine values requires the usage of a multi-criteria decision-making method. The Technique for Order of Preference by Similarity to Ideal Solution (TOPSIS; Hwang and Yoon, 1981) method is used to fulfill the requirement. The method identifies relatively the best and the worst ideal alternatives by normalizing the input metrics. Afterward, the distances between the metric value and the ideal best/worst solutions of the corresponding metric are calculated for each scenario. Finally, the TOPSIS algorithm ranks the scenarios with respect to the closeness to the best and the remoteness to the worst alternatives.

Before operating the TOPSIS algorithm, the weight and the impact direction of the individual metrics are assigned. The weight denotes the magnitude of the influence of a metric on the resulting decision. For this study, weights are equally appointed to all metrics. The impact direction indicates whether the convergence of a scenario to the best ideal solution is caused by an increase or a decrease in a metric. The

relationship between the convergence and a metric must always be the same, either linearly positive or negative, for any range. In other words, the best value of the metrics should be either the minimum or the maximum value the metric can take. So, the FBI, MBE, and SD are rescaled (Table 2.4). It is precious to note that the rescaled values of the metrics are merely used to manipulate the TOPSIS algorithm. All other interpretations are made considering the real (i.e., not rescaled) values.

Table 2.4 Characteristics of the categorical metrics and pairwise statistics. A: Number of Correct Detection, B: Number of False Alarms, C: Number of Misses, D: Number of Correct Negative, E: Total forecast number (73)

Name	Group	Possible Range	Perfect Score	Rescaled Range	Impact Direction	Rescaling Method
POD = $\frac{A}{A+C}$	Categorical	0 to 1	1	x	+	x
FAR= $\frac{B}{A+B}$	Categorical	0 to 1	0	x	-	x
CSI= $\frac{A}{A+B+C}$	Categorical	0 to 1	1	x	+	x
PC= $\frac{A+D}{E}$	Categorical	0 to 1	1	x	+	x
FBI= $\frac{A+B}{A+C}$	Categorical	0 to ∞	1	0 to 1	+	**A)** If FBI[i]>2, FBI[i]=0 **B)** If 2>FBI[i]>1, FBI[i]=2-FBI[i] **C)** If FBI[i]<1, FBI[i]= FBI[i]
RMSE	Pairwise	0 to ∞	0	x	-	x
MBE	Pairwise	-∞ to ∞	0	0 to ∞	-	MBE[i]=|MBE[i]|
SD	Pairwise	-∞ to ∞	1	0 to 1	+	**A)** If SD[i]>2, SD[i]=0 **B)** If 2>SD[i]>1, SD[i]=2-SD[i] **C)** If SD[i]<1, SD[i]= SD[i]
Correlation	Pairwise	-1 to 1	1	x	+	x

2.4 Contribution of the WRF & WRF-Hydro coupling and satellite soil moisture initialization to the accuracy of hydrometeorological forecasts

Within the scope of this section, 4 different long-term simulations are performed as follows:

1. **WRF-SA**: The standalone WRF model including traditional 1D Noah LSM

2. **WRF-Hydro-SA**: The standalone WRF-Hydro model, which is calibrated and validated with the meteorological input derived from the WRF-SA

3. **WRF-Coup**: The fully coupled WRF/WRF-Hydro modeling system operated with calibrated WRF-Hydro parameters

4. **WRF-Coup-SM**: The fully coupled WRF/WRF-Hydro modeling system operated with calibrated WRF-Hydro parameters and initiated with SMAP product

The temporal coverage of the simulations is shown in Figure 2.7. The details of these runs and model setups are explained in the following sub-sections.

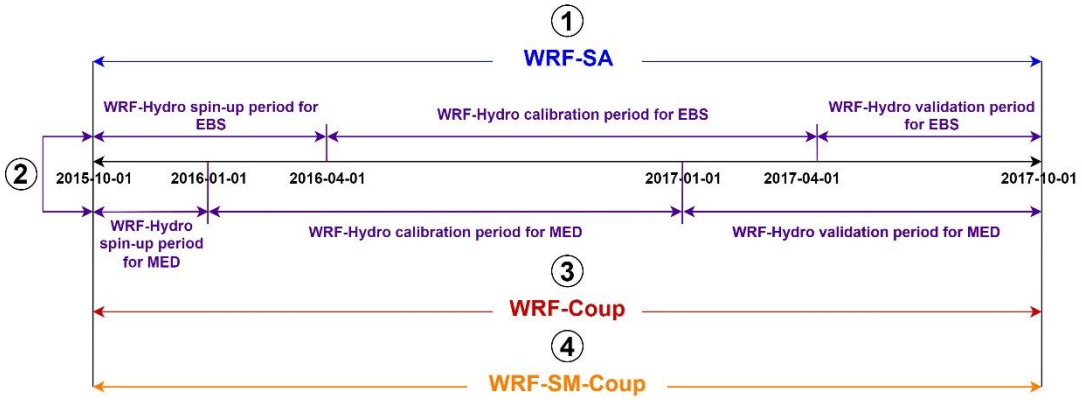

Figure 2.7. Temporal coverage of the models

2.4.1 WRF-SA

The WRF-SA model is run over two areas (i.e., EBS and MED) to compare its performance with the coupled models and produce meteorological input variables for the WRF-Hydro-SA model for a long-term period. Study areas of the WRF-SA models for EBS and MED are designed as two nested domains (Figure 2.5-B). The models' initial and lateral boundary conditions are provided by GFS data. However, according to Pilatin et al. (2021), the lower boundary of the WRF model applied over the Black Sea region is better represented with the use of high-resolution sea surface temperature (SST) from NCEP data. Therefore, for initial and time-continuous boundary conditions, NCEP-SST data are used instead of SST data of GFS. The CU, MP, and PBL schemes (Table 2.5) of the WRF-SA models are selected according to the outputs of the sensitivity analysis (i.e., the scenario introduced in Section 2.3 and Duzenli et al. (2021), which gives the best precipitation output). The CU physics are not initiated for the convection-permitting child domains. The model's time step for solving dynamic and physical equations is 54 seconds for the parent domain (d01) and 18 seconds for the child domain (d02). The models consist of 40 vertical levels, and the pressure in the topmost level is 5 kPa.

Table 2.5 The physics used in long-term WRF simulations with respect to the regions. The CU physics are not initiated for the child domains (i.e., the physics marked in red show the CU used not in the inner domain, but in the outer domain operated simultaneously).

Physics	**EBS**	**MED**
MP	WSM6 (WRF Single–moment 6–class Scheme)	ES (Eta (Ferrier) Scheme)
CU	GFES (Grell–Freitas Ensemble Scheme)	GFES
PBL	YSU (Yonsei University Scheme)	MYJ (Mellor–Yamada–Janjic Scheme)
Shortwave radiation scheme	Dudhia short-wave radiation scheme	Dudhia short-wave radiation scheme
Longwave radiation scheme	RRTM long-wave radiation scheme	RRTM long-wave radiation scheme
Land surface model	Noah land surface model	Noah land surface model
Surface model	Eta & MM5 similarity surface layer schemes	Eta & MM5 similarity surface layer schemes

2.4.2 WRF-Hydro-SA

2.4.2.1 Selection of the calibration and validation subbasins

General Directorate of State Hydraulic Works (DSI) provided the daily streamflow data for the stream gauges in EBS and MED. The subbasin corresponding to each stream gauge is delineated using the ArcGIS preprocessing tool (Sampson and Gochis, 2018). The elevation data for this process is retrieved from the Hydrological data and maps based on Shuttle Elevation Derivatives at multiple Scales (HydroSHEDS) that have 3 arc-second (~90m) spatial resolutions.

The EBS basin consists of many small and steeply elevated subbasins owing to its complex and steep-sided topography. Because of these geographical features, the hydrological response in the region's subbasins is rapid against sudden and excessive precipitation events. Therefore, it is worthwhile to calibrate the WRF-Hydro model for the EBS region not only according to daily data but also according to hourly data and to discuss the possible differences between the values of calibrated parameters. Hence, the calibration of the WRF-Hydro model for the EBS region is separately achieved for daily and hourly streamflow data over the Arhavi subbasin (Figure 2.5-A, red subbasin), which has hourly streamflow data as well as daily. The calibrated values of the parameters acquired from the calibration of the Arhavi subbasin are validated for both red and blue subbasins in Figure 2.5-A. Calibration of the WRF-Hydro model for the MED region is performed over the Oymapınar subbasin (Figure 2.5-C, red subbasin), and the calibrated model is validated for both the red and blue subbasins shown in Figure 2.5-C. At least one subbasin adjacent to the calibration subbasins is incorporated among the subbasins selected for the validation. The time series of the calibration basins are provided in Figure 2.8.

The spatial resolution of the WRF-Hydro model run over the d02 domains (Figure 2.5) is chosen as 250 m. The model terrain comprises four different soil layers of 10, 30, 60, and 100 cm from the surface to the ground. All routing modules (surface, subsurface, and channel) and baseflow bucket model are activated. The time step is 15 seconds for the terrain routing and 300 seconds for the channel routing operations.

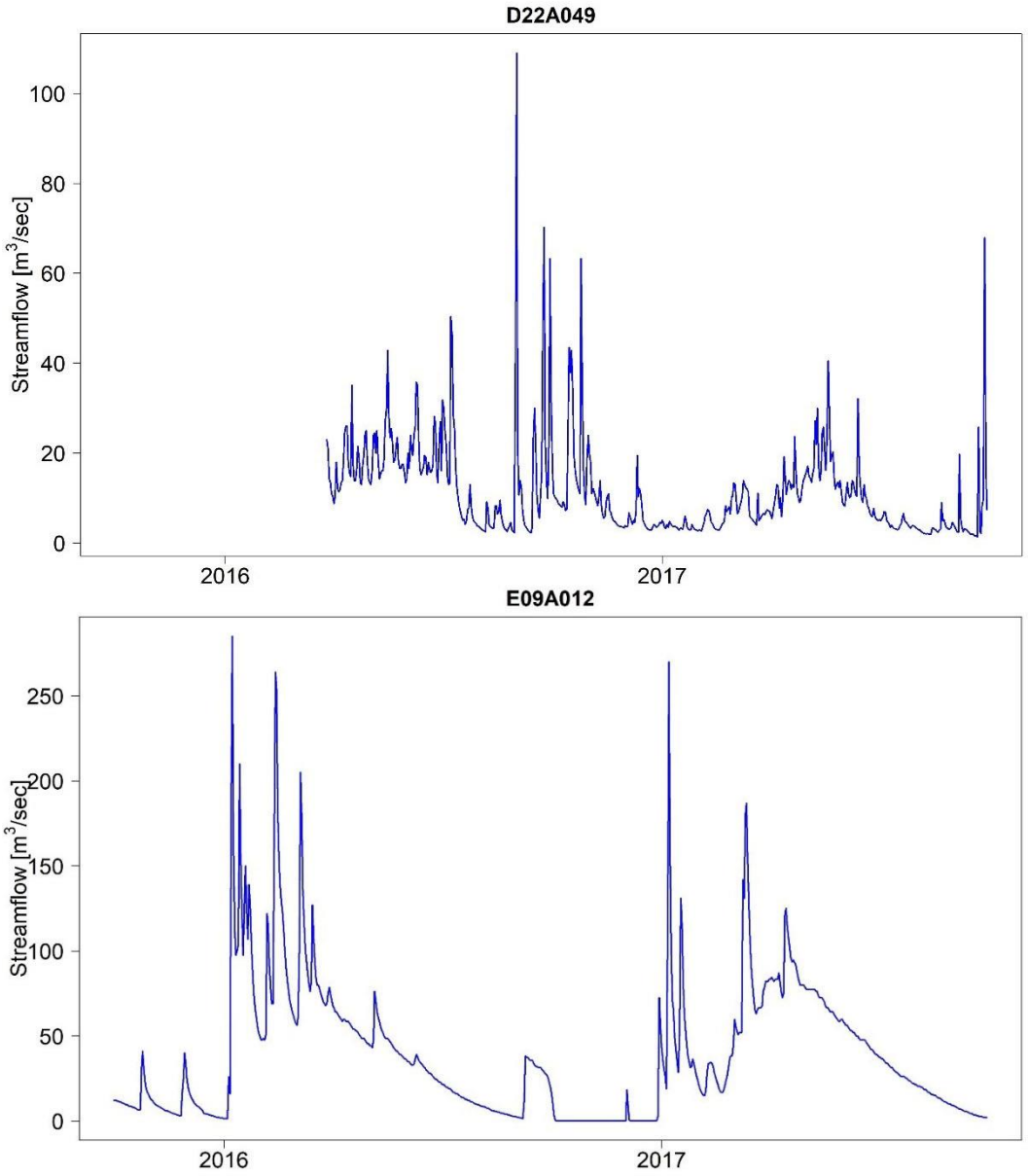

Figure 2.8. Time series of streamflow gauges used for the calibration study. D22A049: Calibration basin of EBS, E09A012: Calibration basin of MED.

2.4.2.2 WRF-Hydro-SA calibration period

The WRF-Hydro-SA model parameters are calibrated throughout one year (i.e., between 01.04.2016 - 01.04.2017 for EBS and 01.01.2016 - 01.01.2017 for MED).

Seven different parameters, which are the most calibrated in the literature and thought to have a significant effect on the streamflow output, are selected to calibrate in this study (Yucel et al., 2015; Senatore et al., 2015; Givati et al., 2016; Naabil et al., 2017; Kerandi et al., 2018; Fersch et al., 2020; Zhang et al., 2020b; Camera et al., 2020; Abbaszadeh et al., 2020; Kilicarslan et al., 2021):

- REFKDT: Infiltration depth
- RETDEPRTFAC: Retention depth scaling factor
- REFDK: the reference (silty clay loam) saturated hydraulic conductivity
- SLOPE: Free drainage coefficient
- OVROUGHRTFAC: Overland roughness scaling factor
- MAnnN: Manning's roughness coefficient
- LKSATFAC: Lateral saturated hydraulic conductivity scaling factor

In the calibration part, ten different values are tested for each parameter. Before starting the calibration process, a sensitivity analysis is applied to the hydrologic model during the relatively short spin-up period. As a result of this analysis, the model's sensitivity to the RETDEPRTFAC parameter is low, and the model gives the best streamflow outputs for the both region when this parameter value is selected as 0. Based on this result, the best parameter value of RETDEPRTFAC is assumed as 0, and this parameter is excluded from the calibration study.

The WRF-Hydro-SA model is calibrated for four different cases:

- **EBS-daily**: Calibration of Arhavi subbasin in EBS considering daily streamflow data (based on KGE coefficient)
- **EBS-hourly:** Calibration of Arhavi subbasin in EBS considering hourly streamflow data (based on KGE coefficient)
- **MED-KGE:** Calibration of Oymapınar subbasin in MED considering daily streamflow data (based on KGE coefficient)
- **MED-NSE:** Calibration of Oymapınar subbasin in MED considering daily streamflow data (based on NSE coefficient)

The calibration process is carried out starting from the MED-KGE scenario. During the calibration of this scenario, it is observed that any value selected for the REFDK parameter other than the default value causes unreasonable streamflow outputs. In addition, Camera et al. (2020) stated that calibrating one of the REFDK and REFKDT parameters would be sufficient since these parameters are equifinal (i.e. Both parameters have the same effect on the WRF-Hydro-SA outputs). Thus, the REFDK parameter is not calibrated for the other scenarios, and the default value (i.e., $2x10^{-6}$) is assigned to this parameter.

The calibration is done based on the KGE coefficient for the first three cases, whereas the NSE coefficient is the decision statistic for the last case. The primary purpose is to compare the calibrated parameter values obtained for the same region and period but based on different coefficients. Besides, the WRF-Hydro-SA model is calibrated via the manual step-wise calibration method, as in Yucel et al. (2015). The manual calibration method first calibrates the parameters determining the total water volume (i.e., REFKDT, REFDK, SLOPE) and then the parameters specifying the hydrograph shape (i.e., OVROUGHRTFAC, MAnnN, LKSATFAC). While calibrating the first parameter (i.e., REFKDT), the model is run with the default values of the other parameters. For the following parameters, the model is initiated with the values of the parameters calibrated until then.

The WRF-Hydro-SA model is forced with the meteorological data (i.e., shortwave/longwave radiation, specific humidity, wind (u-v), temperature, surface pressure) generated by the WRF-SA model. However, in-situ measurements are utilized as precipitation forcing data instead of WRF-SA output for the calibration of the hydrologic model. The precipitation data of 181 stations in and around EBS and 99 stations in and around MED are provided by MGM. These point data are converted into gridded precipitation via the Inverse Distance Weighting (IDW) method since the WRF-Hydro model needs gridded inputs. The meteorological stations located inside the basins (shown in Figure 2.5) are used to evaluate the

precipitation and temperature outputs of the WRF-SA, WRF-Coup, and WRF-SM-Coup models.

2.4.2.3 WRF-Hydro-SA validation period

The WRF-Hydro-SA model is forced along the validation period with the calibrated parameters using four different precipitation input data sources:

- In-situ measurement
- WRF-SA
- Uncorrected radar
- Corrected radar

In this way, it is possible to measure the streamflow generation performance of the WRF-Hydro model with respect to different precipitation input products as well as different spatiotemporal conditions.

Uncorrected and corrected radar data (Yousefi, 2020) are used in this study. The spatial resolution of the radar data is 1 km. However, the meteorological variables to be given as input data to the WRF-Hydro-SA model have a spatial resolution of 3 km. Furthermore, the complex topography of the study areas causes the beam blockage in radar sensors, and correspondingly, this condition prevents the acquisition of spatially continuous radar data over the regions. Due to the beam blockage, 55% of the Eastern Black Sea region and 38% of the Mediterranean region do not have radar data (Figure 2.5-A and Figure 2.5-C). Hence, the radar data with 1 km spatial resolution are interpolated into 3 km grids, and the grids that do not incorporate radar data are filled with the in-situ measurements before being used as forcing for the WRF-Hydro-SA model. Fundamentally, four different methods have been tried:

- **Method 1:** In-situ measurements are interpolated to the domain with the grids having 3 km horizontal grid spacing via the IDW method. 1 km radar data are upscaled to the 3 km grid resolution using the bilinear interpolation

method. The empty grids in the 3-km radar data are filled with the observation data.

- **Method 2:** In-situ measurements are interpolated to the domain with the grids having 1 km horizontal grid spacing via the IDW method. The empty grids in the 1-km radar data are filled with the observation data. The filled data at 1 km are upscaled to the 3 km grid resolution using the bilinear interpolation method.
- **Method 3:** In-situ measurements are interpolated to the domain with the grids having 3 km horizontal grid spacing via the IDW method. 1 km radar data are upscaled to the 3 km grid resolution using the weighted average method. The empty grids in the 3-km radar data are filled with the observation data.
- **Method 4:** In-situ measurements are interpolated to the domain with the grids having 1 km horizontal grid spacing via the IDW method. The empty grids in the 1 km radar data are filled with the observation data. The filled data at 1-km are upscaled to the 3 km grid resolution using the weighted average method.

A sensitivity analysis is conducted to understand which of these four different ways is more robust to generate radar data that will force the WRF-Hydro-SA model. The WRF-Hydro-SA model is separately run for a week using the radar data obtained from each method. The radar product, which produces the most accurate streamflow data at the end of these 1-week simulations, is also preferred to produce the radar data to be used as precipitation input for the validation analyses. As a result of this sensitivity analysis, the radar product obtained via the Method 2 is chosen as the radar data to be used in the validation period (Table 2.6). Also, the time series for each streamflow product obtained at the end of this sensitivity analysis and the spatial distribution of the precipitation at peak hour are presented in Figure 2.9 and Figure 2.10, respectively.

Table 2.6 Statistics calculated between the hourly streamflow outputs of the WRF-Hydro-SA model and the closest stream gauge data for the flood event in Kemer between 13.12.2018 - 20.12.2018. The WRF-Hydro-SA model is separately simulated, considering each radar product obtained from different methods. RMSE: root means square error, NSE: Nash Sutcliffe Efficiency, R: Correlation. The unit of the streamflow data is m^3/s.

	RMSE	NSE	R
Method 1	72.73	0.18	0.72
Method 2	64.31	0.34	0.77
Method 3	66.80	0.29	0.75
Method 4	66.81	0.29	0.75

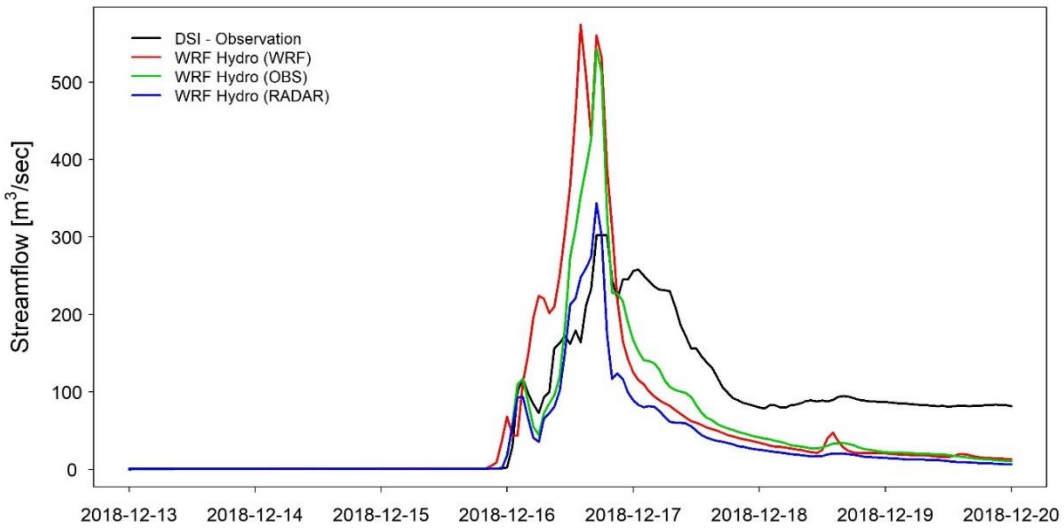

Figure 2.9. The observed streamflow data from station D08A071 and WRF-Hydro-SA model outputs for the Kemer – Ovacık event simulations. WRF Hydro (WRF): The output when the WRF Hydro-SA model is forced with WRF precipitation, WRF Hydro (OBS): The output when the WRF Hydro-SA model is forced with precipitation from in-situ measurement, WRF Hydro (RADAR): The output when the WRF Hydro-SA model is forced with the radar precipitation obtained from method 2.

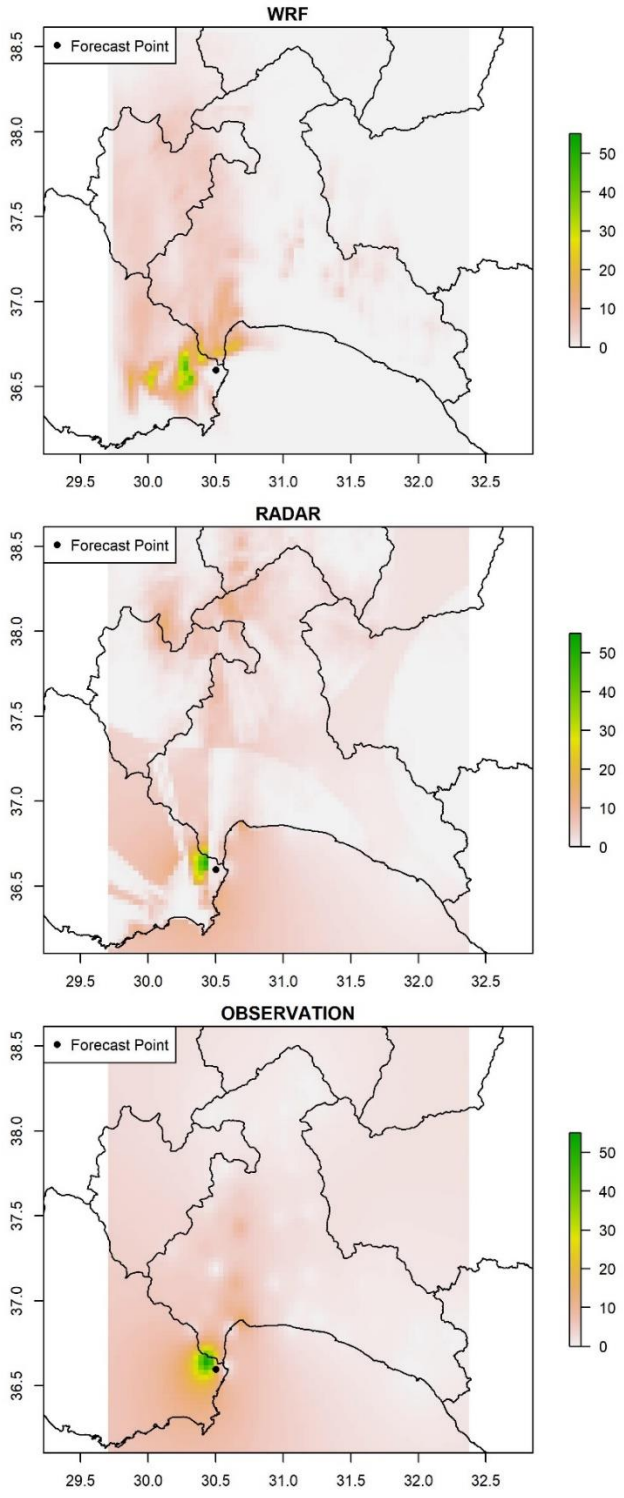

Figure 2.10. Spatial distribution of precipitation (in mm) by products for the peak hour of the Kemer event (for the output obtained with Method 2).

2.4.3 WRF-Coup

Input data source, model physics, and spatial resolution of the atmospheric model of the WRF-Coup model are the same as the WRF-SA described in Section 2.4.1, and the characteristics of the hydrological model of the WRF-Coup are the same as the calibrated WRF-Hydro-SA model mentioned in Section 2.4.2. The WRF-Hydro model in the coupled model is run with the calibrated parameters obtained from the MED-KGE and EBS-daily calibration scenarios for the MED and EBS regions, respectively.

2.4.4 WRF-SM-Coup

The coupled WRF & WRF-Hydro modeling system is initiated with the topsoil layer moisture data from the SMAP product to obtain the WRF-Coup-SA model. The SMAP product has a temporal resolution of 3-hour and a spatial resolution of 9 km. The GFS keeps providing the other boundary conditions of this model. The SMAP product is not raw satellite data; the National Aeronautics and Space Administration (NASA) downscales the SMAP satellite outputs (36 km) to form such high-resolution data.

The soil moisture data from different sources (i.e., satellite, model, in-situ measurement) have different scales (i.e., data distribution/dispersion); therefore, the corresponding data are rescaled before being used in the same analyses (Dirmeyer et al., 2004; Reichle and Koster, 2005; Afshar and Yilmaz, 2017). Accordingly, the SMAP product is rescaled to the scale of GFS soil moisture because the GFS source supplies all the other boundary data. Albeit the study covers two years, the rescaling processes are conducted between 2015-10-01 and 2019-10-01 since using a more extended period improves the rescaling success (Yilmaz and Crow, 2013). The rescaling process is achieved using three different methods; two of which are linear (linear regression (REG) and variance matching (VAR)), and one is nonlinear (multivariate adaptive regression splines (MARS)). Method performances are

compared in terms of Bias, correlation, root-mean-square-error (RMSE), and standard deviation ratio (SD ratio) statistics.

Linear rescaling is performed using the following equations based on the existence of a simple linear relationship between SMAP and GFS soil moisture (Yilmaz and Crow, 2013).

$$Y^{*}_{REG} = \mu_x + (Y - \mu_y) x c^{REG} \quad (1)$$

$$Y^{*}_{VAR} = \mu_x + (Y - \mu_y) x c^{VAR} \quad (2)$$

$$c^{REG} = \frac{\sigma x}{\sigma y} \rho(x, y) \quad (3)$$

$$c^{VAR} = \frac{\sigma x}{\sigma y} \quad (4)$$

where;

Y= SMAP time series

Y^{*}_{REG} = SMAP data obtained via REG method

Y^{*}_{VAR} = SMAP data obtained via VAR method

μ_x = Mean of the GFS time series

μ_y = Mean of the SMAP time series

$\boldsymbol{\rho}(x,y)$ = Correlation between GFS and SMAP time series

σ_x = Standard deviation of the GFS time series

σ_y = Standard deviation of the SMAP time series

Although MARS is a linear model in terms of its algorithm, it examines the nonlinear relationships that might exist between input and output variables (Friedman, 1991). The model consists of two steps: i) forward stepwise phase ii) backward stepwise phase. In the forward stepwise phase, the model aims to minimize the errors between the output and target (i.e., rescaled and reference data set for our case) variables. It is the backward stepwise phase that prunes the function to avoid overfitting and allows the model to converge to the real function rather than the existing data.

SMAP data are used as input data for the rescaling methods to estimate the GFS data. The statistics are calculated between the estimated GFS and the actual GFS products over each SMAP grid in d01 domain and the closest GFS grid. The MARS method gives the best value for all the statistics except the SD ratio, in which the VAR method is the best. The VAR method inherently equates the standard deviation of the rescaled data to the standard deviation of the reference data. Nevertheless, the method excessively focuses on matching the standard deviation and causes relatively low values at other statistics and highly fluctuated outputs (Figure 2.11-A, and Figure 2.11-B). Therefore, the WRF-SM-Coup model is initiated using SMAP data rescaled with the MARS method. Moreover, the spatial distribution of the SMAP (i.e., before the rescaling), GFS, and SMAP (MARS) data at the initiation time of the models (i.e., 2015-10-01-00:00:00) are shown under the corresponding columns in Figure 2.11-C and Figure 2.11-D. According to these figures, SMAP soil moistures are consistently smaller than the GFS values for both regions, which could be due to a scaling difference between the products; hence the satellite soil moisture data should be rescaled before their use in models.

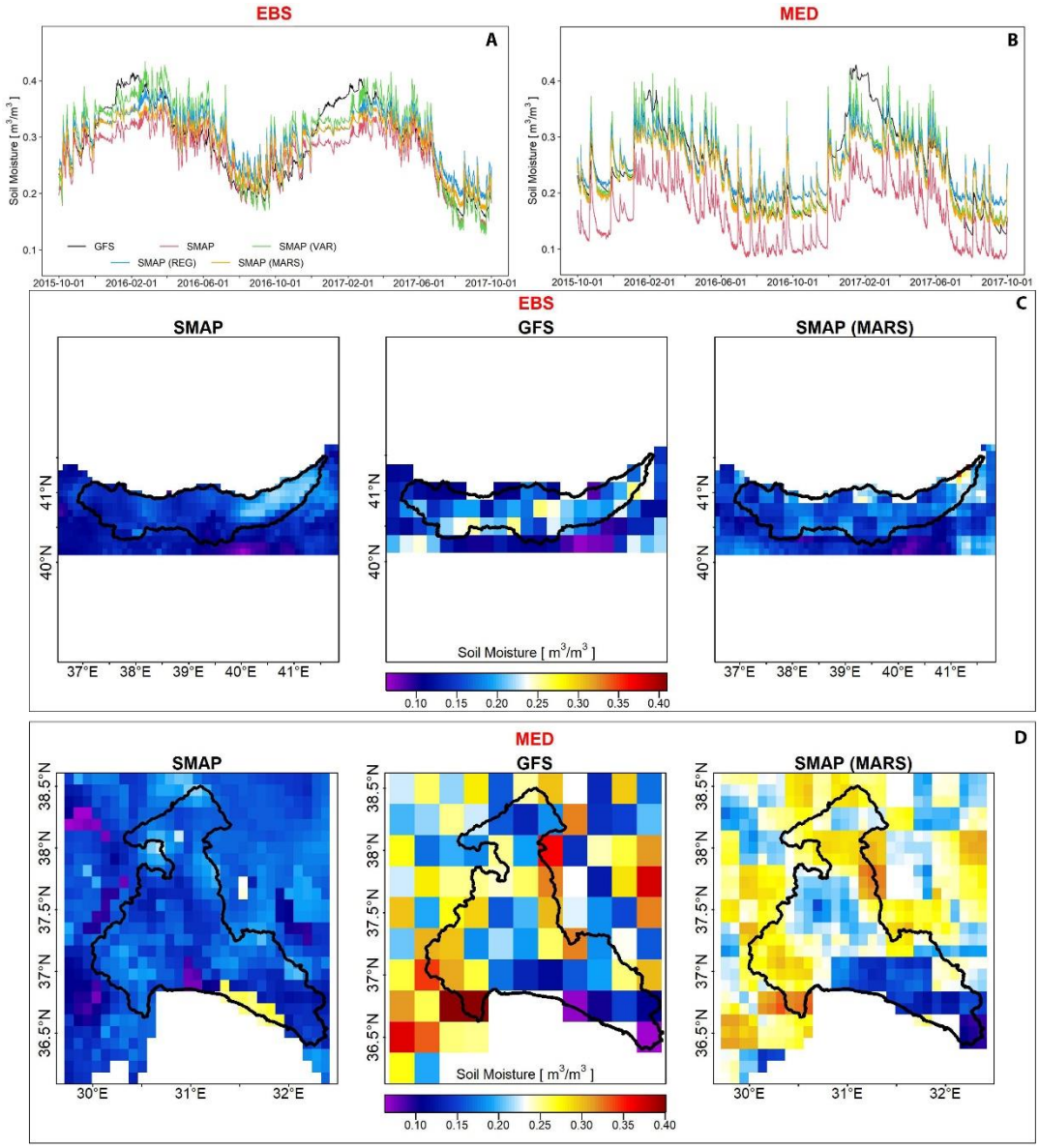

Figure 2.11. Time series of the topsoil layer moisture of different products for the study period (Panel A and B). Panel C and D shows the spatial distribution of the topsoil layer moisture products by regions for the initiation time of the long-term WRF model simulations (i.e., 10.01.2015-00:00:00). The figure is obtained using R-programming language (R Core Team, 2020).

CHAPTER 3

RESULTS AND DISCUSSION

3.1 Sensitivity of the extreme precipitation simulation capability of the WRF model against model physics and initial and lateral boundary data source

3.1.1 Temporal characteristics of area-averaged precipitation

In this section, the ensembles, which are composed of 24 members, are formed concerning the initial and lateral boundary condition & horizontal grid spacing combinations. Here, the primary motivation is to discuss the differences in the WRF outcomes associated with the changing external parameters (i.e., initial and lateral boundary data source and spatial resolution) rather than the model physics. Evaluations are performed based on the information between the ensemble mean value of the members and observed areal mean precipitation for the regions.

Figure 3.1 shows the mean time series for the simulation period of the events. Each column in the figure indicates the scenarios that correspond to the different initial and lateral boundary conditions & horizontal grid spacing combination, whereas each row exhibits an event. The variations in the observed areal mean precipitation, each of WRF ensemble members, and ensemble mean of the members can be observed from the figure. Fundamentally, Figure 3.1 shows that the model members underestimate the precipitation amount except for the MED-autumn and some members of the EBS-summer events. Particularly for the MED-autumn event, all members overestimate the peak value. Though WRF does not correctly predict the amount of the peak values, it is generally successful at capturing the peak hours of the extreme events. Notably, a considerable part of the model configurations that include GFS can accurately detect even the peak hour of the MED-summer, which

is a highly intense and short-term event. Approximately 35% of the members involving GFS determines the peak hour of this event. The ratio of those members missing the peak hour more than one hour is 18.75%. According to the correlation values between the ensemble means and the area-averaged precipitation, the general fluctuations of the WRF ensembles during the 73 hours agree well with the observations. For the EBS-autumn event, the correlations are around 0.90. The correlation is higher at summer events when GFS is used as the initial and lateral boundary conditions. ERA5 ensembles give a better correlation only for the MED-autumn event. Furthermore, based on areal mean precipitation, the cases having 3 km horizontal grid spacing are as successful as 9 km in terms of the correlation coefficient.

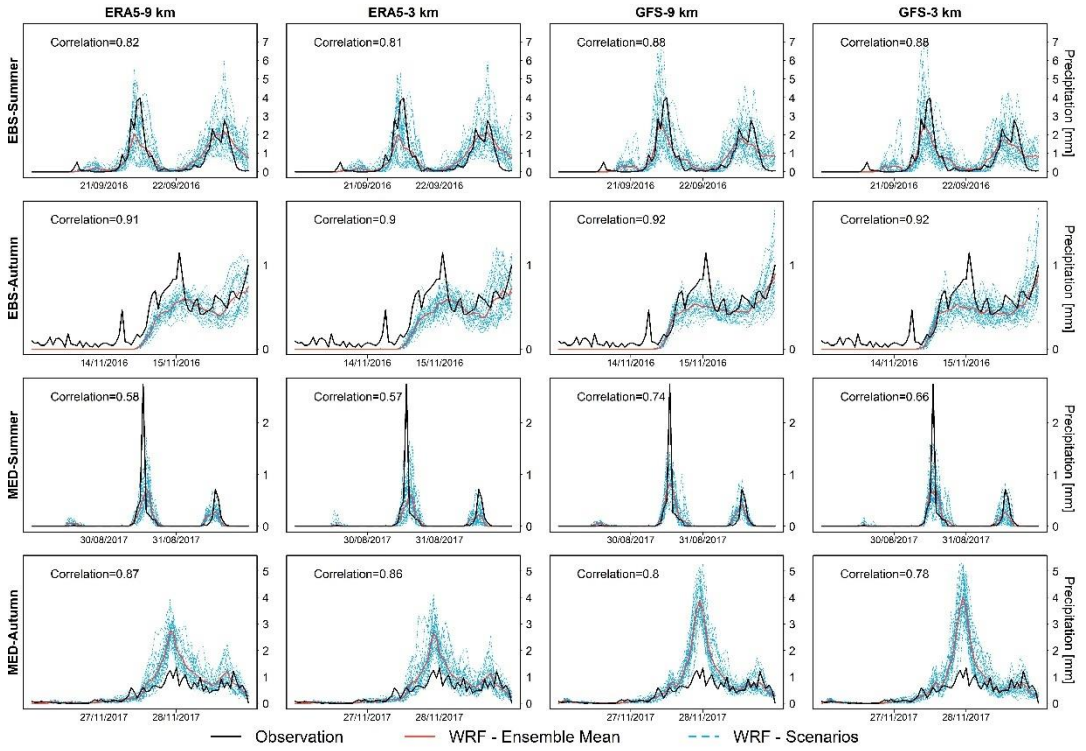

Figure 3.1. The area-averaged observed and WRF-derived precipitation considering different initial and lateral boundary condition & horizontal grid spacing combinations. For each case, the correlation values are calculated between the ensemble mean of the corresponding 24 scenarios and the observed data.

In Figure 3.2, dispersions of the hourly areal mean precipitation data for the event day (i.e., 24 data points) are presented for the gauge records, as well as for the different initial and lateral boundary conditions & horizontal grid spacing configurations. The observations are shown in green, and each scenario is marked with a color, changing from red to blue. The member colored with red has the lowest TOPSIS coefficient among the 24 members, and the blue one indicates the member with the highest coefficient. The other colors between these two show the order of each member. For the illustration of Figure 3.2, TOPSIS coefficients are obtained based on the metrics calculated between the hourly areal mean values of the observations and each member. In this way, the capacity of the model in capturing area-averaged hourly precipitation for the entire region is displayed. Firstly, the limits of the interquartile range and the maximum point for the observation of the EBS-summer are well presented by the best members of each of ERA5 and GFS ensembles. However, the skill for demonstrating the interquartile range and the maximum point is highly variable between the scenarios. Thus, the physics choices are quite influential on the variability of the simulations performed for this event. Secondly, most of the ERA5 configurations shown with bluish colors provide almost the same median value as the EBS-autumn observation. In other words, these configurations are successful at predicting the average precipitation amount for the event day. Nevertheless, all combinations simulating EBS-autumn underestimate the peak value of the event. Figure 3.2 also shows that, compared to the other events, the observed data of the EBS-autumn has a more symmetrical distribution shape. So, the total precipitation amount is more uniformly distributed along the simulation period than the other events. The scenarios generally have difficulty in following this symmetrical shape owing to the underestimation of the peak value. Moreover, the MED-summer event's distribution shape dramatically has positive skewness since the event occurs just in a few hours. Albeit the scenarios are successful at matching the distribution shape, they are not capable of determining the maximum value. Lastly, the overestimation of the MED-autumn event in terms of the peak value and the size of the interquartile range is also presented by the boxplots of scenarios. The

overestimation is more explicit in GFS-forced members than those in ERA5-forced members.

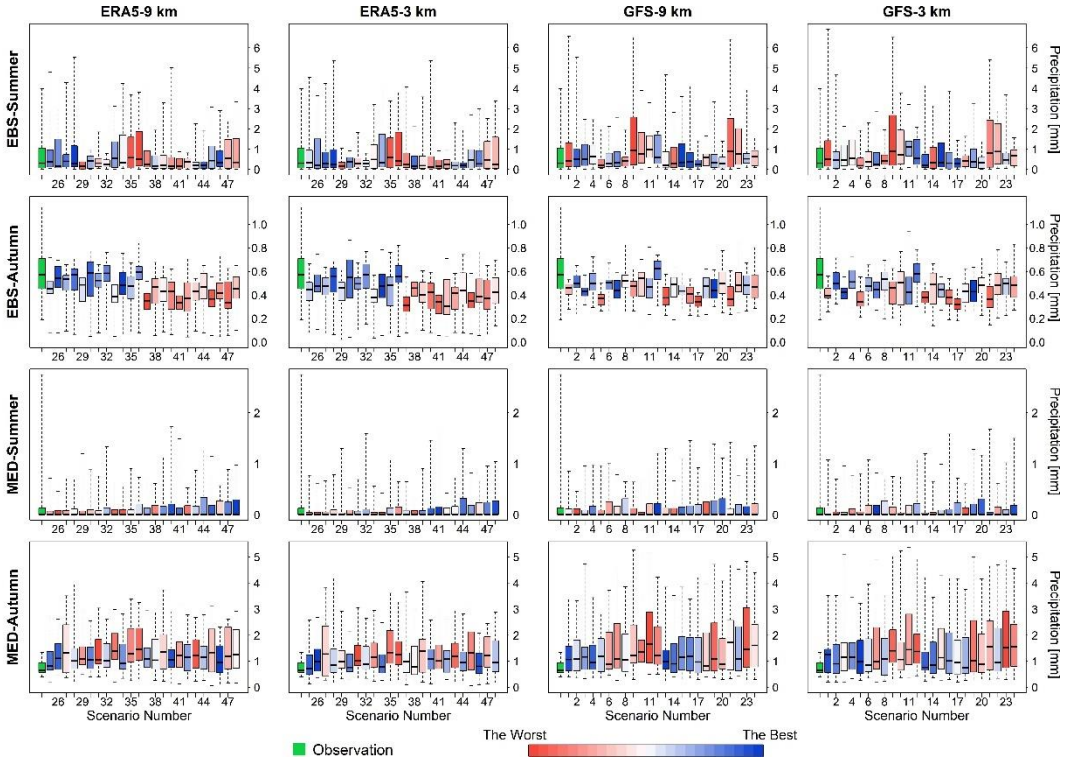

Figure 3.2. The comparison of the dispersions of the observed precipitation and the individual WRF scenarios for the event day. Colors of the boxes indicate the hierarchy between the scenarios based on TOPSIS algorithm. The rating is performed for each initial and lateral boundary condition & horizontal grid spacing combination, separately. Scenario numbers are assigned based on Table 2.3.

Figure 3.3 compares the influences of the initial and lateral boundary data source and parameterization choices on the variability of the WRF outputs for the 9 km spatial resolution. The blue line in the figure is obtained by calculating the variance of the area-averaged precipitation values from the 24 members of ERA5 forcing for each hour. This line shows the effect of the parameterization on the variability when ERA5 is chosen as the initial and lateral boundary data source. Similarly, the orange line indicates the effect of the parameterization, in case meteorological data of the GFS is used to initiate the model. The purple line shows the initial and lateral

boundary data effect. As seen in Table 2.3, each of the 24 parameterization combinations forms two different scenarios, one with ERA5 and one with GFS. A new precipitation time series is attained for the grids of each combination by taking the mean of the precipitation outputs coming from these two scenarios (e.g., 1-25, 2-26, 3-27, …, 24-48 in Table 2.3). The variance of the area-averaged precipitations of the newly obtained 24 scenarios for each hour is assumed to present the initial and lateral boundary data effect on the area-averaged precipitation variability generated by WRF. In general, when the initial and lateral boundary data source is chosen as GFS, the parameterization effect is higher in comparison to ERA5 except for the MED-summer. Still, there are some hours, at which the parameterization effect is relatively higher for the ERA5 choices. Figure 3.3 additionally proves that the parameterization choices affect the area-averaged precipitation variability more than the initial and lateral boundary data source selection for the simulated events.

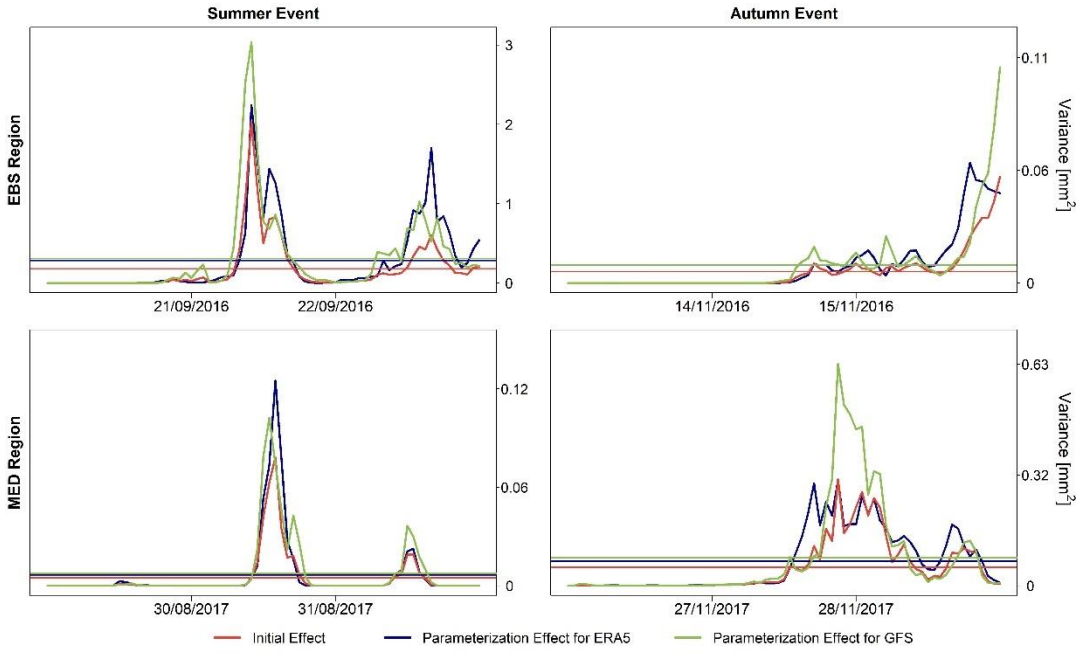

Figure 3.3. The influences of the initial and lateral boundary data source and parameterization on WRF-derived precipitation. The horizontal lines show the mean values of the plots represented with the same color.

3.1.2 Selection of the best scenarios

The ensemble approach is quite useful for the sensitivity analyses since the error of the predictions originates from the model configurations (Houtekamer et al., 1996). One of the primary objectives of this section is to choose the best WRF-model configurations from the constituted scenarios that are composed of parameterization schemes, initial and lateral boundary data, and spatial resolutions for each event. Table 3.1 and Table 3.2 show the hierarchy between the scenarios considering the TOPSIS algorithm for each event and spatial resolution, separately (i.e., Table 3.1 for 9 km and Table 3.2 for 3 km spatial resolutions). In Table 3.2, the CU parameterization of 3 km scenarios is colored with red because it is kept inactive in simulations. Those show the CU scheme of the collaborating coarse domain. To begin with, the best scenarios of the EBS-summer case for both 9 km and 3 km grid spacing commonly include MYJ and ERA5 combinations. PBL scheme of the best scenarios is changeable for the other events. Nevertheless, ERA5 is dominant for the EBS-Autumn as well, at which 8 of the best 10 scenarios (i.e., best five scenarios per resolution, a total of 10 scenarios) use ERA5 as initial and lateral boundary conditions. Thus, it can be asserted that ERA5 is superior compared to GFS over the EBS region. On the contrary, given the MED-summer event, GFS is better than ERA5. Both data sources are credible for the MED-autumn event. Besides, WSM6 is the driving MP scheme of the EBS-autumn. Whereas, ES is the MP scheme of all the best scenarios of the MED-autumn. The driving MP scheme is generally variable in summer except for the small domain of the MED-summer. AATS governs the best scenarios for the 3 km domain of the MED-summer. The choice of the MP scheme is determinant for the EBS-summer event because the other parameters of the best scenarios are stable. In terms of the CU scheme, rather than autumn, BMJ is more efficient in summer. Unlike, KF is more influential in autumn. It is encountered with the GFES scheme in the best scenarios of both autumn and summer events.

Table 3.1 List of the scenarios ordered from the best to the worst, based on the TOPSIS results for the 9 km spatial resolution.

	EBS-Summer				EBS-Autumn				MED-Summer				MED-Autumn			
	MP	CU	PBL	Initial	MP	CU	PBL	Initial	MP	CU	PBL	Initial	MP	CU	PBL	Initial
1	ATS	BMJ	MYJ	ERA5	WSM6	KF	MYJ	ERA5	ES	BMJ	YSU	ERA5	ES	KF	MYJ	GFS
2	ES	GFES	MYJ	ERA5	WSM6	GFES	YSU	ERA5	KS	BMJ	YSU	GFS	ES	GFES	YSU	ERA5
3	WSM6	BMJ	MYJ	ERA5	WSM6	GFES	YSU	GFS	ATS	BMJ	MYJ	ERA5	ES	GFES	MYJ	GFS
4	KS	BMJ	MYJ	ERA5	WSM6	GFES	MYJ	ERA5	WSM6	GFES	MYJ	GFS	ES	KF	YSU	GFS
5	ATS	GFES	MYJ	ERA5	ATS	KF	MYJ	ERA5	ATS	GFES	MYJ	ERA5	ES	GFES	MYJ	ERA5
6	WSM6	GFES	MYJ	ERA5	WSM6	GFES	MYJ	GFS	KS	KF	YSU	GFS	ATS	GFES	MYJ	GFS
7	ATS	GFES	YSU	ERA5	KS	KF	YSU	ERA5	KS	KF	MYJ	GFS	ES	GFES	YSU	GFS
8	KS	GFES	MYJ	GFS	ES	GFES	YSU	GFS	ES	GFES	MYJ	GFS	ES	BMJ	MYJ	GFS
9	WSM6	GFES	YSU	ERA5	ATS	GFES	YSU	ERA5	KS	BMJ	MYJ	GFS	ATS	GFES	YSU	GFS
10	ES	KF	MYJ	GFS	ES	KF	MYJ	ERA5	ATS	BMJ	MYJ	GFS	WSM6	GFES	MYJ	ERA5
11	ATS	KF	MYJ	ERA5	WSM6	KF	YSU	ERA5	ATS	BMJ	YSU	GFS	ES	BMJ	YSU	GFS
12	ES	KF	MYJ	ERA5	ATS	KF	YSU	ERA5	ATS	KF	MYJ	GFS	ES	BMJ	MYJ	ERA5
13	WSM6	KF	MYJ	ERA5	KS	BMJ	MYJ	GFS	KS	GFES	YSU	GFS	WSM6	KF	YSU	GFS
14	ES	BMJ	MYJ	ERA5	ES	KF	YSU	ERA5	WSM6	KF	YSU	ERA5	ATS	BMJ	MYJ	GFS
15	ES	BMJ	YSU	ERA5	ATS	KF	YSU	GFS	WSM6	BMJ	MYJ	GFS	ATS	GFES	MYJ	ERA5
16	ES	GFES	YSU	ERA5	WSM6	BMJ	YSU	ERA5	ATS	GFES	MYJ	GFS	ES	BMJ	YSU	ERA5
17	ES	GFES	MYJ	GFS	ES	GFES	YSU	ERA5	KS	GFES	MYJ	GFS	ATS	BMJ	YSU	GFS
18	WSM6	BMJ	YSU	ERA5	KS	GFES	YSU	ERA5	ATS	KF	YSU	GFS	WSM6	KF	MYJ	GFS
19	ES	KF	YSU	ERA5	WSM6	KF	MYJ	GFS	ATS	KF	YSU	ERA5	ATS	KF	MYJ	GFS
20	ATS	BMJ	YSU	ERA5	ATS	BMJ	MYJ	GFS	WSM6	BMJ	YSU	GFS	WSM6	GFES	YSU	ERA5
21	ATS	KF	MYJ	GFS	ES	GFES	MYJ	ERA5	WSM6	BMJ	YSU	ERA5	ATS	KF	YSU	GFS
22	ES	GFES	YSU	GFS	ATS	KF	MYJ	GFS	ATS	BMJ	YSU	ERA5	WSM6	GFES	MYJ	GFS
23	KS	GFES	YSU	ERA5	KS	KF	MYJ	ERA5	WSM6	KF	MYJ	ERA5	WSM6	GFES	YSU	GFS
24	KS	KF	MYJ	ERA5	ATS	BMJ	YSU	GFS	WSM6	GFES	MYJ	ERA5	ATS	BMJ	YSU	ERA5
25	KS	GFES	MYJ	ERA5	ES	KF	MYJ	GFS	ES	GFES	MYJ	ERA5	WSM6	BMJ	YSU	GFS
26	WSM6	BMJ	MYJ	GFS	ATS	BMJ	YSU	ERA5	KS	GFES	MYJ	ERA5	WSM6	BMJ	MYJ	GFS
27	ATS	KF	YSU	ERA5	KS	GFES	MYJ	GFS	ES	KF	YSU	ERA5	ES	KF	YSU	ERA5
28	KS	BMJ	YSU	GFS	ES	BMJ	YSU	GFS	WSM6	KF	YSU	GFS	ATS	BMJ	MYJ	ERA5
29	KS	BMJ	YSU	ERA5	WSM6	KF	YSU	GFS	WSM6	BMJ	MYJ	ERA5	KS	GFES	YSU	GFS
30	KS	KF	YSU	ERA5	WSM6	BMJ	MYJ	ERA5	ATS	GFES	YSU	GFS	WSM6	BMJ	MYJ	ERA5
31	ES	KF	YSU	GFS	ES	BMJ	YSU	ERA5	KS	KF	YSU	ERA5	ATS	GFES	YSU	ERA5
32	ATS	KF	YSU	GFS	ATS	GFES	MYJ	ERA5	ATS	GFES	YSU	ERA5	ES	KF	MYJ	ERA5
33	ATS	GFES	YSU	GFS	KS	GFES	YSU	GFS	ES	KF	MYJ	GFS	KS	GFES	MYJ	GFS
34	KS	GFES	YSU	GFS	ES	BMJ	MYJ	GFS	ES	GFES	YSU	ERA5	KS	BMJ	YSU	GFS
35	KS	BMJ	MYJ	GFS	ATS	BMJ	MYJ	ERA5	ES	KF	YSU	GFS	WSM6	BMJ	YSU	ERA5
36	KS	KF	MYJ	GFS	KS	BMJ	YSU	ERA5	ATS	KF	MYJ	ERA5	KS	BMJ	MYJ	GFS
37	ATS	BMJ	YSU	GFS	ES	KF	YSU	GFS	WSM6	KF	MYJ	GFS	KS	KF	YSU	GFS
38	WSM6	GFES	MYJ	GFS	WSM6	BMJ	YSU	GFS	WSM6	GFES	YSU	GFS	ATS	KF	MYJ	ERA5
39	ATS	GFES	MYJ	GFS	ATS	GFES	MYJ	GFS	ES	BMJ	YSU	GFS	KS	KF	MYJ	GFS
40	WSM6	KF	MYJ	GFS	KS	KF	MYJ	GFS	WSM6	GFES	YSU	ERA5	KS	KF	MYJ	ERA5
41	KS	KF	YSU	GFS	WSM6	BMJ	MYJ	GFS	ES	BMJ	MYJ	ERA5	KS	GFES	MYJ	ERA5
42	WSM6	BMJ	YSU	GFS	ATS	GFES	YSU	GFS	ES	GFES	YSU	GFS	KS	BMJ	MYJ	ERA5
43	WSM6	KF	YSU	ERA5	KS	BMJ	YSU	GFS	KS	GFES	YSU	ERA5	KS	BMJ	YSU	ERA5
44	WSM6	GFES	YSU	GFS	KS	GFES	MYJ	ERA5	ES	KF	MYJ	ERA5	ATS	KF	YSU	ERA5
45	WSM6	KF	YSU	GFS	KS	KF	YSU	GFS	KS	BMJ	YSU	ERA5	WSM6	KF	MYJ	ERA5
46	ES	BMJ	YSU	GFS	KS	BMJ	MYJ	ERA5	KS	BMJ	MYJ	ERA5	KS	KF	YSU	ERA5
47	ES	BMJ	MYJ	GFS	ES	BMJ	MYJ	ERA5	KS	KF	MYJ	ERA5	WSM6	KF	YSU	ERA5
48	ATS	BMJ	MYJ	GFS	ES	GFES	MYJ	GFS	ES	BMJ	MYJ	GFS	KS	GFES	YSU	ERA5

Table 3.2 List of the scenarios ordered from the best to the worst, based on the TOPSIS results for the 3 km spatial resolution.

	EBS-Summer				EBS-Autumn				MED-Summer				MED-Autumn			
	MP	CU	PBL	Initial	MP	CU	PBL	Initial	MP	CU	PBL	Initial	MP	CU	PBL	Initial
1	ATS	BMJ	MYJ	ERA5	WSM6	KF	MYJ	ERA5	ATS	GFES	MYJ	GFS	ES	GFES	YSU	ERA5
2	ATS	GFES	MYJ	ERA5	WSM6	GFES	YSU	ERA5	ATS	GFES	MYJ	ERA5	ES	GFES	MYJ	GFS
3	WSM6	BMJ	MYJ	ERA5	ATS	KF	MYJ	ERA5	KS	GFES	MYJ	GFS	ES	KF	YSU	GFS
4	WSM6	GFES	MYJ	ERA5	ATS	BMJ	YSU	ERA5	ATS	KF	YSU	GFS	ES	GFES	MYJ	ERA5
5	ES	GFES	MYJ	ERA5	WSM6	GFES	YSU	GFS	ATS	GFES	YSU	GFS	ES	BMJ	YSU	GFS
6	ATS	GFES	YSU	ERA5	WSM6	GFES	MYJ	GFS	KS	KF	YSU	GFS	ES	GFES	YSU	GFS
7	KS	BMJ	MYJ	ERA5	ATS	BMJ	MYJ	GFS	WSM6	BMJ	YSU	GFS	ES	BMJ	MYJ	GFS
8	KS	GFES	MYJ	GFS	WSM6	KF	YSU	ERA5	KS	GFES	YSU	GFS	ES	KF	MYJ	GFS
9	WSM6	GFES	YSU	ERA5	ATS	GFES	MYJ	ERA5	ES	GFES	MYJ	GFS	ATS	GFES	MYJ	GFS
10	ES	BMJ	YSU	ERA5	WSM6	KF	MYJ	GFS	ATS	BMJ	MYJ	ERA5	ATS	GFES	YSU	GFS
11	WSM6	KF	MYJ	ERA5	KS	KF	YSU	ERA5	ATS	KF	MYJ	GFS	ATS	BMJ	MYJ	GFS
12	ES	BMJ	MYJ	ERA5	ATS	KF	MYJ	GFS	WSM6	GFES	MYJ	ERA5	ES	BMJ	YSU	ERA5
13	ES	KF	MYJ	ERA5	KS	KF	MYJ	ERA5	WSM6	BMJ	MYJ	GFS	WSM6	GFES	MYJ	ERA5
14	ES	GFES	YSU	ERA5	ES	GFES	YSU	GFS	ATS	KF	YSU	ERA5	ES	BMJ	MYJ	ERA5
15	WSM6	BMJ	YSU	ERA5	WSM6	GFES	MYJ	ERA5	ATS	GFES	YSU	ERA5	ATS	GFES	MYJ	ERA5
16	ES	KF	MYJ	GFS	ATS	GFES	YSU	ERA5	ATS	BMJ	MYJ	GFS	WSM6	KF	YSU	GFS
17	ATS	KF	MYJ	ERA5	KS	BMJ	MYJ	GFS	ES	GFES	MYJ	ERA5	ATS	BMJ	YSU	GFS
18	WSM6	BMJ	MYJ	GFS	ATS	BMJ	MYJ	ERA5	WSM6	GFES	YSU	GFS	WSM6	GFES	MYJ	GFS
19	ATS	BMJ	YSU	ERA5	ATS	KF	YSU	ERA5	ES	BMJ	YSU	ERA5	ATS	BMJ	MYJ	ERA5
20	ES	GFES	YSU	GFS	WSM6	BMJ	YSU	ERA5	ATS	BMJ	YSU	GFS	WSM6	GFES	YSU	ERA5
21	ATS	KF	YSU	ERA5	WSM6	BMJ	YSU	GFS	WSM6	GFES	MYJ	GFS	WSM6	GFES	YSU	GFS
22	ATS	KF	MYJ	GFS	WSM6	BMJ	MYJ	ERA5	WSM6	KF	YSU	ERA5	WSM6	BMJ	MYJ	GFS
23	ES	GFES	MYJ	GFS	WSM6	KF	YSU	GFS	KS	GFES	MYJ	ERA5	WSM6	BMJ	YSU	GFS
24	KS	KF	YSU	ERA5	KS	GFES	MYJ	GFS	KS	BMJ	YSU	GFS	ATS	KF	MYJ	GFS
25	KS	GFES	MYJ	ERA5	KS	GFES	YSU	GFS	ES	KF	MYJ	GFS	ATS	BMJ	YSU	ERA5
26	ATS	KF	YSU	GFS	ES	GFES	YSU	ERA5	WSM6	BMJ	MYJ	ERA5	ATS	KF	YSU	GFS
27	ES	KF	YSU	ERA5	ATS	BMJ	YSU	GFS	ES	BMJ	MYJ	ERA5	ES	KF	YSU	ERA5
28	ES	KF	YSU	GFS	ATS	KF	YSU	GFS	ES	BMJ	YSU	GFS	WSM6	KF	MYJ	GFS
29	KS	GFES	YSU	ERA5	KS	GFES	YSU	ERA5	WSM6	KF	MYJ	GFS	KS	GFES	YSU	GFS
30	KS	KF	MYJ	ERA5	ES	KF	YSU	ERA5	KS	BMJ	MYJ	GFS	WSM6	BMJ	MYJ	ERA5
31	KS	BMJ	YSU	ERA5	ATS	GFES	YSU	GFS	KS	KF	MYJ	GFS	ATS	GFES	YSU	ERA5
32	ATS	GFES	YSU	GFS	KS	BMJ	MYJ	ERA5	ES	GFES	YSU	ERA5	WSM6	BMJ	YSU	ERA5
33	KS	BMJ	YSU	GFS	ES	GFES	MYJ	GFS	ES	GFES	YSU	GFS	KS	GFES	MYJ	GFS
34	KS	BMJ	MYJ	GFS	WSM6	BMJ	MYJ	GFS	WSM6	BMJ	YSU	ERA5	ES	KF	MYJ	ERA5
35	KS	GFES	YSU	GFS	KS	BMJ	YSU	ERA5	WSM6	KF	MYJ	ERA5	KS	BMJ	MYJ	GFS
36	WSM6	GFES	MYJ	GFS	ES	KF	YSU	GFS	KS	KF	YSU	ERA5	KS	BMJ	YSU	GFS
37	ATS	GFES	MYJ	GFS	ATS	GFES	MYJ	GFS	WSM6	KF	YSU	GFS	KS	BMJ	MYJ	ERA5
38	WSM6	KF	MYJ	GFS	KS	KF	YSU	GFS	WSM6	GFES	YSU	ERA5	KS	KF	YSU	GFS
39	ATS	BMJ	YSU	GFS	KS	KF	MYJ	GFS	ATS	KF	MYJ	ERA5	KS	KF	MYJ	ERA5
40	KS	KF	MYJ	GFS	KS	GFES	MYJ	ERA5	ES	KF	MYJ	ERA5	ATS	KF	MYJ	ERA5
41	WSM6	BMJ	YSU	GFS	KS	BMJ	YSU	GFS	ATS	BMJ	YSU	ERA5	KS	GFES	MYJ	ERA5
42	WSM6	KF	YSU	GFS	ES	KF	MYJ	ERA5	KS	KF	MYJ	ERA5	KS	KF	MYJ	GFS
43	ES	BMJ	MYJ	GFS	ES	BMJ	YSU	ERA5	ES	BMJ	MYJ	GFS	KS	GFES	YSU	ERA5
44	WSM6	KF	YSU	ERA5	ES	GFES	MYJ	ERA5	ES	KF	YSU	GFS	KS	BMJ	YSU	ERA5
45	WSM6	GFES	YSU	GFS	ES	BMJ	YSU	GFS	ES	KF	YSU	ERA5	KS	KF	YSU	ERA5
46	KS	KF	YSU	GFS	ES	BMJ	MYJ	GFS	KS	GFES	YSU	ERA5	ATS	KF	YSU	ERA5
47	ES	BMJ	YSU	GFS	ES	KF	MYJ	GFS	KS	BMJ	MYJ	ERA5	WSM6	KF	YSU	ERA5
48	ATS	BMJ	MYJ	GFS	ES	BMJ	MYJ	ERA5	KS	BMJ	YSU	ERA5	WSM6	KF	MYJ	ERA5

Taylor diagram (Taylor, 2001) summarizes the model performance by presenting some statistics between the model and the reference. These statistics are the correlation coefficient, the root-mean-square difference, and the ratio of standard deviations. Figure 3.4 comprises Taylor diagrams with regard to the different model parameterizations and initial and lateral boundary data for each event. Each dot in this figure indicates a combination. In Figure 3.4, there are 96 combinations under the column of the parameterization and initial and lateral boundary data inputs except for the CU scheme (There are 48 combinations for this column) since all the simulations are run with a nested run, but CU scheme is inactivated for the 3 km grid spacing. The shape and the colors of the dots represent the used parameterizations and initial and lateral boundary data source in the corresponding combination. The statistics of the combinations in Figure 3.4 are obtained by taking the mean of the statistics calculated between the stations and the closest grid to the stations for each combination. OBS is the optimal point (i.e., correlation=1, ratio of standard deviations=1, and the root-mean-square difference=0). So, if a model outcome is closer to the OBS, then it is a better outcome. According to the TOPSIS results, MYJ & ERA5 combination is detected at all the best scenarios of the EBS-summer event. Although the Taylor diagram results are commonly similar to the TOPSIS results, a few of the best scenarios of the Taylor diagram includes GFS. This difference derives from that ERA5 is more successful than GFS in categorical metrics. For instance, the mean of the POD index is 0.45 for the GFS scenarios, while the mean POD value of the ERA5 scenarios is 0.53. It is worthwhile to remind that categorical metrics are used in the TOPSIS algorithm, whereas they are not taken into consideration in the Taylor diagram. Also, GFS and ERA5 values are highly separable when the MED-autumn event is considered. For this event, the scenarios with GFS widely find out higher correlation values, but the ratio of the standard deviation is mostly higher as well. The best MP, CU, boundary layer schemes, and input data of the event are ES, GFES, YSU-MYJ, and ERA5, respectively. Both PBL schemes in this event show a very similar performance.

Further, it is possible to mention some local clusters in terms of the MP scheme for the events. However, the clustering is quite evident at the EBS-autumn analyses. For EBS-autumn clusters, the correlation and root-mean-square difference values are similar. Nonetheless, the standard deviation rates are highly variable and are, therefore, the main reason for clustering. The standard deviation of the WRF estimates produced by the scenarios that include the KS scheme is lower than the observations. Contrarily, the WSM6 scheme generates time series with more variability. The ratios of the standard deviations aggregate around 1 for the other two MP schemes. Differently from the other events, the values of the root-mean-square that belong to 96 members are close to each other for the EBS-autumn incident. Correlation values in EBS-autumn stay between 0.4-0.6 while they stay less than 0.4 in the other three events (EBS-summer, MED-summer, and MED-autumn). Moreover, for the MED-summer event, the figure proves that there are four different scenarios, the standard deviations of which are nearly the same with the reference. These four scenarios are composed of the combinations of ES - KF(GFES) - YSU - ERA5 - 9 km (3 km). The highest variability (standard deviation) in all parameterization schemes and initial and lateral boundary datasets is observable in the MED-summer event.

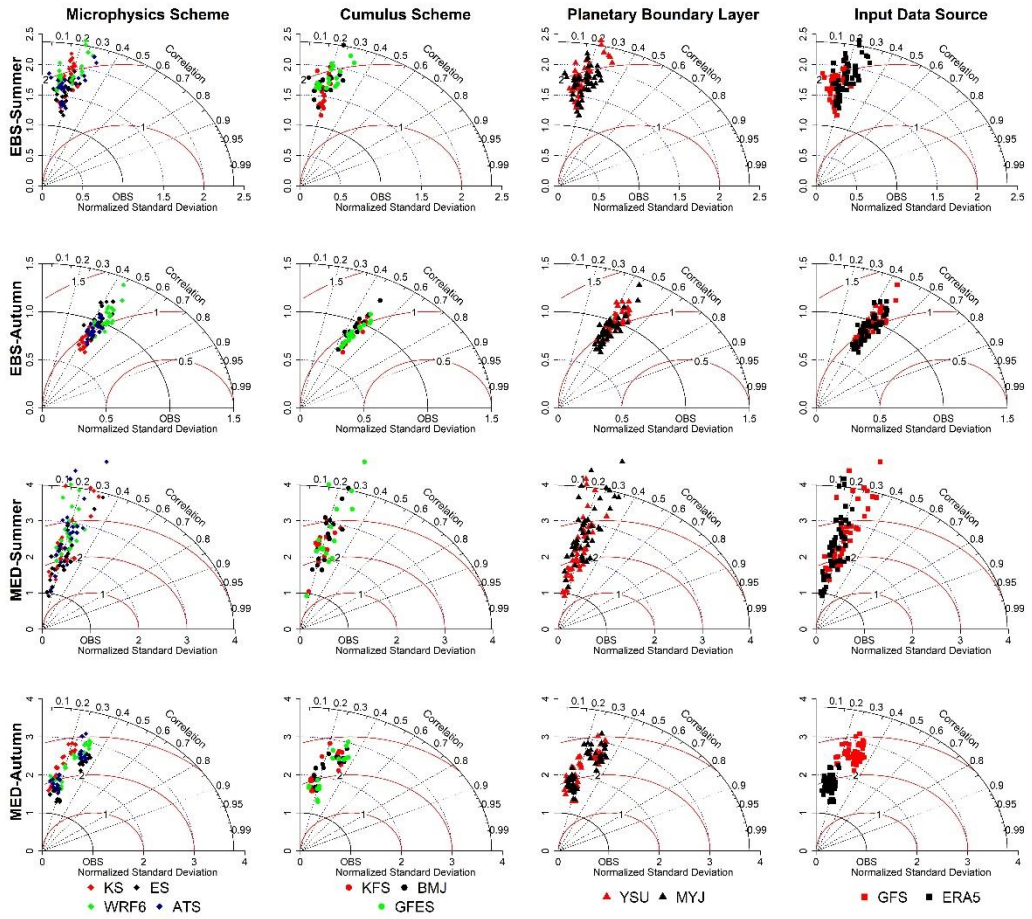

Figure 3.4. Taylor diagram for the different parameters and events. OBS is the best point. The red semi-circles show the RMSE differences, and the black quarter-circles, except for the one indicating the correlation values, present the standard deviation ratios. The presented statistics for each scenario are obtained by taking the mean of the statistics, which are calculated between the stations and the closest grid.

Because of the complexity in its occurrence, the primary factors behind the summer precipitation are still uncharted (Tabari and Willems, 2018). Therefore, forecasting summer extremes is a challenging issue. Assuming that the summer events are convective and small-scaled, the evaluation of the performance of a model at the event center is noteworthy. Figure 3.5 shows the hourly variation of the summer event centers from observed stations in EBS and MED and the closest grid ensemble. As a result, the model cannot thoroughly solve the system causing extreme rainfall

at the central station of the MED event. FAR index for the best and the worst ten scenarios is close to each other, which is about 0.8, along with showing a low correlation value with the central station. For the EBS-summer event, while the peak amount at the central station is 81.1 mm, this amount is 12 mm for the ensemble mean of the best ten scenarios. In other words, the model has difficulty estimating the peak amount. However, the peak hour corresponds to the 34th hour after the simulation started, is captured by the model. Further, the FAR and POD index and the correlation coefficient between the ensemble mean of the best ten scenarios and the central station are 0.41, 0.91, and 0.84. These values prove that the WRF ensemble is successful not only in describing the fluctuation but also in detecting precipitation at an hourly scale.

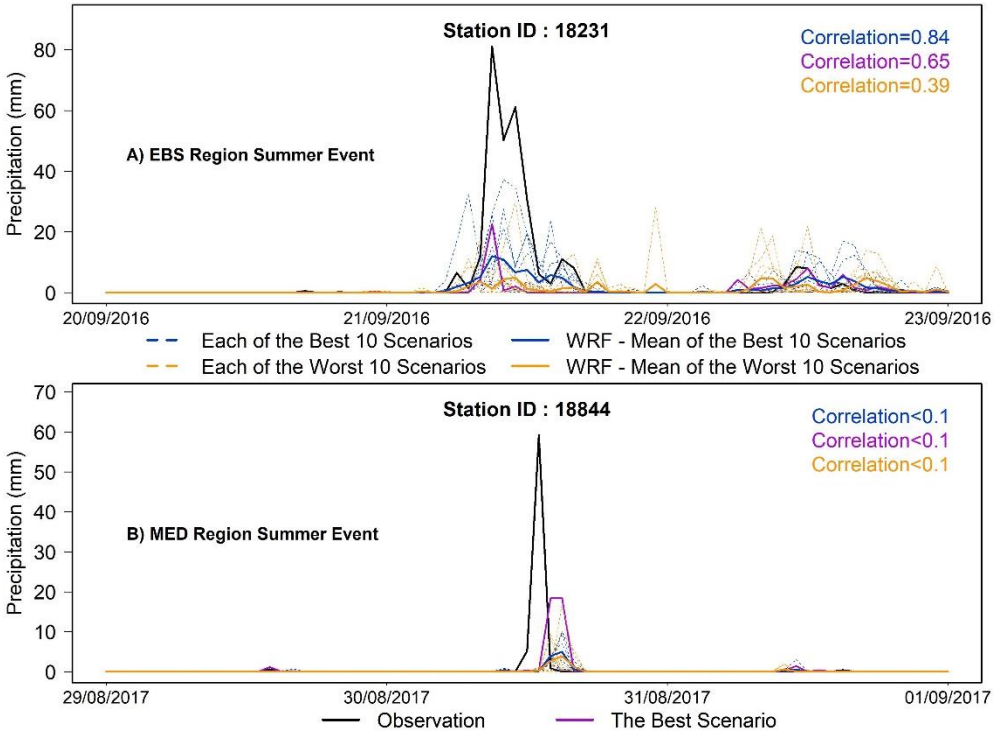

Figure 3.5. The time-series for the central stations of the summer events and the ensembles of the closest grids to the central stations. The correlation values colored with dark blue, purple, and orange show the linear relationship between the central stations of the events and the ensemble mean of the best ten scenarios, the best scenario, and the ensemble mean of the worst ten scenarios, respectively.

The spatial distribution of the extreme precipitation events is evaluated using the ensemble of the best ten scenarios and the best scenarios in Figure 3.6 (for EBS) and Figure 3.7 (for MED). All maps in the figures consist of total precipitation values that occur per each grid on the event day. The first row of the figures shows the spatial dispersion of the in-situ measurements distributed over the region using the IDW method because the stations almost uniformly spread over the regions. The figures provide information about the 3 km horizontal grid spacing analyses. The observation maps agree that the rainfall event occurs around one center for EBS-summer and a few centers for EBS-autumn events rather than occurring across the region. For both events, the event centers are commonly located near the sea. This condition may be triggered by the orographic influences since the mountains lie parallel to the sea throughout EBS coasts. Moreover, the rainfall is considerably intense and occurs over the spatially smaller scales for the summer events of the regions. Although the EBS-summer seems to be amplified by the orography as well, both summer events are mainly driven by the local convective systems.

The second and the third rows show the spatial distribution of the ensemble mean of the best ten scenarios and the best scenarios. The WRF maps of the EBS-autumn event support the inferences about the orography and demonstrate precipitation all along the coast. Besides, the ensemble mean map accurately detect the spatial positions of most of the event centers. The convection-permitting analysis spatially overestimates the extreme event; however, the observed peak amounts are still underestimated. On the contrary, the MED-autumn event is overestimated in terms of both spatial scale and precipitation amount. The overestimation is more apparent for the best scenario case than the ensemble mean of the best ten scenarios case. In general, the ensemble mean of the best ten scenarios improves the findings of the best scenario. Exceptionally, the spatial location of the convective event center is more accurately determined by the best scenario of the MED-summer event.

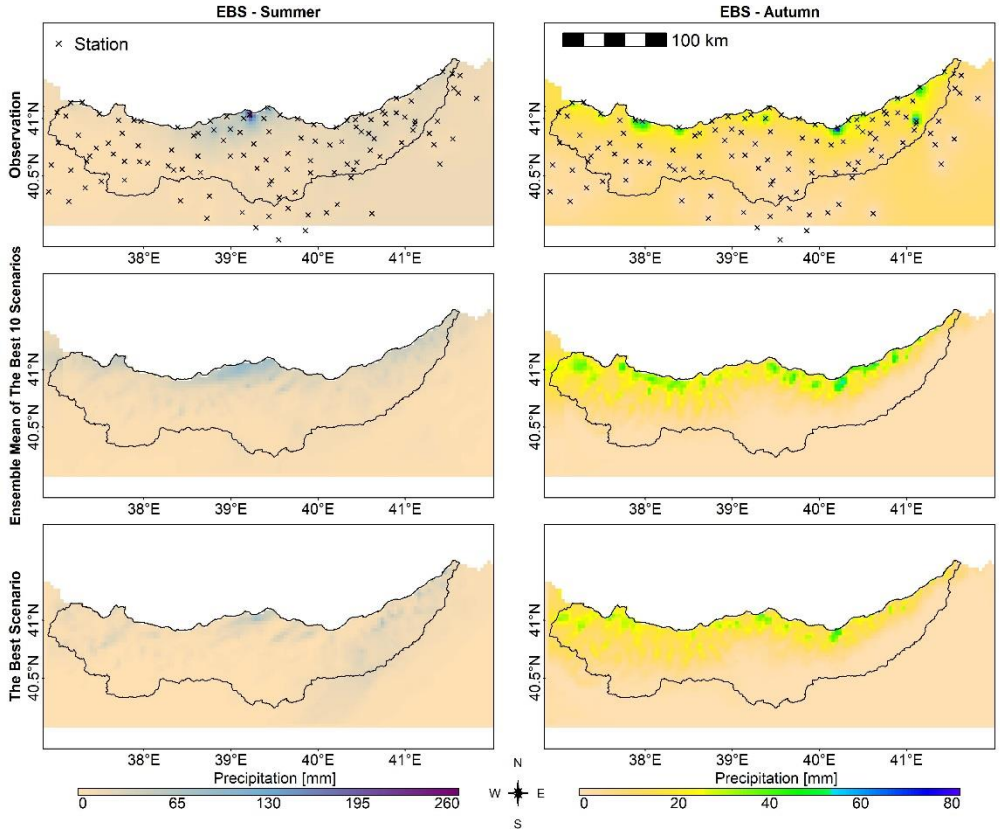

Figure 3.6. The spatial distribution of the daily total precipitation of the EBS events for the observations, the ensemble mean of the best 10 scenarios, and the best scenarios regarding 3 km spatial resolution on the event day. The point observations are converted into gridded data through the IDW method.

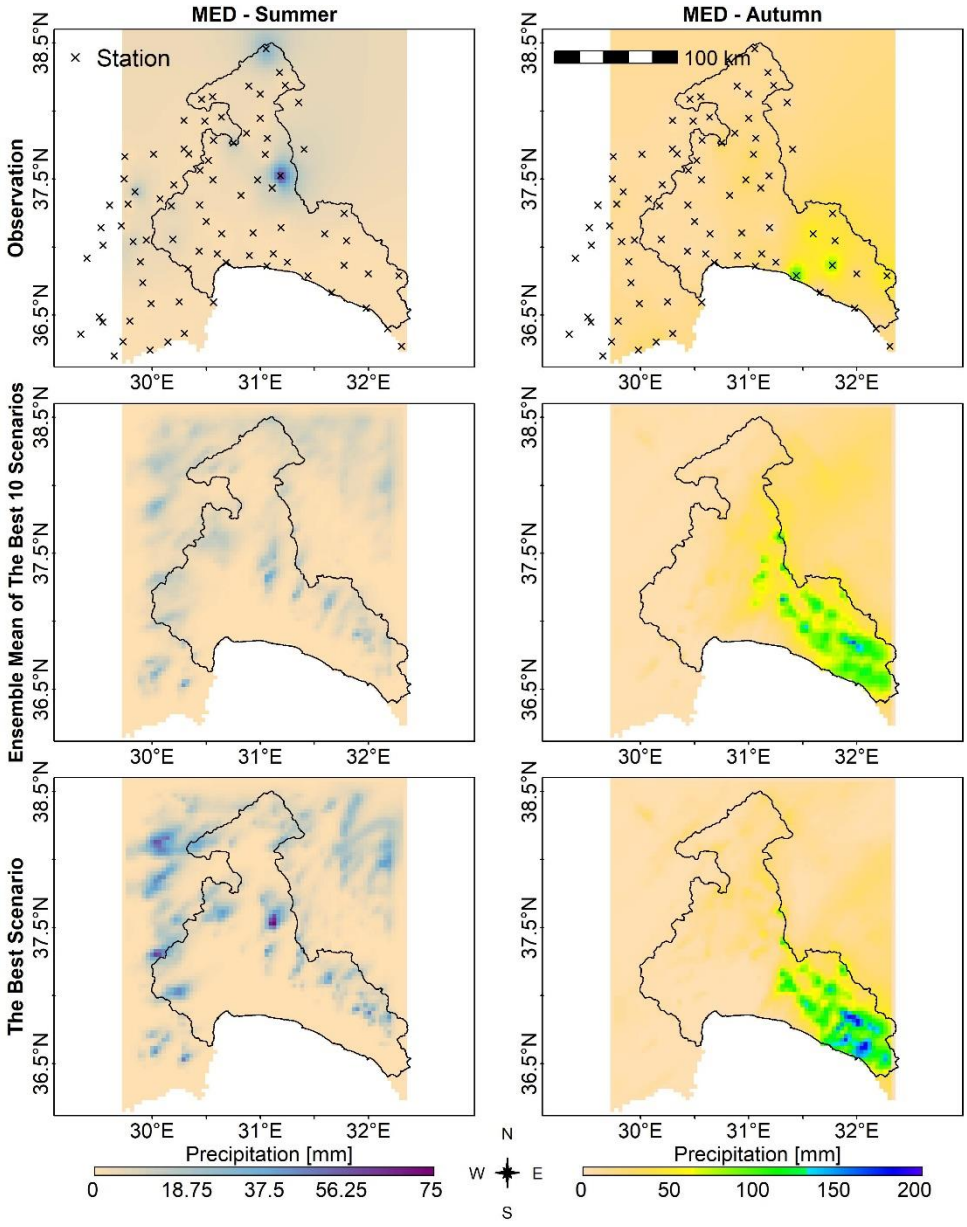

Figure 3.7. The spatial distribution of the daily total precipitation of the MED events for the observations, the ensemble mean of the best 10 scenarios, and the best scenarios regarding 3 km spatial resolution on the event day. The point observations are converted into gridded data through the IDW method.

Figure 3.8 is a useful visual to further investigate the orographic influences in precipitation extremes for the EBS-autumn event. In the first panel of the figure, the spatial distribution of the precipitation amount in 3 km horizontal grid spacing is

presented for the peak hour relative to the areal mean. A cross-section (A-B) of the slice that includes the grid having the maximum hourly precipitation is obtained in the south-north direction. The second panel shows the mixing ratio and the vertical wind speed (i.e., contours) distributions regarding the changing WRF vertical level (i.e., sigma level) and the latitude along the cross-section. All the WRF-outputs (i.e., mixing ratio, precipitation, and wind speed) in this figure are the ensemble mean of the best ten scenarios for the 3 km spatial resolution. Also, the red line provides the value of the altitude corresponding to each latitude. The primary aim of the graph is to determine whether the orographic barrier triggers the condensation of the moisture coming from the sea or not as well as detecting the vertical level of the cloud formation causing the extreme precipitation and finding out the magnitude and the direction of the vertical wind waves over the region. According to the figure, there is intense cloud formation around the 10^{th} vertical level and over the 41°N latitude. The vertical wind-wave up to 0.6 m/s is detected in the upward direction for this part. The cloud formation and wind wave overlap with the region on which the maximum precipitation originates. Likewise, the altitude of the maximum precipitation area is around 250 m. This is the first hilly region that the moisture encounters while coming from the sea. Even though they are not as strong as the cloud formation driving the maximum precipitation, the clouds generating precipitation appear at higher altitudes than 250 m as well. The cloud formation stops at approximately 800 m altitude. Neither precipitation nor cloud formation is observed at the places higher than this altitude. Based on these inferences, the orography seems one of the leading precipitating causes of the EBS-autumn extreme precipitation events.

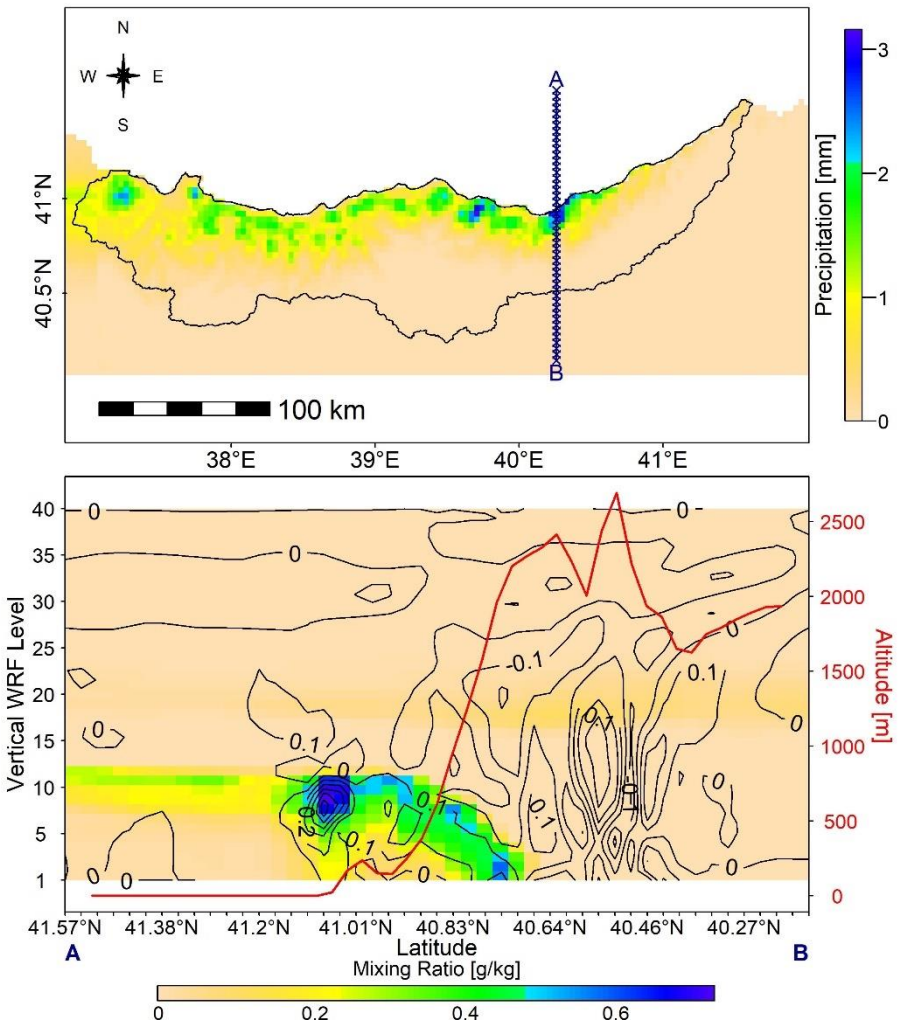

Figure 3.8. The first panel shows the spatial distribution of WRF-derived precipitation that has 3 km horizontal grid spacing for the peak hour relative to the areal mean. The x-axis of the second panel indicates the latitudes for the A-B cross-section, while the first y-axis shows the vertical WRF-levels. The colored background presents the mixing ratio distribution concerning the latitudes and the vertical levels, whereas the counters demonstrate the vertical wind magnitude and direction in m/sec. The positive wind values indicate the upward wind movement, and the negative ones are the indicator of the downward wind circulation. The values of precipitation, mixing ratio, and wind speed are obtained by taking the ensemble mean of the best ten scenarios. The second y-axis demonstrates the altitude values for the corresponding latitudes.

3.1.3 Validation of the selected best scenarios with the independent events

The performance of the selected best ten combinations is tested for the independent events occurring over the same region and in the same season. Figure 3.9 the results of the calibration and validation ensembles in terms of the values of some metrics. The metrics are calculated between each station and the ensemble mean of the closest grid (i.e., the ensemble mean of the best ten scenarios for the calibration events and ensemble mean of the ten scenarios for the validation events.). The boxes in this figure represent the dispersion of the statistical measures of stations for these events.

As expected, both categorical and other statistical measures decrease in the validation period as these measures are calculated through independent events. The chaotic situation of the atmosphere is responsible for the changes in statistical measures between two events, even though the similar (same) model configuration is used. Still, there are some situations at which the indices are as successful as calibration values. For instance, the categorical metric values are very close to each other for the calibration and validation events of the MED-autumn. Similarly, although the range of it is slightly more extensive, the median value of the RMSE is lower for the validation event of the EBS-summer compared to the calibration event. The selected physics configurations for these two regions and seasons are particularly appropriate to use in future storm simulations over these domains.

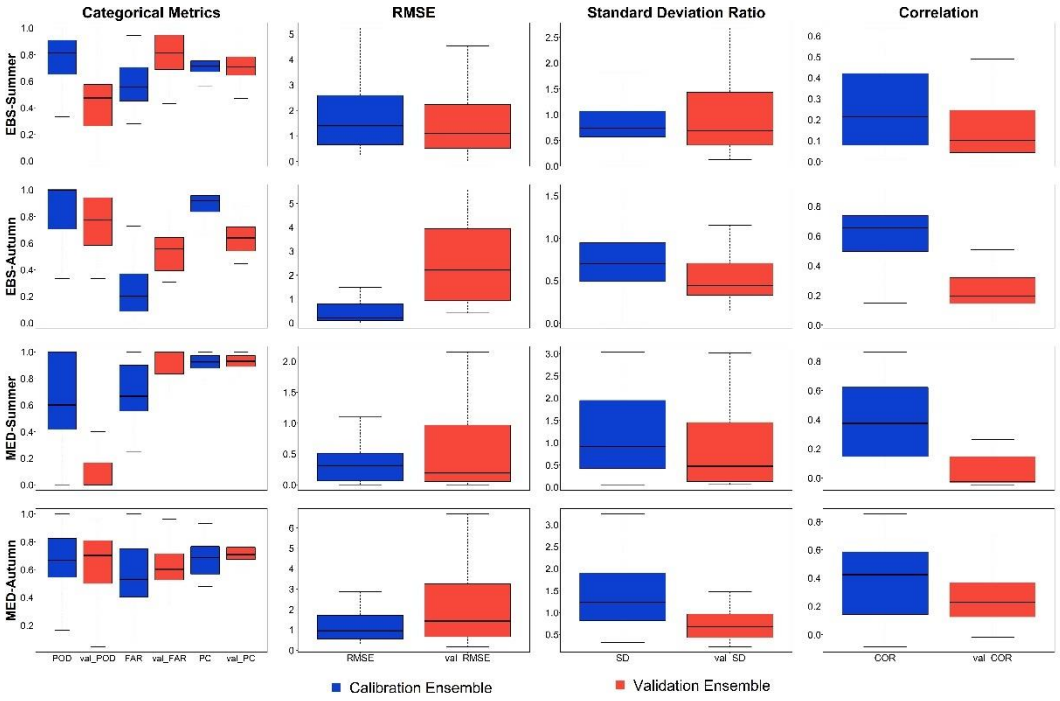

Figure 3.9. The comparison of the performance of the calibration and validation ensembles

For the validation events, the performance of the WRF model in precipitation generation is compared with the performance of the ERA5 dataset, which is one of the two data sources used in this study as the initial and lateral boundary conditions for the constructed WRF models. The precipitation forecasts of the other data source, GFS, are not compared with the WRF results since GFS forecasts are not provided in the hourly time scale. It is worthy to state that the comparisons are made based on the area-averaged values because ERA5 data and WRF ensembles have different spatial resolutions. Figure 3.10 demonstrates the fluctuations of the time series of the observations, WRF ensemble mean, and ERA5 mean data for each event. The TP ratios indicate the fraction of the cumulative precipitation generated by the models to the cumulative precipitation acquired from the stations for the simulation periods. First of all, the total precipitation amount that occurs in the EBS-summer and MED-autumn events is precisely accumulated by the WRF ensemble. However, the model underestimates the total amounts of the EBS-autumn and MED-summer events. Especially for the MED-summer event, both models highly underestimate the total

amount and have a relatively low correlation with the observations because of the strong convection-driven occurrence mechanism of the summer events. This mechanism results in very intense and short duration precipitation. Indeed, WRF catches the time of the first peak of the validation event, but it misses the subsequent essential precipitation peak and thereby underestimates the total precipitation amount. Checking the sensitivity of the model against different sea surface temperatures may be a valuable contribution to the improved simulation of convective summer events (Senatore et al., 2019). Moreover, the correlation between the observations and WRF is more powerful compared to the ERA5 except for the EBS-summer event. The positive contribution of the dynamical downscaling to the TP ratio of the MED-autumn and the correlation of the EBS-autumn events is notable. To conclude, though there are some exceptions, WRF outputs are commonly more successful than the ERA5 precipitation estimates for the selected validation events.

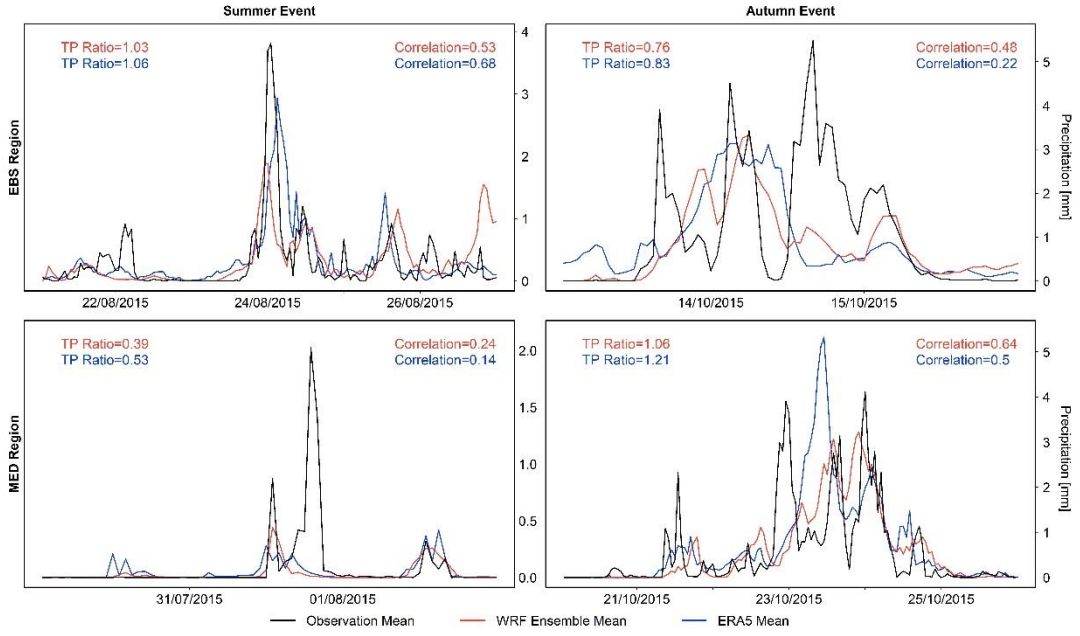

Figure 3.10. The performance comparison of the WRF- and ERA5-derived precipitation for the validation events

3.2 Contribution of the WRF & WRF-Hydro coupling and satellite soil moisture initialization to the accuracy of hydrometeorological forecasts

3.2.1 Calibration and validation of the WRF-Hydro-SA

Table 3.3 shows the statistics of the best trial of each calibration step and KGE/NSE values of the run with the default and calibrated parameter combinations. The best trial indicates the run giving the highest KGE value for the first three scenarios and the highest NSE value for the MED-NSE scenario.

The calibrated values obtained from two different calibration scenarios performed for the EBS region (i.e., daily and hourly) are different for the REFKDT, SLOPE, and MAnnN parameters. The calibrated REFKDT value is lower for the EBS-daily scenario than the EBS-hourly scenario, whereas the calibrated SLOPE value of the EBS-daily scenario is relatively higher. The infiltration rate at the EBS-daily simulation is lower because of this low REFKDT value. Also, the water transition from the soil to the bucket model under the soil is more for the EBS-daily scenario, owing to the higher SLOPE value. In a word, in the EBS-daily scenario, a lower amount of water enters the soil, and more water exits. For instance, for the validation run forced with observed precipitation, the basin average soil moisture values of the topmost soil level (i.e., the soil level at which infiltration occurs) and the lowest soil level (i.e., the soil level just above the bucket model) are 0.27 and 0.29 for the EBS-daily scenario, while they are 0.28 and 0.31 for the EBS-hourly scenario. Further, the calibrated MAnnN value is lower for the EBS-hourly scenario than the EBS-daily scenario. In other words, the model calibrated considering the hourly data perceives the river bed as less rough. The reason is that Arhavi, the calibration basin, is a steep and small subbasin. Therefore, the surface runoff in the system reaches its peak quickly (i.e., sometimes within hours after the start of precipitation), which is possible with lower roughness. Finally, the improvement of the KGE statistic in the EBS-daily scenario (i.e., 14%) is greater than in the EBS-hourly scenario (i.e., 1%).

Due to varying performance metrics, the calibrated parameter values differ for the MED-KGE and MED-NSE scenarios. The primary motivation of the NSE is testing the capacity of the model to catch the variation of the observed hydrograph and the peaks. On the other hand, the KGE has three different focuses: alpha (i.e., the ratio of the standard deviation of the model to the standard deviation of the observation), beta (i.e., the ratio of the mean of the model to the mean of the observation), and R. For the REFKDT parameter, the simulation initiated with the calibrated value selected by the MED-NSE (i.e., 3.75) are more successful at the statistics of RMSE, R, and MAE than the simulation run by the calibrated value chosen by the MED-KGE (i.e., 0.25). However, in Bias statistics, the model causes better KGE for the REFKDT value of 0.25 than 3.75 by improving the beta statistic. Moreover, the MED-KGE model has greater runoff volume than the MED-NSE model. The Bias is -34.28% for the REFKDT value of 0.25 and -38.12% for the REFKDT value of 3.75. The MED-KGE scenario improves the Bias as the calibration steps progress, but there is no such improvement for the MED-NSE scenario. At the end of the calibration process, Bias decreases to -26.77% in the model calibrated with KGE, while Bias improvement is limited (i.e., -35.54%) in the model calibrated with NSE. Lastly, the KGE statistic increases by 13% through the KGE-oriented calibration. The NSE value shows an increase of only 2% in the NSE-oriented calibration.

Table 3.3 The statistics calculated between the streamflow observations and the model outputs simulated with the best parameter value selected as a result of 10 trials for each parameter. The statistics are calculated based on daily streamflow data for the EBS-daily, MED-KGE, and MED-NSE scenarios, whereas they are obtained based on hourly streamflow data for the EBS-hourly scenario. All calculations are carried out with the unit of m^3/s. Black bold statistics are obtained when the model is run with the default parameters, and bold red statistics show the performance of the calibrated model.

Calibration scenario	Parameter	Calibrated parameter value	RMSE	NSE	R	MAE	KGE	Bias (%)
EBS-daily	Default	-		**0.41**			**0.64**	
	REFKDT	0.75	8.01	0.52	0.82	4.98	0.72	-0.53%
	SLOPE	0.6	7.85	0.53	0.79	5.18	0.77	1.92%
	OVROUGHRTFAC	0.1	7.57	0.57	0.79	5.09	0.79	0.23%
	MAnnN	2.1	7.4	0.59	0.8	5	0.8	0.30%
	LKSATFAC	1120	7.38	**0.59**	0.8	5	**0.8**	0.08%
EBS-hourly	Default	-		**0.21**			**0.64**	
	REFKDT	2.75	13.68	0.21	0.66	6.59	0.64	0.90%
	SLOPE	0.3	13.68	0.21	0.66	6.59	0.64	0.90%
	OVROUGHRTFAC	0.1	13.42	0.24	0.66	6.54	0.65	0.61%
	MAnnN	1.3	13.39	0.25	0.66	6.58	0.65	0.84%
	LKSATFAC	1000	13.39	**0.25**	0.66	6.58	**0.65**	0.84%
MED-KGE	Default	-		**0.74**			**0.56**	
	REFKDT	0.25	29.23	0.59	0.82	19.73	0.59	-34.28%
	REFDK	$2*10^{-6}$	29.23	0.59	0.82	19.73	0.59	-34.28%
	SLOPE	1	27.92	0.63	0.83	17.94	0.67	-26.67%
	OVROUGHRTFAC	1	27.92	0.63	0.83	17.94	0.67	-26.67%
	MAnnN	2.3	25.35	0.69	0.86	16.41	0.68	-26.72%
	LKSATFAC	10000	24.92	**0.7**	0.87	16.33	**0.69**	-26.77%
MED-NSE	Default	-		**0.74**			**0.56**	
	REFKDT	3.75	23.23	0.74	0.93	16.32	0.56	-38.12%
	SLOPE	0.4	23.19	0.74	0.92	15.83	0.58	-36.10%
	OVROUGHRTFAC	0.1	22.83	0.75	0.93	15.76	0.59	-35.65%
	MAnnN	0.9	22.83	0.75	0.93	15.8	0.59	-35.64%
	LKSATFAC	2230	22.3	**0.76**	0.93	15.84	**0.61**	-35.54%

The hourly streamflow outputs of the calibrated models forced with the parameter values obtained from the EBS-daily and EBS-hourly scenarios are represented in Figure 3.1. The KGE values that are calculated between the hourly streamflow outputs of the models and DSI observations for each month of the calibration period are provided in Table 3.4. The results show that the KGE values obtained for the EBS-hourly scenario are higher than the ones for the EBS-daily scenario at 9 of the 12 months. In contrast, for September, the KGE value of the EBS-daily scenario is higher than the EBS-hourly scenario. The main reason for this situation is that the EBS-hourly scenario overestimates the first peak at the beginning of the month, which brings about a dramatic decrease in its KGE coefficient. This overestimation might originate from the lower MAnnN value of the EBS-hourly scenarios causing less rough channel surface. Even though the EBS-hourly scenario has less rough channel surface, there is no consistent overestimation problem for the EBS-hourly model along the calibration period since its soil stores higher moisture in comparison to the EBS-daily model, as it is explained above. Nevertheless, for this event, a relatively high precipitation amount results in overestimation, most probably by directly overfeeding the channel and turning into surface runoff before the soil reaches the saturation (i.e., precipitation rate might be higher than the infiltration rate as in Horton overland flow).

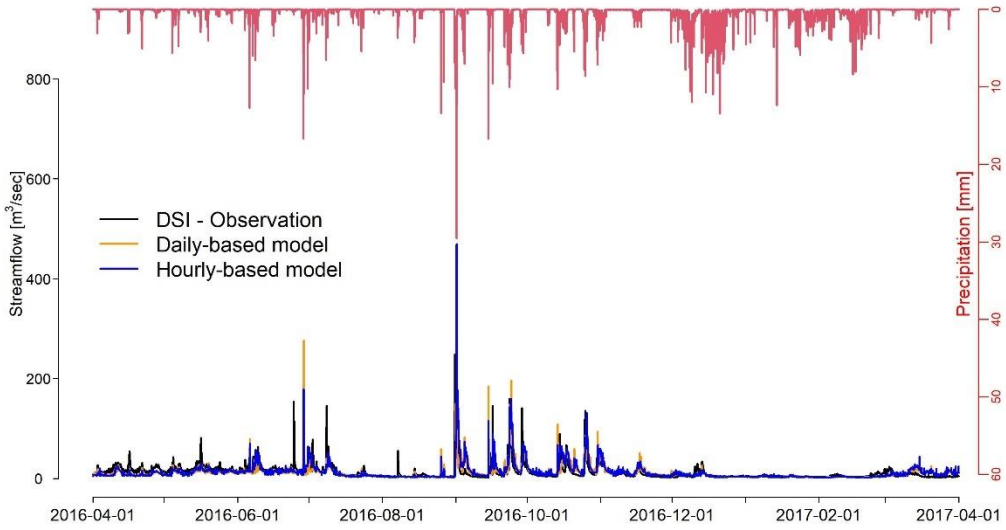

Figure 3.11. Hourly streamflow data from in-situ measurement and WRF-Hydro-SA models operated with the calibrated parameters obtained as a result of EBS-daily and EBS-hourly calibration scenarios for the Arhavi DSI station. The precipitation data is the area averaged precipitation for the corresponding subbasin.

Table 3.4 KGE coefficients obtained between the hourly streamflow of Arhavi DSI station and WRF-Hydro-SA models operated with the calibrated parameters obtained as a result of EBS-daily and EBS-hourly calibration scenarios. The coefficient is calculated for each month separately.

Calibration scale	**KGE**											
	Apr-16	May-16	Jun-16	Jul-16	Aug-16	Sep-16	Oct-16	Nov-16	Dec-16	Jan-17	Feb-17	Mar-17
daily	0.24	0.37	0.22	0.34	0.30	0.52	0.47	0.62	0.25	0.33	-0.03	-0.31
hourly	0.25	0.38	0.50	0.51	0.04	0.25	0.43	0.64	0.26	0.40	0.08	-0.25

In WRF-Hydro, there are two options for the distribution of groundwater (and a third option: it can be considered a sink term). The first one is the exponential bucket model, and the second one is pass-through. In the former, the water is transferred from the bottom soil layer to the underlying groundwater bucket and accumulated. After the bucket fills up, the excess water feeds the channel flow. On the other hand,

in the pass-through option, the water is directly transferred to the channel bypassing the bucket (D. J. Gochis et al., 2018). Accordingly, the exponential bucket model is expected to give better streamflow outputs for long-term simulations. In contrast, the pass-through option is highly recommended for short-term extreme event simulations. In this study, even though the simulations are performed for a long-term period, the pass-through option is used since one of the main aims here is to successfully simulate extreme events in the calibration period. However, we realize that the model underestimates the recession part of the streamflow (Figure 3.12). To understand whether this situation is associated with the groundwater option, the WRF-Hydro-SA model having the parameter values obtained as a result of the MED-KGE scenario is initiated with the option of the exponential bucket model. According to the results, the influence of the choice of groundwater option on streamflow outputs is not significant for our case (Figure 3.12).

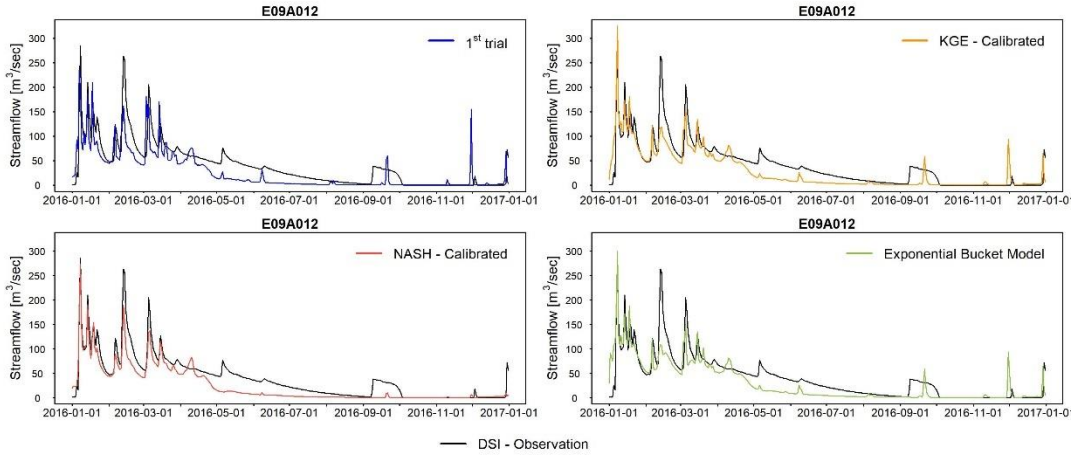

Figure 3.12. DSI observation and WRF-Hydro-SA streamflow outputs from different run conditions for the Oymapınar basin

The parameters calibrated for the EBS-daily, EBS-hourly, and MED-KGE scenarios are validated for different periods, sub-basins, and input precipitation sources (Table 3.5). The performance of the models dramatically decreases in validation periods. Three components of the KGE statistics are focused on understanding the potential reasons for these decreases.

Figure 3.13-A shows the KGE values and components (i.e., alpha, beta, and correlation) for each calibration and validation simulation of the MED-KGE scenario. It can be seen that from Figure 3.13-A, the beta value is around 0.8 for the best of the calibration simulations. In the validation period, the beta value increases to around 1 for the WRF-Hydro-SA model outputs forced with the observed and corrected radar precipitation. In other words, the model is more successful in the validation period in terms of the beta statistic. This outcome is interesting; because the total flow volume is more accurately estimated in the validation period despite the dramatic decrease in the KGE. As for the correlation statistic, the model is more successful during the calibration period; but the performance decrease during the validation period is slight. Thus, the decrease in the KGE originates from neither beta nor correlation statistics. However, the alpha statistic is around 90% for the best calibration simulation and this value rises to around 200% for the validation scenarios. Namely, although the WRF-Hydro-SA model successfully determines the total flow volume during the validation period, it cannot propagate the total volume correctly throughout the time series and misses the variability.

Figure 3.13-B is formed to determine why the WRF-Hydro-SA fails to distribute the total water volume through the time series. The figure demonstrates the precipitation, temperature, streamflow, and snow water equivalent variables for different products along the validation period. At the beginning of the validation period, precipitation occurs, as seen from the observation data, and the basin responds rapidly to the precipitation by generating the streamflow. For this period, a large portion of the precipitation is rainfall since the observed temperature (i.e., the black lines) is frequently above 0°C. However, the WRF-Hydro-SA model is run using the WRF-derived temperature (i.e., the purple lines) as input and the WRF-derived temperature values are commonly below 0°C in this period. So, the WRF-Hydro-SA model considers the precipitation given to it as substantially snow, not rain. Due to this situation, the model underestimates the streamflow in early January and stores a good part of the precipitation as snowpack. The snowpack starts to melt slowly towards April, thanks to the temperature increase. When the model encounters precipitation

around April at above 0°C, it overestimates the streamflow because of the melting snow contribution to the runoff budget in addition to its response to rain. The overestimation lasts until mid-May when snowpack budgets consume. The model performance is better in the calibration period since it does not encounter any condition causing snow-rain complications in 2016. The circumstance for the other nine subbasins is also similar.

After, the validation simulations are repeated using the observed temperature to recover the systematic error originated by the temperature input. However, this time, overestimation occurs for the streamflow output in the first three months, and underestimation occurs in April and May (Figure 3.13-B). The described problem does not entirely disappear. Still, this study proves that the input temperature data deserve more attention, especially for the long-term WRF-Hydro runs covering the snowy seasons.

Table 3.5 The KGE values calculated between the streamflow observations and WRF-Hydro-SA outputs obtained from the simulations initiated with the calibrated parameter combinations. Red bold numbers show the best KGE for the corresponding row. Subbasins are numbered starting from the eastern-based on Figure 2.5-A for EBS and Figure 2.5-C for MED.

			KGE (with respect to the input precipitation data source)			
Calibration scenario	**Time interval**	**Basin No**	**In-situ**	**Uncorrected radar**	**Corrected radar**	**WRF-SA**
MED-KGE	**Calibration [01.01.2016-01.01.2017]**	Basin 3	0.69	-	-	-
	Validation [01.01.2017-01.10.2017]	Basin 3	0.27	0.1	0.3	**0.37**
		Basin 1	-0.54	-1.33	-0.61	**-0.19**
		Basin 2	-0.25	-1.25	-0.52	**-0.23**
		Basin 4	-1.61	**0.55**	-0.06	-21.22
EBS-daily	**Calibration [01.04.2016-01.04.2017]**	Basin 1	0.8	-	-	-
	Validation [01.04.2017-01.10.2017]	Basin 1	-0.72	**-0.69**	**-0.69**	-1.1
		Basin 2	**0.51**	**0.51**	**0.51**	0.28
		Basin 3	-2.03	**-1.24**	-1.75	-2.75
		Basin 4	0.66	0.53	**0.67**	0.51
		Basin 5	**0.38**	-0.21	0.21	0.16
		Basin 6	0.69	0.56	**0.71**	0.4
EBS-hourly	**Calibration [01.04.2016-01.04.2017]**	Basin 1	0.65	-	-	-
	Validation [01.04.2017-01.10.2017]	Basin 1	-1.85	**-1.73**	-1.75	-2.3

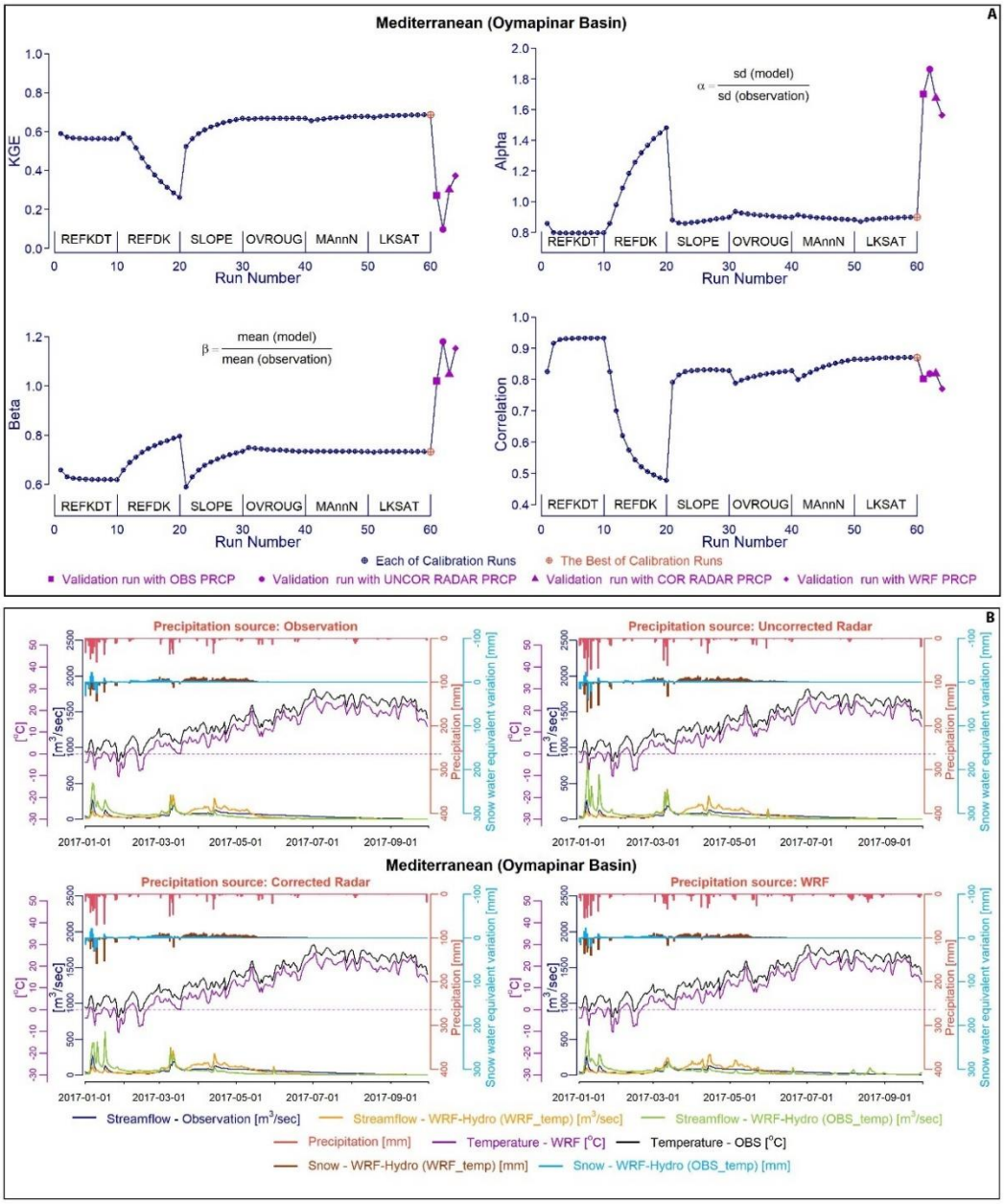

Figure 3.13. Panel A: The KGE values and their components obtained in each calibration step and validation simulations for the Oymapınar basin (i.e., the calibration basin of the MED region). Panel B: The precipitation, streamflow, and temperature time series of existing/obtained products for the Oymapınar basin along the validation period. Streamflow values are provided for the point at the exit of the basin, while the temperature and precipitation values are the basin averages. The figure is obtained using R-programming language (R Core Team, 2020).

3.2.2 Short-term evaluation of hydrometeorological variables

This section discusses the hydrometeorological outputs of the four long-term simulations (i.e., for the period of 01.10.2015 – 01.10.2017) for some short-term periods.

Precipitation, air temperature, soil moisture, specific humidity, and soil temperature outputs of the atmospheric models (i.e., WRF-SA, WRF-Coup, WRF-SM-Coup) are evaluated for the meteorological stations in Arhavi and Döşemealtı districts of EBS and MED, which are notably flood-prone regions (Figure 3.14). The model performances are discussed for the hourly data of a one-month dry period (2017-July), considering the danger of convective floods and harmful drought events during the summer.

The WRF-SA model generally underestimates the daily minimum temperature values in EBS, but both coupled models are relatively successful in catching the daily minimum and peak temperatures. All three models, particularly WRF-SA, overestimate the minimum temperature values in MED, and the offline model (i.e., WRF-SA) is more accurate in predicting peak values. For the coupled models, even though changing the initial soil moisture data source does not significantly affect the temperature outputs, the precipitation and soil moisture outputs differ thoroughly. For instance, the WRF-SM-Coup model underestimates the precipitation event occurring on the 5th of July, whereas it is overestimated by the WRF-Coup model (Figure 3.14-A). This overestimation also causes a steep increase in soil moisture for the corresponding period. After reaching the peak point, the WRF-Coup model's soil moisture quickly decreases due to the high evaporation rate in summer, which results in local increases in the amount of specific humidity. Albeit specific humidity value decreases after a slight increase, decreases in the temperature make the air reach the dew point, and another precipitation event occurs a few days later. An increase in the air temperature and specific humidity just prior to the precipitation events in the EBS region indicates a typical cloud-precipitation signature formed by local summer convection. This character of the lower boundary layer is presented from all three

model runs. Moreover, the MED region is drier than the EBS region in summer (Figure 3.14-B). For the MED region, the soil moisture outputs of all models constantly decrease all along the month since the models produce almost no precipitation. Also, the decrease rate (i.e., slope) of soil moisture for coupled models (particularly for SM coupled run) is much higher than the decrease rate for the WRF-SA model. Moisture feedbacks from the surface to the atmosphere stay higher (higher specific humidity) for WRF-SM-Coup compared to the other two model runs. The soil moisture values of the WRF-SA model are higher than the soil moisture of the coupled models. Because of this, the soil temperature of the WRF-SA model is relatively low compared to the coupled models. Coupled models, especially for the MED region, show a higher daily amplitude of the soil temperature than WRF-SA. Drier (i.e., semi-arid) MED region exhibits more variable surface-air interaction resulting from differences introduced by three model runs. However, in the wet EBS region, the variability of such interaction is less pronounced by these model runs.

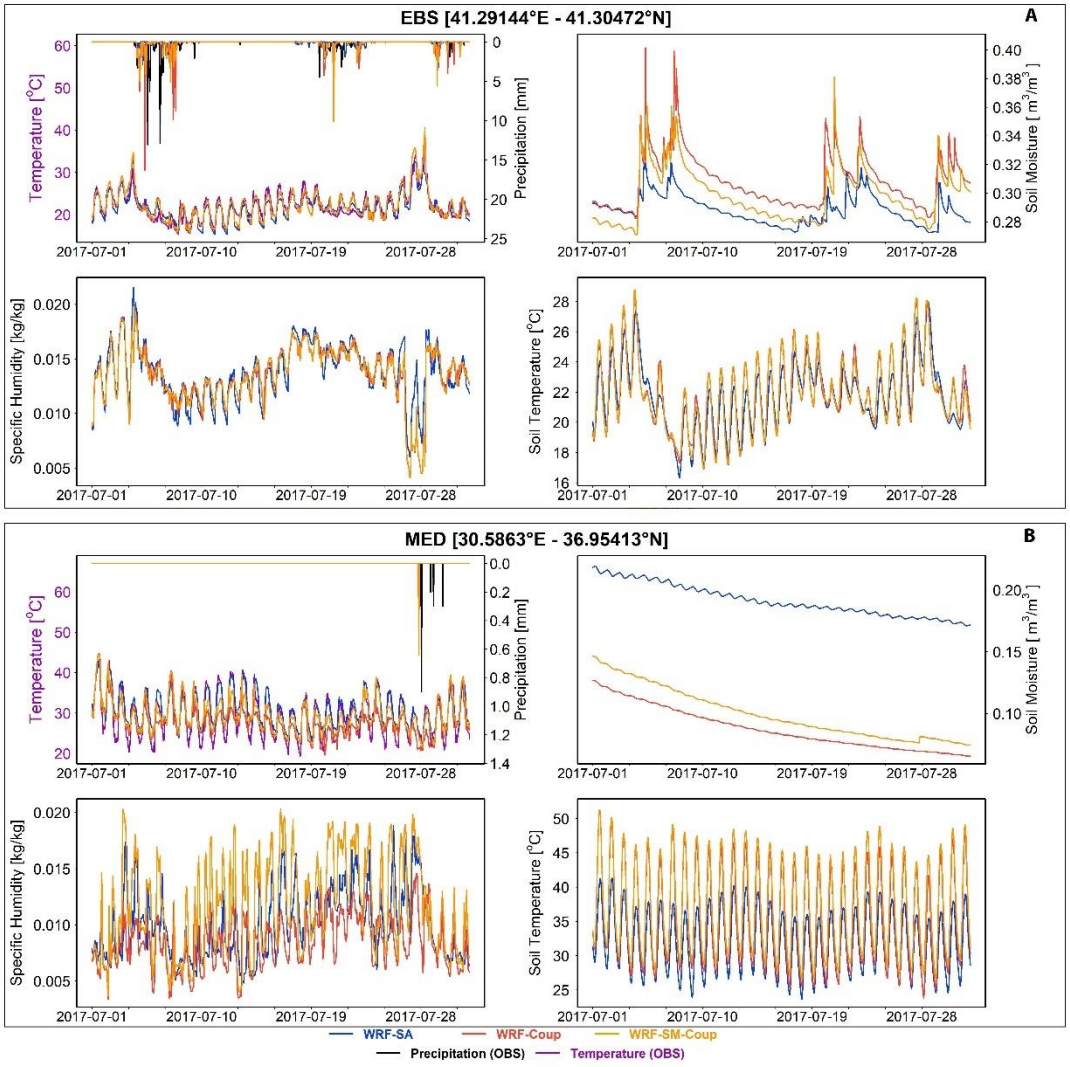

Figure 3.14. Hourly observations (for precipitation and temperature) at the Arhavi and Döşemealtı meteorological stations of the EBS and MED regions and the model outputs (for precipitation, temperature, soil moisture, specific humidity and soil temperature) at the closest grids to these stations for the July-2017. The figure is obtained using R-programming language (R Core Team, 2020).

Figure 3.15-A represents the spatial distribution of the observed precipitation (obtained via the IDW method) for the extreme precipitation event that occurred in EBS on 21.09.2016 at 10:00 am. Figure 3.15-B demonstrates the temperature, precipitation, specific humidity, and latent heat flux estimations of the WRF-SA, WRF-Coup, and WRF-SM-Coup models for the event time. The precipitation event

occurs on a small scale in the mid of the region, where the peak rainfall reaches 50 mm/h. The event arises on the seaside of the mountains parallel to the sea, indicating a strong contribution from orography. The WRF-Coup model simulates the peak precipitation with high accuracy in quantity and location. The WRF-SM-Coup successfully catches the peak precipitation amount, but it misses the actual occurrence location. The WRF-SA model, on the other hand, wrongly simulates the location and the magnitude of the extreme event. As consistent with the observed precipitation distribution, the initial soil moisture update in coupled model run diminishes the rainfall activities in the northeast of the EBS region. Availability of the humidity towards the topographical cross-section triggers rainfall enhancement together with elevated heat sources. Warmer air temperature over the sea, moisture transport from the sea to the mid of the Black Sea via wind, and greater near-surface humidity over this region well match the actual location of the peak precipitation event for both coupled model runs. The latent heat flux distribution is thoroughly changed by the coupled models especially for the northeastern part of the region, which shows the influence of the WRF-Hydro coupling on local moisture flux.

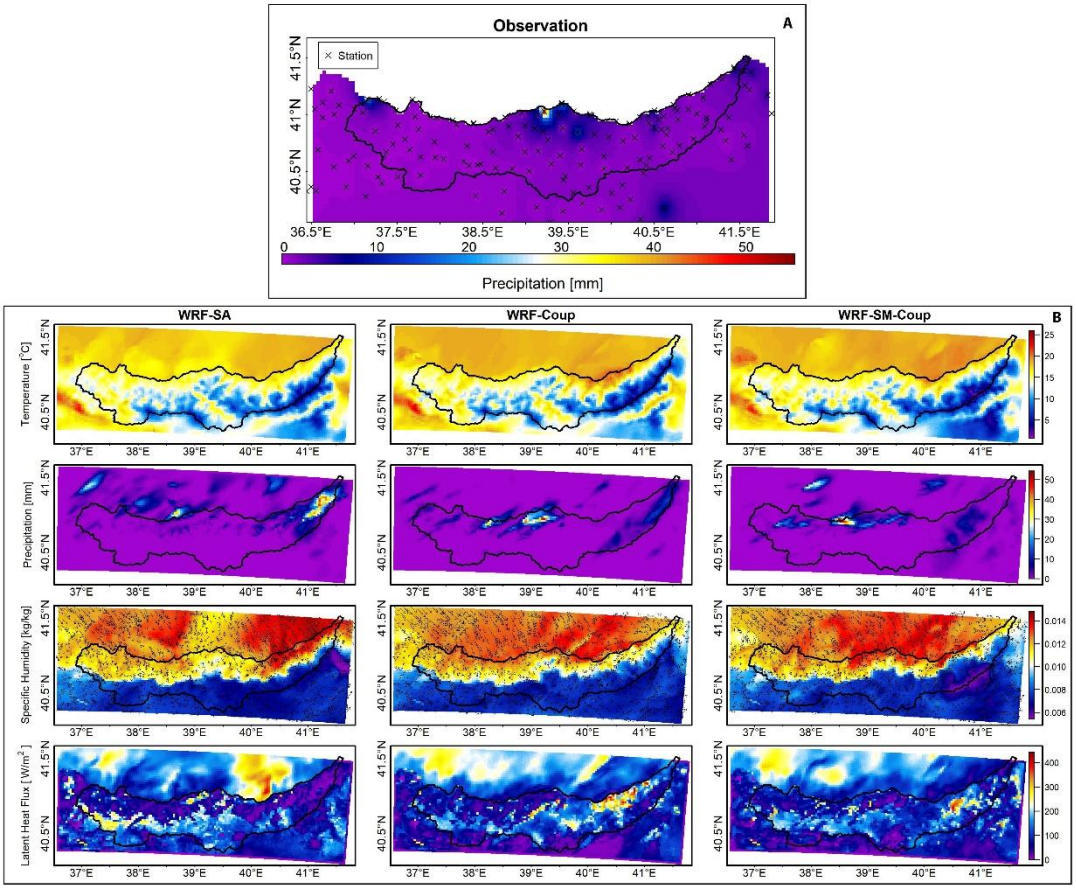

Figure 3.15. Panel A: Observed precipitation map (obtained with IDW) of the EBS region for the extreme precipitation event on 21.09.2016 at 10:00. Panel B: Temperature, precipitation, specific humidity and latent heat flux with respect to different models for the same spatiotemporal condition with Panel A. The arrows on the specific humidity maps are the vectors showing the direction and relative magnitude of the wind. The figure is obtained using R-programming language (R Core Team, 2020).

3.2.3 Long-term evaluation of hydrometeorological variables

In this study, the initial and lateral boundary conditions (i.e., wind, pressure, moisture, temperature, and geopotential height) for the WRF atmospheric models are provided by the GFS-forecast product. GFS model also forecasts precipitation by using the same initial and lateral boundary conditions. Thus, before comparatively

discussing the hydrometeorological outputs coming from WRF-SA, WRF-Coup, and WRF-SM-Coup, the precipitation output of WRF-SA is evaluated against the GFS-derived precipitation to see the possible contribution of the dynamical downscaling. Figure 3.16 shows the variation of the area-averaged precipitation from observation, GFS (0.25° spatial resolution), and WRF (3-km spatial resolution) products along the study period. The correlation coefficients between the area averaged precipitation from the observation and GFS are 0.77 and 0.90 for the EBS and MED regions. These values are 0.84 and 0.92 for the WRF outputs. In other words, especially in EBS, the WRF model improves the precipitation outputs in terms of correlation coefficients. The total precipitation amount in MED is 1342.33 mm for two years with respect to in-situ measurements. GFS overestimates the total precipitation amount (1462.44 mm), whereas WRF is relatively successful in determining this value (1319.42 mm). For EBS, total precipitation for two years is 2900.44 mm, while this value is estimated as 2570.24 mm and 2479.22 mm by the GFS and WRF models, respectively. In other words, for this region, the WRF model amplifies the underestimation amount. Still, it can be said that the WRF model improves the obtained precipitation using the GFS-derived initial and lateral boundary conditions on average as well as provides the outputs with higher resolution.

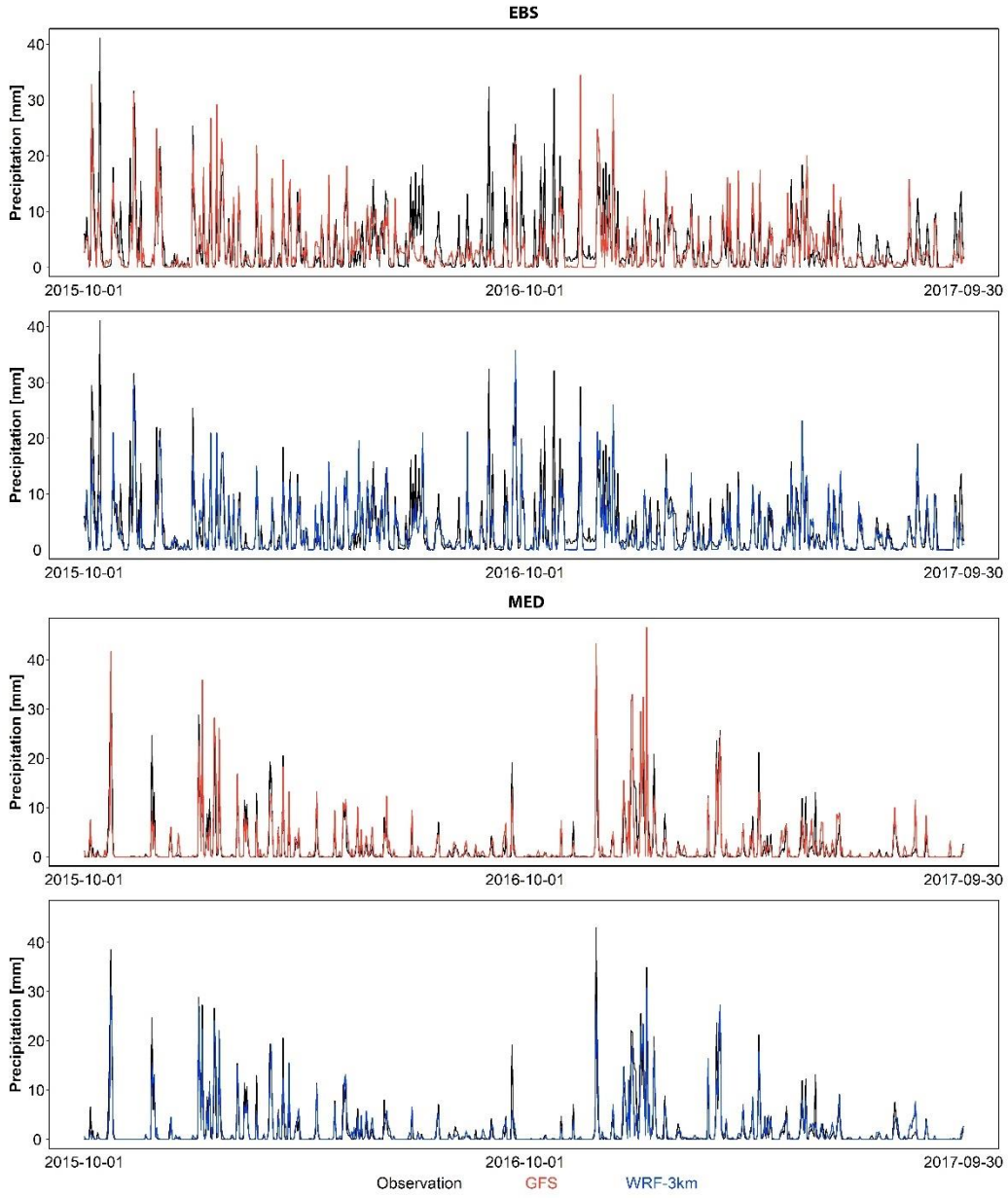

Figure 3.16. Time series of the area averaged precipitation for different products

The Arhavi, one of the subbasins in the wettest region of the country, receives precipitation in all seasons (Figure 3.17). Oymapınar has rainy winters and dry summers; thus, precipitation generally occurs in the winter months. The models can capture the mentioned precipitation behaviors of both regions that fluctuate according to the seasons. Statistics of both streamflow and precipitation data for the

WRF-Coup and WRF-SM-Coup models are almost identical for Arhavi. In other words, the sensitivity of the streamflow and the average basin precipitation outputs against changing initial soil moisture data source is minor in Arhavi, a more humid region than Oymapınar. Modifications that may alter the land-surface model outputs of the modeling system, such as running the model in fully coupled mode or updating the initial soil moisture data source, change the local water cycle and, consequently, the local precipitation formation mechanism. Local-scale atmospheric movements are more determinant on the precipitation formation processes in MED than in EBS, particularly in summer. The long-term precipitation variability of the EBS precipitation is generally shaped by the large-scale teleconnection pattern such as North Atlantic Oscillation (Türkeş and Erlat, 2003; Duzenli et al., 2018). Thus, model results more explicitly differ in Oymapınar, specifically for the spring and summer months. Moreover, the WRF-SA exaggerates the streamflow peaks in both study basins, but this feature disappeared in both coupled models. Coupled models also improve the recession parts of the streamflow graph that is highly overestimated by the WRF-SA model for the Oymapınar basin. For this basin, streamflow simulation of WRF-SM-Coup in the 2017 water year matches perfectly with observation. The relatively low streamflow simulation performance of the WRF-SM-Coup model in early 2016 most probably originates from the selection of the short spin-up period. The semi-arid region needs more spin-up time to reach an equilibrium state that contributes to simulating streamflow better. In addition, since surface soil moisture is a precipitation-dominant state variable as the region stays under semi-arid conditions (i.e., rare precipitation), the effect of updated initial soil moisture in long-term simulation becomes more significant. This, in turn, results in more appropriate exchange fluxes realistically modifying cloud-precipitation systems.

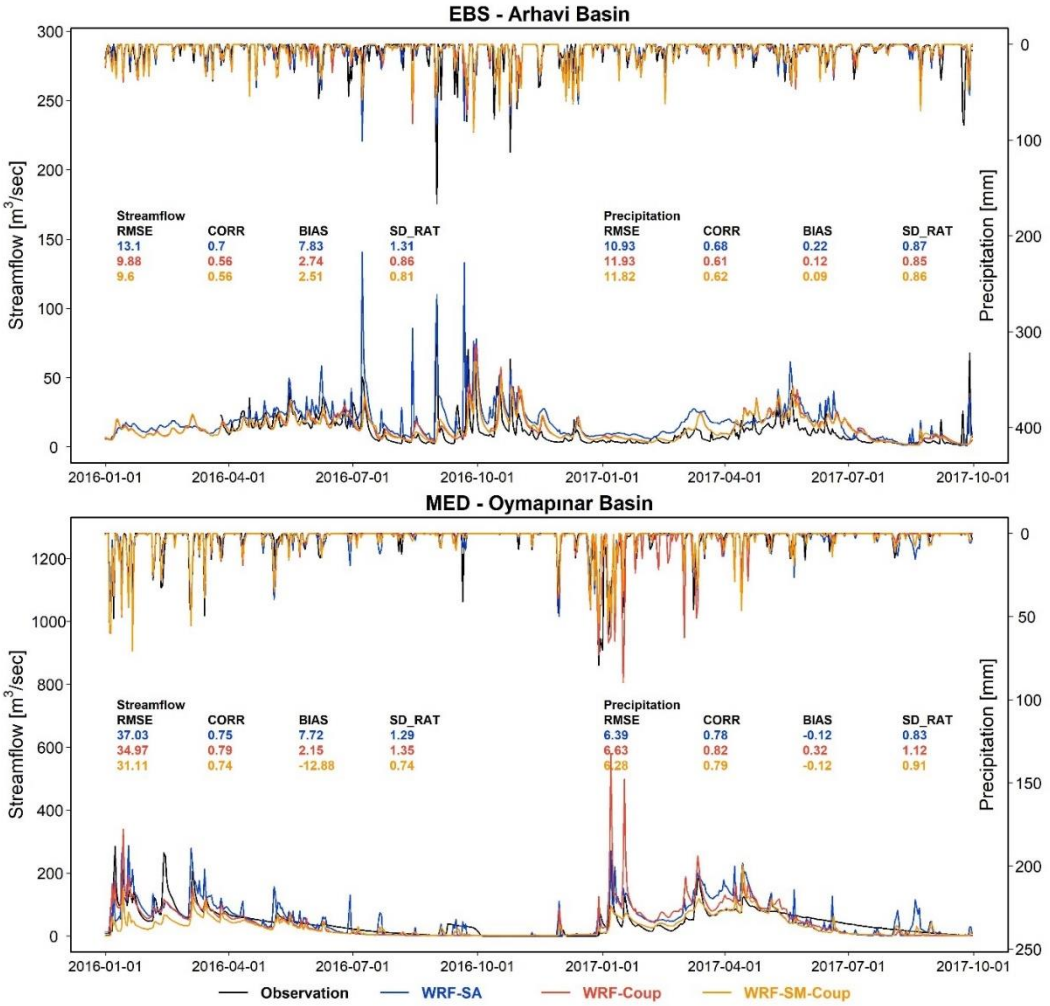

Figure 3.17. The streamflow and averaged precipitation data of the Arhavi and Oymapınar basins for the period 01.01.2016 - 01.10.2017. The time scales of the data are daily. The reverse axes show the precipitation time series. The figure is obtained using R-programming language (R Core Team, 2020).

Figure 3.18 shows the spatial distribution of the RMSE and correlation statistics for precipitation and temperature covering the period of 01.01.2016 - 01.10.2017. For the EBS region, the primary difference in the outputs occurs over the coastal area in the northeastern part of the region. The WRF-SA model provides higher correlation values over this region, albeit the RMSE values are similar. Coupled models do not develop the outputs in that region, probably because the interannual precipitation is highly connected to the instabilities arising at the sea surface rather than the land

surface (Senatore et al., 2020). Unlike precipitation, the coupled models provide more successful outcomes for the temperature of EBS, which highly depends on the Bowen ratio (sensible to latent heat fluxes ratio). Besides, the satellite soil moisture usage thoroughly contributes to the precipitation outputs in interior parts of the southeastern MED region. The topsoil layer moisture is one of the fundamental moisture sources of precipitation since the region is located on the inland side of the mountains. Thus, the output precipitation from the model gives a reaction to any variation done on the soil moisture initiation. For this case, even though the WRF-Coup model does not improve the WRF-SA precipitation, the WRF-Coup-SM, namely the SMAP data, significantly enhances the precipitation. The temperature outputs of the WRF-SA and WRF-Coup-SM models in MED are also more realistic based on the statistical distribution maps.

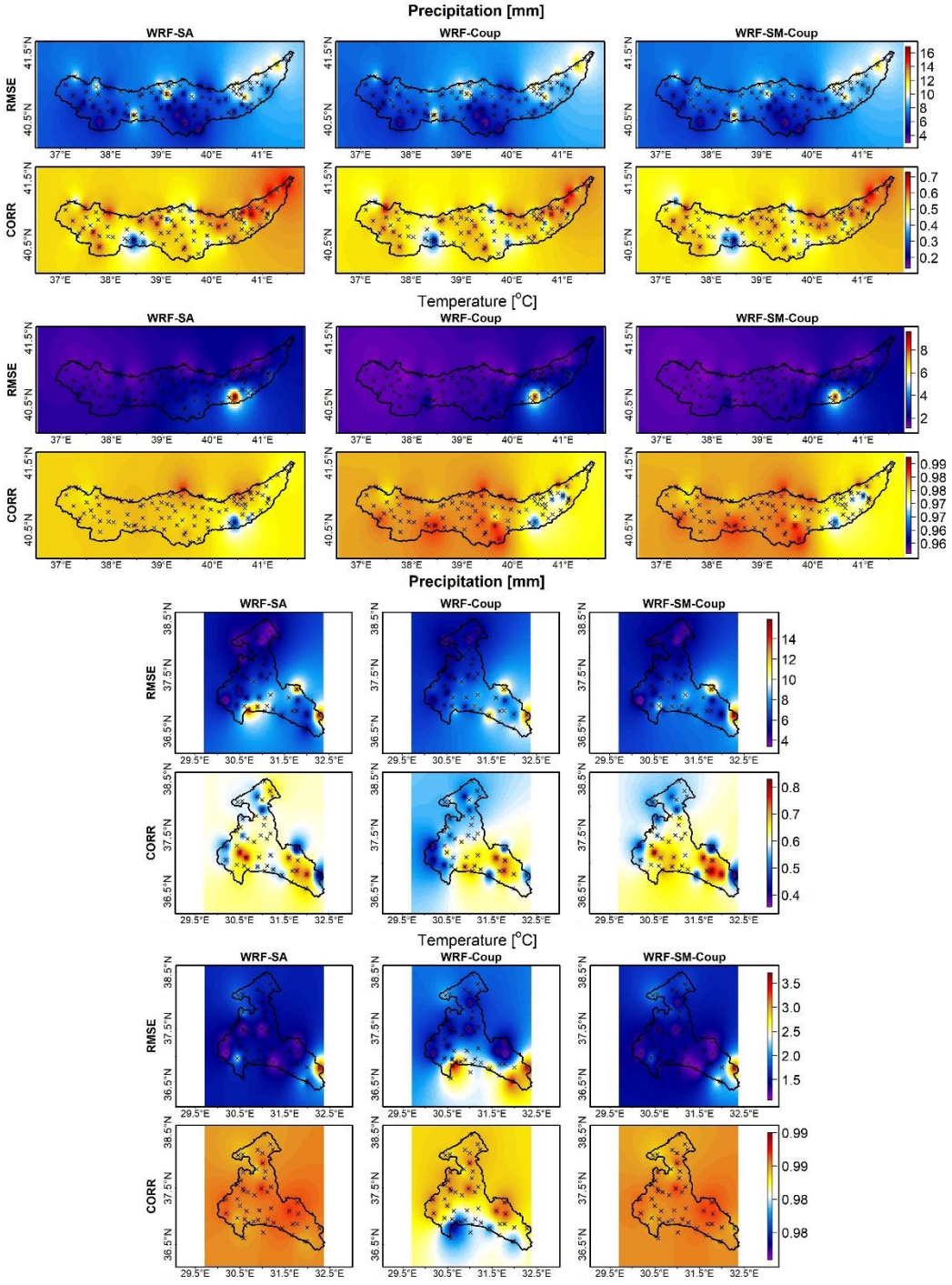

Figure 3.18. Spatial distribution of the statistics calculated between each meteorological station and the closest grid for the daily time series including 01.01.2016 - 01.10.2017. The statistics are interpolated to entire study are via the IDW method. The figure is obtained using R-programming language (R Core Team, 2020).

Figure 3.19 shows the monthly water budget distribution of the models considering two flood-prone subbasins of EBS (i.e., Arhavi) and MED (i.e., Kemer). Negligibly small residual values prove that the water balance closure is successfully maintained in both regions. For the EBS region, snowfall in winter is a crucial element of the water budget distribution in spring. Thus, the water distribution of EBS is provided, including the winter months. In EBS, the snowpacks formed in December and January start melting in March and contribute to the (sub)surface runoff until June (even July for the coupled models). The total streamflow is mainly contributed by the underground runoff (i.e., UR; moisture–driven mechanism) for all models of the EBS region. Coupled models yield more snowmelt than the standalone WRF in spring, so their interflow contribution is higher. Summer increase (decrease) in ET (precipitation) and winter increase (decrease) in precipitation (ET) exist as some seasonal character of the water cycle. Given the highly elevated terrain of the Arhavi basin, the infiltrated water is widely distributed to the lower elevations via the subsurface routing option of the coupled models. This lets the existing soil stay unsaturated and continue infiltrating along the region, increasing the groundwater flow (Senatore et al., 2015; Arnault et al., 2016; Fersch et al., 2020). On the other hand, in Kemer, both coupled models substantially reduce the precipitation amount simulated by WRF-SA. This signifies the critical influence of surface energy exchanges generated by coupled models under semi-arid climate conditions. After June, the ET losses of coupled models are solely driven by soil moisture, which further increases the soil moisture deficit. Higher infiltration as a result of increased soil moisture deficit causes streamflow contributed largely by interflow while precipitation occurs during spring. Besides, from May through September, particularly in August, WRF-SM-Coup yields greater precipitation than the WRF-Coup, addressing the effect of redistribution of initial soil moisture. Nevertheless, the soil moisture update does not significantly affect the water budget distribution in the humid Arhavi basin.

Furthermore, Fersch et al. (2020) define some residuals in terrestrial water balance outputs of both standalone and coupled models due to the numerical errors and

subgrid aggregation/disaggregation processes of the coupled models. For our case, the residual amounts for the water balances of standalone models are almost zero. The residuals are higher in percentage in the semi-arid region (i.e., MED) than in the humid region (i.e., EBS) for the coupled models.

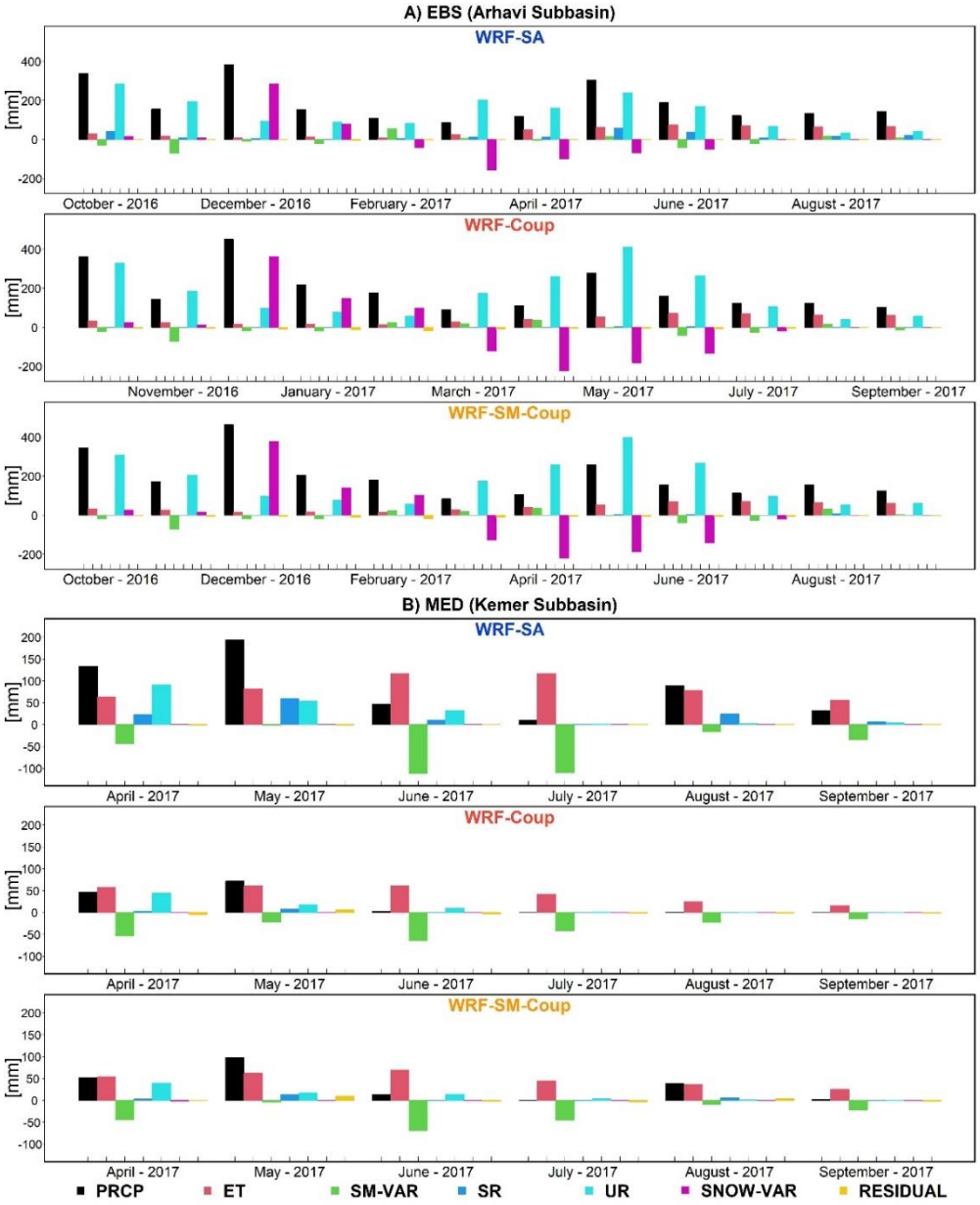

Figure 3.19. Water budget distribution for different model cases over Arhavi (Basin 1 on Figure 2-A) and Kemer (Basin 4 on Figure 2C) subbasins. Subbasins are numbered starting from the eastern-based on Figure 2-A for EBS and Figure 2-C for MED. PRCP= ET + SM-VAR + SR + UR + SNOW-VAR + RESIDUAL; where, PRCP: Precipitation, ET: Evapotranspiration, SM-VAR: Soil moisture storage variation, SR: Surface runoff, UR: Underground runoff, SNOW-VAR: Snow-water equivalent depth variation. The figure is obtained using R-programming language (R Core Team, 2020).

CHAPTER 4

CONCLUSIONS

This study consists of two different parts. In the first part, a sensitivity analysis is conducted on the model physics, initial and lateral boundary data source, and horizontal grid spacing of the WRF model to improve extreme precipitation simulation capacity. The primary aim here is to construct early warning systems against extreme precipitation events over two flood-prone regions of Turkey (i.e., EBS and MED) and discuss the model behavior in different simulation conditions. In the second part, the atmospheric model is coupled with a hydrologic model, WRF-Hydro, to enhance the feedback mechanism between the land and the overlying atmosphere. Before coupling the WRF and WRF-Hydro models, some essential parameters of the WRF-Hydro are calibrated. The coupled model is also initiated with the soil moisture data retrieved from the SMAP source. The influences of the coupling and soil moisture data update on the land surface energy fluxes, and accordingly, the modeling system outputs are discussed. The outcomes of the study are provided in the following sections.

4.1 Sensitivity of the extreme precipitation simulation capability of the WRF model against model physics and initial and lateral boundary data source

According to the TOPSIS results, the ERA5 improves the WRF-derived precipitation performance more than GFS when it is used as initial and lateral boundary conditions in the EBS region. The GFS is a better data source for the simulations of the MED-summer event. Various members initiated with GFS and ERA5 do appear among the best scenarios of the MED-autumn event. The MYJ governs the PBL option of the EBS-summer event. Yet, for the other events, it is not possible to identify a dominant

PBL choice. The TOPSIS algorithm commonly proposes the combinations containing WSM6 as the MP option for the EBS-autumn event, while it recommends ES for the MED-autumn event. Also, the combinations of these MP schemes with the CU scheme of GFES improves the results. AATS is the most prevailing MP scheme for the MED-summer event simulations that have a 3 km grid spacing. Albeit most of the top ten scenarios based on ranking applied over 96 scenarios (two nest domains used together) have a spatial resolution of 9 km for the events, the model is also successful in downscaling precipitation values to the 3 km spatial resolution. For instance, five of the best ten scenarios of the MED-autumn event comprise 3 km horizontal grid spacing. For the CU parameterization, the BMJ option is more influential in summer months, whereas KF is more active in autumn. It can be encountered with the GFES option in the best scenarios of both seasons. Another robust conclusion is that physics combinations used in ensemble members 18, 20, 22, 42 for EBS and ensemble members 18, 27, 33, 37 for MED should be avoided.

Based on the analyses performed in this study, the precipitation variability is more sensitive to the model parameterization than the initial and lateral boundary data source selection for the area-averaged precipitation. Still, this conclusion might be case specific. In future studies, rechecking this result via larger ensembles, including more initial and lateral boundary condition data sources and various extreme precipitation events with different characteristics, would be beneficial.

For the calibration events, the ensemble means underestimate the area-averaged precipitation except for the MED-autumn event. For the simulation period of this event, not only the ensemble mean but also all of the scenarios overestimate the amount of precipitation. This situation might originate from the biased SST data or excessive local soil moisture evaporation during the simulations. Accordingly, testing the sensitivity of the WRF-derived precipitation against different SST and soil moisture data sources over MED would be a good contribution to the existing literature. Still, the WRF (3 km) ensemble is more successful than the ERA5 (0.25°) in simulating the validation event for the MED-Autumn. This is one of the essential contributions of this study because MED is a region considered a climate change

hotspot, so better simulation of the extreme events over this region is crucial. Moreover, the model for the EBS-summer validation event almost perfectly predicts the total precipitation amount. The validation ensemble overestimates the occurred total precipitation by only 3%. Estimating the total amount of a summer event with an error of 3% is quite valuable.

It is unquestionable that finding the best model physics combination together with representative grid resolving and accurate initial and lateral boundary datasets is of primary importance in weather prediction efforts. Further work under-way includes repeating this analysis on additional geographical regions using higher number of events in Turkey to release more comprehensive evaluation and addressed model combinations throughout the country.

4.2 Contribution of the WRF & WRF-Hydro coupling and satellite soil moisture initialization to the accuracy of hydrometeorological forecasts

The WRF-Hydro-SA model is calibrated using the in-situ measurements as precipitation input for a long-term period that includes the seasons. It is validated for different spatiotemporal conditions considering each of the WRF and (un)corrected radar precipitation, as well as the in-situ measurements. The model is calibrated based on both KGE and NSE statistics using daily streamflow for MED and daily and hourly streamflow observations using KGE function for EBS. According to the results, the best parameter values differ notably in the KGE- and NSE-based calibration, although the model is calibrated along the same period. The essential difference between the two calibration functions arises because the KGE coefficient is mainly driven by the bias component of the runoff obtained in this study. As a result of this tendency, the KGE-based calibration chooses the parameter values providing better biases but worse MAE, R, and RMSE values. Similarly, the selected parameter values vary at the end of the daily and hourly streamflow-based calibration. The hourly calibration ends with less rough channel surface, higher infiltration, and lower groundwater recharge, causing higher soil moisture volume.

The highly elevated terrain and small basins of EBS trigger different model construction in hourly precision. This information is valuable for the early warning system studies over the basins showing fast hydrologic response as a result of a complex topography and prone to flash floods.

The worse performance measures obtained for the validation periods are partly related to a systematic error in the WRF temperature variable given as input data to the WRF-Hydro-SA model, which induces confusion in the model when partitioning the input precipitation as rainfall or snow. Accordingly, the model fails to successfully distribute the total runoff budget throughout the time series since it could not define the snowpacks and melting periods correctly. In spite of the availability of the spatiotemporal changes in different precipitation forcings (i.e., radar, WRF, in-situ), winter snow accumulation significantly controls the streamflow. The model is forced with the observed temperature to overcome this issue. Even though this process improves the outcomes, there are still undisclosed points waiting to be explored. In future works, merging the temperature data taken from different sources such as remote sensing tools, models, and in-situ measurements, via innovative ensemble techniques to provide high-quality temperature input to the hydrologic model or coupling the model with a state-of-the-art snow module would make an excellent contribution to this field of work.

Hydrometeorological variables obtained from the long-term simulations of the WRF-SA, WRF-Coup, and WRF-Coup-SM models are evaluated for long-term and short-term periods. As a result, coupling WRF/WRF-Hydro modeling system causes higher underground runoff and soil moisture outputs, whereas coupling induces lower surface runoff volume, especially in EBS (i.e., highly elevated and steep-sided basin). Besides, the lateral distribution of the water budget in coupled model positively contributes to the convection-driven extreme precipitation simulation for the EBS region. Based on this result, using the coupled systems for early warning purposes is quite beneficial, especially for the summer extremes of humid regions having complex topography.

The initiation of the model with the satellite soil moisture affects the outputs more explicitly in the MED region than in the EBS region. Soil moisture update has a negligible effect on long-term precipitation outputs in the more humid region, in which precipitation is mainly driven by large-scale circulations instead of local convection. However, the SMAP data usage to initiate the coupled model upgrades the temperature outputs for the regions by sharing the total energy between latent and sensible heat fluxes more accurately. With a better representation of exchange fluxes provided by initial satellite soil moisture update in long-term simulation, simulated streamflow matches perfectly with observation. For future studies, coupling and soil moisture update contribution can be measured over the interior regions, where the continental climate is dominant, to compare the outcomes with the coastal regions. Likewise, testing the soil moisture initiation with different spin-up periods and with respect to various data sources would form an ensemble including helpful information about the terrestrial water cycle components and their interactions.

REFERENCES

Abbaszadeh, P., Gavahi, K., & Moradkhani, H. (2020). Multivariate remotely sensed and in-situ data assimilation for enhancing community WRF-Hydro model forecasting. *Advances in Water Resources*, *145*, 103721. https://doi.org/10.1016/j.advwatres.2020.103721

Afshar, M.H., Bulut, B., Duzenli, E., Amjad, M., & Yilmaz, M. T. (2022). Global spatiotemporal consistency between meteorological and soil moisture drought indices. *Agricultural and Forest Meteorology*, *316*, 108848. https://doi.org/10.1016/j.agrformet.2022.108848

Afshar, M.H., & Yilmaz, M. T. (2017). The added utility of nonlinear methods compared to linear methods in rescaling soil moisture products. *Remote Sensing of Environment*, *196*, 224–237. https://doi.org/10.1016/j.rse.2017.05.017

Afshar, Mehdi H., Şorman, A. Ü., Tosunoğlu, F., Bulut, B., Yilmaz, M. T., & Danandeh Mehr, A. (2020). Climate change impact assessment on mild and extreme drought events using copulas over Ankara, Turkey. *Theoretical and Applied Climatology*. https://doi.org/10.1007/s00704-020-03257-6

Ali, H., & Mishra, V. (2018). Increase in Subdaily Precipitation Extremes in India Under 1.5 and 2.0 °C Warming Worlds. *Geophysical Research Letters*, *45*(14), 6972–6982. https://doi.org/10.1029/2018GL078689

Amjad, M., Yilmaz, M. T., Yucel, I., & Yilmaz, K. K. (2020). Performance evaluation of satellite- and model-based precipitation products over varying climate and complex topography. *Journal of Hydrology*, *584*, 124707. https://doi.org/10.1016/j.jhydrol.2020.124707

Argüeso, D., Hidalgo-Muñoz, J. M., Gámiz-Fortis, S. R., Esteban-Parra, M. J., Dudhia, J., & Castro-Díez, Y. (2011). Evaluation of WRF Parameterizations for Climate Studies over Southern Spain Using a Multistep Regionalization. *Journal of Climate*, *24*(21), 5633–5651. https://doi.org/10.1175/JCLI-D-11-00073.1

Arnault, J., Rummler, T., Baur, F., Lerch, S., Wagner, S., Fersch, B., Zhang, Z., Kerandi, N., Keil, C., & Kunstmann, H. (2018). Precipitation Sensitivity to the Uncertainty of Terrestrial Water Flow in WRF-Hydro: An Ensemble Analysis for Central Europe. *Journal of Hydrometeorology*, *19*(6), 1007–1025. https://doi.org/10.1175/JHM-D-17-0042.1

Arnault, J., Wagner, S., Rummler, T., Fersch, B., Bliefernicht, J., Andresen, S., & Kunstmann, H. (2016). Role of Runoff–Infiltration Partitioning and Resolved Overland Flow on Land–Atmosphere Feedbacks: A Case Study with the WRF-Hydro Coupled Modeling System for West Africa. *Journal of Hydrometeorology*, *17*(5), 1489–1516. https://doi.org/10.1175/JHM-D-15-0089.1

Arnault, J., Wei, J., Rummler, T., Fersch, B., Zhang, Z., Jung, G., Wagner, S., & Kunstmann, H. (2019). A Joint Soil-Vegetation-Atmospheric Water Tagging Procedure With WRF-Hydro: Implementation and Application to the Case of Precipitation Partitioning in the Upper Danube River Basin. *Water Resources Research*, *55*(7), 6217–6243. https://doi.org/10.1029/2019WR024780

Berg, P., Christensen, O. B., Klehmet, K., Lenderink, G., Olsson, J., Teichmann, C., & Yang, W. (2018). Summertime precipitation extremes in a EURO-CORDEX 0.11◦ ensemble at an hourly resolution. *Natural Hazards and Earth System Sciences Discussions*, 1–21. https://doi.org/10.5194/nhess-2018-362

Bulut, B., Yılmaz, M. T., Afshar, M. H., Şorman, A. Ü., Yücel, İ., Cosh, M. H., & Şimşek, O. (2019). Evaluation of Remotely-Sensed and Model-Based Soil Moisture Products According to Different Soil Type, Vegetation Cover and Climate Regime Using Station-Based Observations over Turkey. *Remote Sensing*, *11*(16), 1875. https://doi.org/10.3390/rs11161875

Camera, C., Bruggeman, A., Zittis, G., Sofokleous, I., & Arnault, J. (2020). Simulation of extreme rainfall and streamflow events in small Mediterranean watersheds with a one-way-coupled atmospheric–hydrologic modelling system. *Natural Hazards and Earth System Sciences*, *20*(10), 2791–2810.

https://doi.org/10.5194/nhess-20-2791-2020

Cassola, F., Ferrari, F., & Mazzino, A. (2015). Numerical simulations of Mediterranean heavy precipitation events with the WRF model: A verification exercise using different approaches. *Atmospheric Research*, *164*, 210–225. https://doi.org/10.1016/j.atmosres.2015.05.010

Cerbelaud, A., Lefèvre, J., Genthon, P., & Menkes, C. (2022). Assessment of the WRF-Hydro uncoupled hydro-meteorological model on flashy watersheds of the Grande Terre tropical island of New Caledonia (South-West Pacific). *Journal of Hydrology: Regional Studies*, *40*, 101003. https://doi.org/https://doi.org/10.1016/j.ejrh.2022.101003

Chen, F., & Dudhia, J. (2001). Coupling an Advanced Land Surface–Hydrology Model with the Penn State–NCAR MM5 Modeling System. Part I: Model Implementation and Sensitivity. *Monthly Weather Review*, *129*(4), 569–585. https://doi.org/10.1175/1520-0493(2001)129<0569:CAALSH>2.0.CO;2

Di, Z., Duan, Q., Gong, W., Wang, C., Gan, Y., Quan, J., Li, J., Miao, C., Ye, A., & Tong, C. (2015). *Assessing WRF model parameter sensitivity: A case study with 5 day summer precipitation forecasting in the Greater Beijing Area*. *42*(2), 579–587.

Dillon, M. E., Collini, E. A., & Ferreira, L. J. (2016). Sensitivity of WRF short-term forecasts to different soil moisture initializations from the GLDAS database over South America in March 2009. *Atmospheric Research*, *167*, 196–207. https://doi.org/10.1016/j.atmosres.2015.07.022

Dirmeyer, P. A., Guo, Z., & Gao, X. (2004). Comparison, validation, and transferability of eight multiyear global soil wetness products. *Journal of Hydrometeorology*, *5*(6), 1011–1033.

Done, J., Davis, C. A., & Weisman, M. (2004). The next generation of NWP: Explicit forecasts of convection using the weather research and forecasting (WRF) model. *Atmospheric Science Letters*, *5*(6), 110–117. https://doi.org/10.1002/asl.72

Dudhia, J. (2014). Overview of WRF physics. *University Corporation for Atmospheric Research, Boulder, CO, Http://Www2. Mmm. Ucar. Edu/Wrf/Users/Tutorial/201401/Physics_full. Pdf*.

Duzenli, E., Tabari, H., Willems, P., & Yilmaz, M. T. (2018). Decadal variability analysis of extreme precipitation in Turkey and its relationship with teleconnection patterns. *Hydrological Processes*, *32*(23), 3513–3528. https://doi.org/10.1002/hyp.13275

Duzenli, E., Yucel, I., Pilatin, H., & Yilmaz, M. T. (2021). Evaluating the performance of a WRF initial and physics ensemble over Eastern Black Sea and Mediterranean regions in Turkey. *Atmospheric Research*, *248*, 105184. https://doi.org/10.1016/j.atmosres.2020.105184

Dyer, J., Zarzar, C., Amburn, P., Dumais, R., Raby, J., & Smith, J. A. (2016). Defining the Influence of Horizontal Grid Spacing on Ensemble Uncertainty within a Regional Modeling Framework. *Weather and Forecasting*, *31*(6), 1997–2017. https://doi.org/10.1175/waf-d-16-0030.1

Efstathiou, G. A., Zoumakis, N. M., Melas, D., Lolis, C. J., & Kassomenos, P. (2013). Sensitivity of WRF to boundary layer parameterizations in simulating a heavy rainfall event using different microphysical schemes. Effect on large-scale processes. *Atmospheric Research*, *132*, 125–143. https://doi.org/10.1016/j.atmosres.2013.05.004

Ekström, M., & Gilleland, E. (2017). Assessing convection permitting resolutions of WRF for the purpose of water resource impact assessment and vulnerability work: A southeast Australian case study. *Water Resources Research*, *53*(1), 726–743. https://doi.org/10.1002/2016WR019545

ElTahan, M., & Magooda, M. (2017). Evaluation of different WRF microphysics schemes: severe rainfall over Egypt case study. *ArXiv Preprint ArXiv:1711.04163*.

Evans, J. P., Ekström, M., & Ji, F. (2012). Evaluating the performance of a WRF physics ensemble over South-East Australia. *Climate Dynamics*, *39*(6), 1241–

1258. https://doi.org/10.1007/s00382-011-1244-5

Ferrier, B. S., Jin, Y., Lin, Y., Black, T., Rogers, E., & DiMego, G. (2002). Implementation of a new grid-scale cloud and precipitation scheme in the NCEP Eta model. *Conference on Weather Analysis and Forecasting*, *19*, 280–283.

Fersch, B., Senatore, A., Adler, B., Arnault, J., Mauder, M., Schneider, K., Völksch, I., & Kunstmann, H. (2020). High-resolution fully coupled atmospheric–hydrological modeling: a cross-compartment regional water and energy cycle evaluation. *Hydrology and Earth System Sciences*, *24*(5), 2457–2481. https://doi.org/10.5194/hess-24-2457-2020

Fosser, G., Khodayar, S., & Berg, P. (2015). Benefit of convection permitting climate model simulations in the representation of convective precipitation. *Climate Dynamics*, *44*(1–2), 45–60. https://doi.org/10.1007/s00382-014-2242-1

Friedman, J. H. (1991). Multivariate adaptive regression splines. *The Annals of Statistics*, *19*(1), 1–67. https://doi.org/10.1214/aos/1176347963

Gao, S., Huang, D., Du, N., Ren, C., & Yu, H. (2022). WRF ensemble dynamical downscaling of precipitation over China using different cumulus convective schemes. *Atmospheric Research*, *271*, 106116. https://doi.org/10.1016/j.atmosres.2022.106116

García-Díez, M., Fernández, J., Fita, L., & Yagüe, C. (2013). Seasonal dependence of WRF model biases and sensitivity to PBL schemes over Europe. *Quarterly Journal of the Royal Meteorological Society*, *139*(671), 501–514. https://doi.org/10.1002/qj.1976

Givati, A., Gochis, D., Rummler, T., & Kunstmann, H. (2016). Comparing one-way and two-way coupled hydrometeorological forecasting systems for flood forecasting in the mediterranean region. *Hydrology*, *3*(2). https://doi.org/10.3390/hydrology3020019

Givati, A., & Rosenfeld, D. (2013). The Arctic Oscillation, climate change and the effects on precipitation in Israel. *Atmospheric Research*, *132*, 114–124. https://doi.org/10.1016/j.atmosres.2013.05.001

Gochis, D., & Chen, F. (2003). Hydrological enhancements to the community Noah land surface model. *NCAR Scientific Technical Report*, 77. https://doi.org/10.5065/D60P0X00

Gochis, D. J., Dugger, A., Barlage, M., Fitzgerald, K., Karsten, L., McAllister, M., McCreight, J., Mills, J., Rafieeinasab, A., & Read, L. (2018). *The NCAR WRF-Hydro Modeling System Technical Description*.

Grell, G. A., & Dévényi, D. (2002). A generalized approach to parameterizing convection combining ensemble and data assimilation techniques. *Geophysical Research Letters*, *29*(14), 38–1. https://doi.org/10.1029/2002gl015311

Grell, G. A., & Freitas, S. R. (2013). A scale and aerosol aware convective parameterization. *Atmos. Chem. Phys*, *14*(10), 5233–5250. https://doi.org/10.5194/acpd-13-23845-2013

Gupta, H. V, Kling, H., Yilmaz, K. K., & Martinez, G. F. (2009). Decomposition of the mean squared error and NSE performance criteria: Implications for improving hydrological modelling. *Journal of Hydrology*, *377*(1–2), 80–91. https://doi.org/10.1016/j.jhydrol.2009.08.003

Gustafson Jr., W. I., Ma, P.-L., & Singh, B. (2014). Precipitation characteristics of CAM5 physics at mesoscale resolution during MC3E and the impact of convective timescale choice. *Journal of Advances in Modeling Earth Systems*, *6*(4), 1271–1287.

Hong, S.-Y., & Lim, J. O. J. (2006). The WRF single-moment 6-class microphysics scheme (WSM6). *Asia-Pacific Journal of Atmospheric Sciences*, *42*(2), 129–151.

Hong, S., Lakshmi, V., Small, E. E., Chen, F., Tewari, M., & Manning, K. W. (2009). Effects of vegetation and soil moisture on the simulated land surface processes

from the coupled WRF/Noah model. *Journal of Geophysical Research*, *114*(D18), D18118. https://doi.org/10.1029/2008JD011249

Houtekamer, P. L., Lefaivre, L., Derome, J., Ritchie, H., & Mitchell, H. L. (1996). A system simulation approach to ensemble prediction. *Monthly Weather Review*, *124*(6), 1225–1242. https://doi.org/10.1175/1520-0493(1996)124<1225:ASSATE>2.0.CO;2

Hsiao, L. F., Yang, M. J., Lee, C. S., Kuo, H. C., Shih, D. S., Tsai, C. C., Wang, C. J., Chang, L. Y., Chen, D. Y. C., Feng, L., Hong, J. S., Fong, C. T., Chen, D. S., Yeh, T. C., Huang, C. Y., Guo, W. D., & Lin, G. F. (2013). Ensemble forecasting of typhoon rainfall and floods over a mountainous watershed in Taiwan. *Journal of Hydrology*, *506*, 55–68. https://doi.org/10.1016/j.jhydrol.2013.08.046

Hu, X. M., Nielsen-Gammon, J. W., & Zhang, F. (2010). Evaluation of three planetary boundary layer schemes in the WRF model. *Journal of Applied Meteorology and Climatology*, *49*(9), 1831–1844. https://doi.org/10.1175/2010JAMC2432.1

Hwang, C. L., & Yoon, K. (1981). *Multiple Attribute Decision Making: Methods and Applications*. Springer.

Janjić, Z. I. (1994). The step-mountain eta coordinate model: Further developments of the convection, viscous sublayer, and turbulence closure schemes. *Monthly Weather Review*, *122*(5), 927–945.

Kain, J. S. (2004). The Kain–Fritsch convective parameterization: an update. *Journal of Applied Meteorology*, *43*(1), 170–181. https://doi.org/10.1175/1520-0450(2004)043<0170:TKCPAU>2.0.CO;2

Kan, Y., Liu, C., Liu, Y., & Zhou, C. (2015). Evaluation of WRF microphysics and cumulus parameterization schemes in simulating a heavy rainfall event over Yangtze River delta. *Remote Sensing and Modeling of Ecosystems for Sustainability XII*, *9610*, 96100R.

Kerandi, N., Arnault, J., Laux, P., Wagner, S., Kitheka, J., & Kunstmann, H. (2018). Joint atmospheric-terrestrial water balances for East Africa: a WRF-Hydro case study for the upper Tana River basin. *Theoretical and Applied Climatology*, *131*(3–4), 1337–1355. https://doi.org/10.1007/s00704-017-2050-8

Kessler, E. (1995). On the continuity and distribution of water substance in atmospheric circulations. *Atmospheric Research*, *38*(1–4), 109–145.

Kilicarslan, B. M., Yucel, I., Pilatin, H., Duzenli, E., & Yilmaz, M. T. (2021). Improving WRF-Hydro runoff simulations of heavy floods through the sea surface temperature fields with higher spatio-temporal resolution. *Hydrological Processes*, *35*(9), e14338. https://doi.org/10.1002/hyp.14338

Lahmers, T. M., Castro, C. L., & Hazenberg, P. (2020). Effects of Lateral Flow on the Convective Environment in a Coupled Hydrometeorological Modeling System in a Semiarid Environment. *Journal of Hydrometeorology*, *21*(4), 615–642. https://doi.org/10.1175/JHM-D-19-0100.1

Li, F., Rosa, D., Collins, W. D., & Wehner, M. F. (2012). Super-parameterization: A better way to simulate regional extreme precipitation. *Journal of Advances in Modeling Earth Systems*, *4*(2). https://doi.org/10.1029/2011MS000106

Li, Y., Li, Z., Zhang, Z., Chen, L., Kurkute, S., Scaff, L., & Pan, X. (2019). High-Resolution Regional Climate Modeling and Projection over Western Canada using a Weather Research Forecasting Model with a Pseudo-Global Warming Approach. *Hydrology and Earth System Sciences Discussions*, *23*(11), 4635–4659. https://doi.org/10.5194/hess-2019-201

Lin, L.-F., & Pu, Z. (2019). Examining the Impact of SMAP Soil Moisture Retrievals on Short-Range Weather Prediction under Weakly and Strongly Coupled Data Assimilation with WRF-Noah. *Monthly Weather Review*, *147*(12), 4345–4366. https://doi.org/10.1175/MWR-D-19-0017.1

Liu, J., Bray, M., & Han, D. (2012). Sensitivity of the Weather Research and Forecasting (WRF) model to downscaling ratios and storm types in rainfall simulation. *Hydrological Processes*, *26*(20), 3012–3031.

https://doi.org/10.1002/hyp.8247

Mannan, M. A., Chowdhury, M. A. M., & Karmakar, S. (2013). Application of NWP model in prediction of heavy rainfall in Bangladesh. *Procedia Engineering*, *56*, 667–675. https://doi.org/10.1016/j.proeng.2013.03.176

Mielikainen, J., Huang, B., Wang, J., Allen Huang, H. L., & Goldberg, M. D. (2013). Compute unified device architecture (CUDA)-based parallelization of WRF Kessler cloud microphysics scheme. *Computers and Geosciences*, *52*, 292–299. https://doi.org/10.1016/j.cageo.2012.10.006

Mylonas, M. P., Douvis, K. C., Polychroni, I. D., Politi, N., & Nastos, P. T. (2019). Analysis of a Mediterranean Tropical-Like Cyclone. Sensitivity to WRF Parameterizations and Horizontal Resolution. *Atmosphere*, *10*(8), 425. https://doi.org/10.3390/atmos10080425

Naabil, E., Lamptey, B. ., Arnault, J., Olufayo, A., & Kunstmann, H. (2017). Water resources management using the WRF-Hydro modelling system: Case-study of the Tono dam in West Africa. *Journal of Hydrology: Regional Studies*, *12*, 196–209. https://doi.org/10.1016/j.ejrh.2017.05.010

Nash, J. E., & Sutcliffe, J. V. (1970). River flow forecasting through conceptual models part I — A discussion of principles. *Journal of Hydrology*, *10*(3), 282–290. https://doi.org/10.1016/0022-1694(70)90255-6

Ning, L., Zhan, C., Luo, Y., Wang, Y., & Liu, L. (2019). A review of fully coupled atmosphere-hydrology simulations. *Journal of Geographical Sciences*, *29*(3), 465–479. https://doi.org/10.1007/s11442-019-1610-5

NOAA. (2015). *NCEP GFS 0.25 Degree Global Forecast Grids Historical Archive*. Research Data Archive at the National Center for Atmospheric Research, Computational and Information Systems Laboratory. https://doi.org/10.5065/D65D8PWK

Pennelly, C., Reuter, G., & Flesch, T. (2014). Verification of the WRF model for simulating heavy precipitation in Alberta. *Atmospheric Research*, *135–136*,

172–192. https://doi.org/10.1016/j.atmosres.2013.09.004

Pielke Sr, R. A., Beltrán-Przekurat, A., Hiemstra, C. A., Lin, J., Nobis, T. E., Adegoke, J., Nair, U. S., & Niyogi, D. (2006). Impacts of regional land use and land cover on rainfall: an overview. *Climate Variability and Change: Hydrological Impacts*, 325–331.

Pilatin, H., Yucel, I., Duzenli, E., & Yilmaz, M. T. (2021). Sensitivity of WRF-derived hydrometeorological extremes to sea surface temperatures in regions with complex topography and diverse climate. *Atmospheric Research*, *264*, 105816. https://doi.org/10.1016/j.atmosres.2021.105816

Prein, A. F., Langhans, W., Fosser, G., Ferrone, A., Ban, N., Goergen, K., Keller, M., Tölle, M., Gutjahr, O., Feser, F., Brisson, E., Kollet, S., Schmidli, J., Van Lipzig, N. P. M., & Leung, R. (2015). A review on regional convection-permitting climate modeling: Demonstrations, prospects, and challenges. *Reviews of Geophysics*, *53*(2), 323–361. https://doi.org/10.1002/2014RG000475

Prein, A. F., Rasmussen, R. M., Ikeda, K., Liu, C., Clark, M. P., & Holland, G. J. (2017). The future intensification of hourly precipitation extremes. *Nature Climate Change*, *7*(1), 48–52. https://doi.org/10.1038/nclimate3168

R Core Team (2022). R: A language and environment for statistical computing. R Foundation for Statistical Computing, Vienna, Austria. URL https://www.R-project.org/

Rama Rao, Y. V., Hatwar, H. R., Salah, A. K., & Sudhakar, Y. (2007). An experiment using the high resolution Eta and WRF models to forecast heavy precipitation over India. *Pure and Applied Geophysics*, *164*(8–9), 1593–1615. https://doi.org/10.1007/s00024-007-0244-1

Reichle, R. H., & Koster, R. D. (2005). Global assimilation of satellite surface soil moisture retrievals into the NASA Catchment land surface model. *Geophysical Research Letters*, *32*(2). https://doi.org/10.1029/2004GL021700

Rummler, T., Arnault, J., Gochis, D., & Kunstmann, H. (2019). Role of Lateral Terrestrial Water Flow on the Regional Water Cycle in a Complex Terrain Region: Investigation With a Fully Coupled Model System. *Journal of Geophysical Research: Atmospheres*, *124*(2), 507–529. https://doi.org/10.1029/2018JD029004

Rummler, T., Wagner, A., Arnault, J., & Kunstmann, H. (2022). Lateral terrestrial water fluxes in the LSM of WRF-Hydro: benefits of a 2D groundwater representation. *Hydrological Processes*, *36*(3), e14510. https://doi.org/https://doi.org/10.1002/hyp.14510

Sampson, K., & Gochis, D. (2018). WRF Hydro GIS Pre-Processing Tools, Version 5.0, Documentation. *Boulder, CO: National Center for Atmospheric Research, Research Applications Laboratory*.

Saris, F., Hannah, D. M., & Eastwood, W. J. (2010). Spatial variability of precipitation regimes over Turkey. *Hydrological Sciences Journal*, *55*(2), 234–249. https://doi.org/10.1080/02626660903546142

Senatore, A., Furnari, L., & Mendicino, G. (2019). Impact of improved Sea Surface Temperature representation on the forecast of small Mediterranean catchments hydrological response to heavy precipitation. *Hydrology and Earth System Sciences Discussions*, *July*, 1–42. https://doi.org/10.5194/hess-2019-345

Senatore, A., Furnari, L., & Mendicino, G. (2020). Impact of high-resolution sea surface temperature representation on the forecast of small Mediterranean catchments' hydrological responses to heavy precipitation. *Hydrology and Earth System Sciences*, *24*(1), 269–291. https://doi.org/10.5194/hess-24-269-2020

Senatore, A., Mendicino, G., Gochis, D. J., Yu, W., Yates, D. N., & Kunstmann, H. (2015). Fully coupled atmosphere-hydrology simulations for the central Mediterranean: Impact of enhanced hydrological parameterization for short and long time scales. *Journal of Advances in Modeling Earth Systems*, *7*(4), 1693–1715. https://doi.org/10.1002/2015MS000510

Sikder, S., & Hossain, F. (2016). Assessment of the weather research and forecasting model generalized parameterization schemes for advancement of precipitation forecasting in monsoon-driven river basins. *Journal of Advances in Modeling Earth Systems*, *8*(3), 1210–1228. https://doi.org/https://doi.org/10.1002/2016MS000678

Skamarock, C., W., Klemp, J. B., Dudhia, J., Gill, D. O., Liu, Z., Berner, J., Wang, W., Powers, J. G., Duda, M. G., Barker, D. M., & Huang, X.-Y. (2019). A Description of the Advanced Research WRF Version 4. *NCAR Tech. Note NCAR/TN-556+STR*, 145 pp. https://doi.org/doi:10.5065/1dfh-6p97

Spinoni, J., Barbosa, P., Bucchignani, E., Cassano, J., Cavazos, T., Christensen, J. H., Christensen, O. B., Coppola, E., Evans, J., Geyer, B., Giorgi, F., Hadjinicolaou, P., Jacob, D., Katzfey, J., Koenigk, T., Laprise, R., Lennard, C. J., Kurnaz, M. L., Li, D., … Dosio, A. (2020). Future Global Meteorological Drought Hot Spots: A Study Based on CORDEX Data. *Journal of Climate*, *33*(9), 3635–3661. https://doi.org/10.1175/jcli-d-19-0084.1

Tabari, H., & Willems, P. (2018). Lagged influence of Atlantic and Pacific climate patterns on European extreme precipitation. *Scientific Reports*, *8*(1), 5748. https://doi.org/10.1038/s41598-018-24069-9

Taylor, K. E. (2001). Summarizing multiple aspects of model performance in a single diagram. *Journal of Geophysical Research*, *106*(D7), 7183–7192. https://doi.org/https://doi.org/10.1002/2014GL061623

Thompson, G., & Eidhammer, T. (2014). A study of aerosol impacts on clouds and precipitation development in a large winter cyclone. *Journal of the Atmospheric Sciences*, *71*(10), 3636–3658.

Toté, C., Patricio, D., Boogaard, H., van der Wijngaart, R., Tarnavsky, E., & Funk, C. (2015). Evaluation of satellite rainfall estimates for drought and flood monitoring in Mozambique. *Remote Sensing*, *7*(2), 1758–1776. https://doi.org/10.3390/rs70201758

Trenberth, K. E. (2011). Changes in precipitation with climate change. *Climate*

Research, *47*(1–2), 123–138. https://doi.org/10.3354/cr00953

Türkeş, M. (1996). Spatial and temporal analysis of annual rainfall variations in Turkey. *International Journal of Climatology*, *16*(9), 1057–1076. https://doi.org/10.1002/(SICI)1097-0088(199609)16:9<1057::AID-JOC75>3.0.CO;2-D

Türkeş, M., & Erlat, E. (2003). Precipitation changes and variability in Turkey linked to the North Atlantic oscillation during the period 1930-2000. *International Journal of Climatology*, *23*(14), 1771–1796. https://doi.org/10.1002/joc.962

Vaidya, S. S., & Singh, S. S. (2000). Applying the Betts-Miller-Janjic scheme of convection in prediction of the Indian monsoon. *Weather and Forecasting*, *15*(3), 349–356. https://doi.org/10.1175/1520-0434(2000)015<0349:ATBMJS>2.0.CO;2

Van de Walle, J., Thiery, W., Brousse, O., Souverijns, N., Demuzere, M., & van Lipzig, N. P. M. (2020). A convection-permitting model for the Lake Victoria Basin: evaluation and insight into the mesoscale versus synoptic atmospheric dynamics. *Climate Dynamics*, *54*(3), 1779–1799. https://doi.org/10.1007/s00382-019-05088-2

Vivoni, E. R., Tai, K., & Gochis, D. J. (2009). Effects of Initial Soil Moisture on Rainfall Generation and Subsequent Hydrologic Response during the North American Monsoon. *Journal of Hydrometeorology*, *10*(3), 644–664. https://doi.org/10.1175/2008JHM1069.1

Wang, W., Liu, J., Li, C., Liu, Y., Yu, F., & Yu, E. (2020). An Evaluation Study of the Fully Coupled WRF/WRF-Hydro Modeling System for Simulation of Storm Events with Different Rainfall Evenness in Space and Time. *Water*, *12*(4), 1209. https://doi.org/10.3390/w12041209

Wang, Y., Yang, J., Chen, Y., De Maeyer, P., Li, Z., & Duan, W. (2018). Detecting the causal effect of soil moisture on precipitation using convergent cross mapping. *Scientific Reports*, *8*(1), 1–8. https://doi.org/https://doi.org/10.1038/s41598-018-30669-2

Wehbe, Y., Temimi, M., Weston, M., Chaouch, N., Branch, O., Schwitalla, T., Wulfmeyer, V., Zhan, X., Liu, J., & Al Mandous, A. (2019). Analysis of an extreme weather event in a hyper-arid region using WRF-Hydro coupling, station, and satellite data. *Natural Hazards and Earth System Sciences*, *19*(6), 1129–1149. https://doi.org/10.5194/nhess-19-1129-2019

Weisman, M. L., Skamarock, W. C., & Klemp, J. B. (1997). The resolution dependence of explicitly modeled convective systems. *Monthly Weather Review*, *125*(4), 527–548. https://doi.org/10.1175/1520-0493(1997)125<0527:TRDOEM>2.0.CO;2

Xiang, T., Vivoni, E. R., & Gochis, D. J. (2018). Influence of initial soil moisture and vegetation conditions on monsoon precipitation events in northwest México. *Atmósfera*, *31*(1), 25–45. https://doi.org/10.20937/ATM.2018.31.01.03

Yilmaz, M. T., & Crow, W. T. (2013). The Optimality of Potential Rescaling Approaches in Land Data Assimilation. *Journal of Hydrometeorology*, *14*(2), 650–660. https://doi.org/10.1175/JHM-D-12-052.1

Yousefi, K. P. (2020). *Estimation of bias-corrected high-resolution radar precipitation maps using the radar and rain gauge network over Turkey*. Middle East Technical University.

Yucel, I., & Onen, A. (2014). Evaluating a mesoscale atmosphere model and a satellite-based algorithm in estimating extreme rainfall events in northwestern Turkey. *Natural Hazards and Earth System Sciences*, *14*(3), 611–624. https://doi.org/10.5194/nhess-14-611-2014

Yucel, I., Onen, A., Yilmaz, K. K., & Gochis, D. J. (2015). Calibration and evaluation of a flood forecasting system: Utility of numerical weather prediction model, data assimilation and satellite-based rainfall. *Journal of Hydrology*, *523*, 49–66. https://doi.org/10.1016/j.jhydrol.2015.01.042

Zeng, X.-M., Wang, B., Zhang, Y., Song, S., Huang, X., Zheng, Y., Chen, C., & Wang, G. (2014). Sensitivity of high-temperature weather to initial soil

moisture: a case study using the WRF model. *Atmospheric Chemistry and Physics*, *14*(18), 9623–9639. https://doi.org/10.5194/acp-14-9623-2014

Zhan, X., Zheng, W., Fang, L., Liu, J., Hain, C., Yin, J., & Ek, M. (2016). A preliminary assessment of the impact of SMAP Soil Moisture on numerical weather Forecasts from GFS and NUWRF models. *2016 IEEE International Geoscience and Remote Sensing Symposium (IGARSS)*, 5229–5232.

Zhang, F., Odins, A. M., & Nielsen-Gammon, J. W. (2006). Mesoscale predictability of an extreme warm-season precipitation event. *Weather and Forecasting*, *21*(2), 149–166. https://doi.org/10.1175/WAF909.1

Zhang, H., Liu, J., Li, H., Meng, X., & Ablikim, A. (2020a). The Impacts of Soil Moisture Initialization on the Forecasts of Weather Research and Forecasting Model: A Case Study in Xinjiang, China. *Water*, *12*(7), 1892. https://doi.org/10.3390/w12071892

Zhang, J., Lin, P., Gao, S., & Fang, Z. (2020b). Understanding the re-infiltration process to simulating streamflow in North Central Texas using the WRF-hydro modeling system. *Journal of Hydrology*, *587*, 124902. https://doi.org/10.1016/j.jhydrol.2020.124902

Zhang, Z., Arnault, J., Laux, P., Ma, N., Wei, J., & Kunstmann, H. (2021a). Diurnal cycle of surface energy fluxes in high mountain terrain: High-resolution fully coupled atmosphere-hydrology modelling and impact of lateral flow. *Hydrological Processes*, *35*(12). https://doi.org/10.1002/hyp.14454

Zhang, Z., Arnault, J., Laux, P., Ma, N., Wei, J., Shang, S., & Kunstmann, H. (2021b). Convection-permitting fully coupled WRF-Hydro ensemble simulations in high mountain environment: impact of boundary layer- and lateral flow parameterizations on land–atmosphere interactions. *Climate Dynamics*, 1–22. https://doi.org/10.1007/s00382-021-06044-9

Zhou, Y., & Mu, Z. (2018). Impact of different reanalysis data and parameterization schemes on WRF dynamic downscaling in the Ili Region. *Water (Switzerland)*, *10*(12), 1729. https://doi.org/10.3390/w10121729

Zittis, G., Bruggeman, A., Camera, C., Hadjinicolaou, P., & Lelieveld, J. (2017). The added value of convection permitting simulations of extreme precipitation events over the eastern Mediterranean. *Atmospheric Research*, *191*, 20–33. https://doi.org/10.1016/j.atmosres.2017.03.002

CURRICULUM VITAE

Surname, Name: Düzenli, Eren

EDUCATION

Degree	Institution	Year of Graduation
MS	METU Civil Engineering	2017
BS	METU Civil Engineering	2015
High School	Mehmet Emin Resulzade Anatolian High School, Ankara	2008

WORK EXPERIENCE

Year	Place	Enrollment
Feb 2020 – Current	METU	Research & Teaching Assistant
Sep 2018 – Sep 2021	METU (Granted by TÜBİTAK)	Project Assistant
Mar 2017 – Jun 2018	METU	Project Assistant

FOREIGN LANGUAGES

Advanced English

PUBLICATIONS

1. Afshar, M. H., Bulut, B., Duzenli, E., Amjad, M., & Yilmaz, M. T. (2022). Global spatiotemporal consistency between meteorological and soil moisture drought indices. Agricultural and Forest Meteorology, 316, 108848. DOI: 10.1016/j.agrformet.2022.108848.

2. Pilatin, H., Yucel, I., Duzenli, E., & Yilmaz, M. T. (2021). Sensitivity of WRF-derived hydrometeorological extremes to sea surface temperatures in regions with complex topography and diverse climate. Atmospheric Research, 264, 105816. DOI: 10.1016/j.atmosres.2021.105816.

3. Kilicarslan, B. M., Yucel, I., Pilatin, H., Duzenli, E., & Yilmaz, M. T. (2021). Improving WRF-Hydro runoff simulations of heavy floods through the sea surface temperature fields with higher spatio-temporal resolution. Hydrological Processes, 35(9), e14338. DOI: 10.1002/hyp.14338.

4. Bağçaci, S. Ç., Yucel, I., Duzenli, E., & Yilmaz, M. T. (2021). Intercomparison of the expected change in the temperature and the precipitation retrieved from CMIP6 and CMIP5 climate projections: A Mediterranean hot spot case, Turkey. Atmospheric Research, 256, 105576. DOI: 10.1016/j.atmosres.2021.105576.

5. Duzenli, E., Yucel, I., Pilatin, H., & Yilmaz, M. T. (2021). Evaluating the performance of a WRF initial and physics ensemble over Eastern Black Sea and Mediterranean regions in Turkey. Atmospheric Research, 248, 105184. DOI: 10.1016/j.atmosres.2020.105184.

6. Duzenli, E., Tabari, H., Willems, P., & Yilmaz, M. T. (2018). Decadal variability analysis of extreme precipitation in Turkey and its relationship with teleconnection patterns. Hydrological Processes, 32(23), 3513-3528. DOI: 10.1002/hyp.13275.

HOBBIES

Astronomy, Documentaries, Movies, Theatre, Acting, Literature, History, Philosophy, Football, Basketball, Tennis, Pilates, Hiking, Camping, Biking, Photography, Brainstorming